Eindhoven University of Technology

MASTER

Characterizing Particle Number Concentration, Size and Dispersion in a Cleanroom Environment

Vervoort, Luuk S.

Award date:
2022

Link to publication

Department of Applied Physics

Characterizing Particle Number Concentration, Size and Dispersion in a Cleanroom Environment

BY

L.S. Vervoort

MSC THESIS

Assessment committee
MEMBER 1 (CHAIR): PROF.DR. H.J.H. CLERCX (F&F)
MEMBER 2: DR.IR. M. DURAN MATUTE (F&F)
MEMBER 3: DR. A.Y. SILOV (PSN)
ADVISORY MEMBER 1: V. MORENO MARQUES MSC
(PRODRIVE TECHNOLOGIES)

Graduation
PROGRAM: APPLIED PHYSICS
CAPACITY GROUP: FLUIDS AND FLOWS
SUPERVISOR: PROF. DR. H.J.H. CLERCX
DATE OF DEFENSE: NOVEMBER 28, 2022
STUDENT ID: 1012093
STUDY LOAD (ECTS): 60
TRACK: FLUIDS, BIO AND SOFT MATTER

November 15, 2022

This page was intnentionally left blank

Abstract

In this thesis, an investigation will be done on Mie scattering and how to define a one-to-one relationship between measured intensity and the individual particle size, by optimizing light source spectral width and sensor detection angles. Besides this, we will look into the flow surrounding a sensor placed on a table in a cleanroom environment. How does personnel near the table and equipment on the table change the deposition of particles in a segment of the cleanroom. With this we investigate the possibility to estimate the particle size distribution in the whole cleanroom. For the first part of light simulations, we use a numerical simulation of particle counting. In these simulations we use different light sources, by which particles move into the laser beam and Mie scattering takes place. From this scattering we will derive a relationship between intensity and the particle radius R. We were able to conclude that a white light source with a detection angle of at least 45°-50° is required for obtaining a workable relation at relatively high intensity. At this detection angle the error stayed below 0.1 μm, necessary for properly sizing of particles in bins.

In the second part of flow simulations, we use STAR-CCM+ to characterize the air flow inside of a segment of the cleanroom. In this segment we have three different geometries in which we inject particles to investigate the deposition of these particles and their trajectories. These geometries consist of only tables, with equipment on the tables or with personnel working near the tables. From this we concluded that it is not possible to portray a good estimate of the particle size distribution in the whole cleanroom by placing one sensor on the desk. In the used geometries, the airflow in our region of interest (above the table) was separated from the rest of the cleanroom and it was not possible for particles to enter this region. Also the asymmetry in velocity fields and particle deposition makes it impossible to give a good estimate by using one sensor.

Table of Contents

1 Introduction

Particle contamination in the semiconductor manufacturing industry is a major topic of concern due to product failure when particle contamination takes place. Air quality in industry is often based on the amount of particulate matter or particles in the air. These particles can cause particle contamination on for example sensors. In the semiconductor manufacturing industry cleanrooms are a vital element in the production chain to prevent such contamination. A cleanroom provides the environment necessary to manufacture and assemble devices that can only tolerate a limited amount of contamination in order to function properly [1]. These devices are needed in fields such as optics, space engineering or production of computer chips for phones and computers. In order to limit the contamination of particles, one needs to find the source. Multiple studies suggest humans to be the main cause for particle pollution in cleanrooms or operating rooms [2, 3, 4]. The contamination comes from skin cells and clothing fibers. Personnel can disperse fragments from their skin and particles from their indoor, non-cleanroom clothing. With the skin losing over 20 million particles with a typical size of 30 μm per day it can be a significant factor to contamination, when there is much human activity in the cleanroom [2]. Taking this into account, good clothing is required in order to prevent the fibers coming off and the skin cells coming out. Face masks, gloves and hairnets are mandatory in some ISO cleanroom classes and act as a barrier filter for particles [5]. Of course there will be a variation in clothing and requirements depending on the application and products in the cleanroom.

Even though this barrier keeps out most of the particles from entering a cleanroom environment, some particles will get through due to human error or other complications. Furthermore, by limiting particle dispersion, microbial growth is reduced. Multiple papers have found that dust contamination is linked to microbial growth inside a cleanroom. In case of microbial growth, bacteria from the ground can be drawn into the airflow reaching other parts of the cleanroom, leading to a vicious circle creating more contamination in the cleanroom [6, 7]. To optimize the prevention of all of this, defining and characterizing the airflow inside a cleanroom needs to be done.

We focus on the industrial applications of air quality control as pursued by Prodrive Technologies. Prodrive Technologies is a company with a wide range of products such as power modules, air quality sensors, cameras and embedded computing systems. Some of these products are produced inside cleanrooms and therefore Prodrive Technologies has an interest in quantifying particle contamination and the air flow within a cleanroom. Different products require a different cleanliness level quantified by the number of particles per cubic meter. These requirements result in various ISO-cleanroom levels (ranging from 1 to 9) with each their respective tolerance levels of particle sizes and on this scale level 1 corresponds to the cleanest class [5]. When determining the levels of cleanliness one determines the particle size distribution. One possible way of doing this is measuring light scattering from a dust particle sized between 0.1 μm and 10 μm in diameter. There is a correlation between scattering intensity on the one hand, and particle size and overall concentration on the other hand. Light scattering for this range of particles is referred to as Mie scattering [8]. Currently, the process of measuring particle size distribution is done once or twice a year by an external company. These external companies perform measurements at different times and locations in the cleanroom. A problem with this method is the low accuracy and the high costs. Between two measurements one does not know the contamination levels or particle size distribution inside the cleanroom. When these levels increase between measurement moments, the dust particles could cause failures in a large product batch, which means that products would not conform to the set requirements. Also the measurement locations are of importance. Some areas are more susceptible for the settling of dust depending on the material and airflow surrounding the location. In this report we deal with the topic of a particle counter in cleanrooms and the positioning of a real-time data sensor taking the airflow in mind.

Optical particle counting uses the principle of Mie scattering. Mie theory was founded by

Maxwell and contemporaries in 1861 and is based on light scattering by electromagnetic waves on conducting metals [9]. Gustav Mie (1902) continued with the concept of light scattering by small spherical particles (smaller or comparable to the wavelength) made of an arbitrary material [8]. Although being named after Gustav Mie, Mie theory had contributions by Debye (1909) and Lorenz (1890) in the same period of time [10, 11]. Not much interest was given to this subject until the invention of computers more than 50 years later. After algorithms were created to calculate higher-order size parameters, this topic gained interest from a broad range of scientists. Some of these were Van de Hulst (1957), Kerker (1969) and Bohren & Huffman (1983) after which they extensively described the particle sizing from light scattering by small particles [12, 13, 14]. Using the scattered light from many of these particles we can determine the particle concentration, but determining the size of individual particles and the exact number in each bin size remains challenging.

With the formalism of Mie theory and due to the need to quantify air quality due to the exponential growth in production of semiconductor devices in the 1960-1970s, the first particle counters were designed. These particle counters were very primitive machines, and although being manually calibrated, these machines had limited accuracy [15]. When particle counters enhanced in quality, resulted in a high demand for better particle counters. Due to various vendors developing their own particle counters and the nonexistence of general guidelines, two particle counters from different companies could portray different size distributions. This problem was solved when the ISO 21501-4 was introduced [5]. The international standard defining rules and regulations on how a particle counter should measure and perform accurate measurements.

Sizing particles with increased accuracy in smaller particle ranges and the lowering of costs have been topics of research. Xiaoyu et al. (2017) have looked into the influence of the wavelength of the light, diameter and refractive index of the particles on the extinction coefficient and light intensity for dust particles by a laser beam [16]. They found that the theoretical values were in line with the experimental values in a 'test box' that illustrated the real case scenario. Gao [17] and Brattich [18] looked into low-cost designs for optical particle counters. The specific weaknesses in these designs stem from high humidity in the sensor and the limitations to the size (upper limit) of detectable particles.

In recent decades ventilation and airflow needed to be optimized in order to cope with the demand for higher-level cleanrooms. Two essential processes that play a key role in contamination are particle deposition and particle dispersion [19]. Particle deposition and dispersion are influenced by many factors including turbulence, indoor surfaces etc.[20]. These contributions are often difficult to experimentally verify and extremely time consuming to simulate. Simulating and predicting the flow with the use of Computational Fluid Dynamics (CFD) can help with limiting particle dispersion and thus contamination of products, while still being cost-effective. Many papers have validated simulations with experimental data. Posner (2003) compared CFD simulations with Laser Doppler Anemometry (LDA), Particle Image Velocimetry (PIV) and experimental tools of an indoor air flow in a sub-scale model room [21]. This in order to optimize the design of buildings with the use of this experimental data and simulations. Sadrizadeh (2014) numerically modelled the different airflow ventilation options in operating rooms, which have similar standards in allowed particles per unit volume [22]. Cleanrooms have typically high flow rates and low particle concentrations. This makes it difficult to model particle trajectories and particle contamination properly. Several models try to portray these phenomena and airflow correctly, such as the k-ε model. Chen (1995) and Rouaud (2002) investigated the airflow and turbulent dispersion by using k-ε models in indoor environments in order to see which would be most realistic [23, 24]. They found that the k-ε model works well in indoor environments.

Combining both topics of particle counting and flow in cleanrooms results in the following research questions:

How can we define a one-to-one relationship between intensity and individual particle size using Mie scattering by optimizing light source spectral width and sensor detection angles?

Is it feasible to obtain a good estimate of the particle size distribution in a cleanroom with a sensor placed on the desk? And how does the deposition of particles inside a cleanroom change taking into account personnel and equipment near and on the table?

In the first part a clear relationship between the intensity of the scattered light and the radius of the particle will be investigated for a monochromatic source and a white light source at varying detection angles. Besides that, the overarching practical question is to explore the feasibility of a particle counting sensor for Prodrive Technologies. Addressing concepts such as particle size distribution, sampling frequency and intensity of the light creates a better understanding of Mie theory and helps with the design of such a sensor. For part two, we determine if a particle counting sensor located on a cleanroom operator desk can measure a particle size distribution, which is representative for the whole cleanroom. By characterizing the flow around the desk we determine the deposition of particles. Personnel working close to the desk and equipment placed on the desk can possibly change this deposition, limiting the placement and accuracy of the sensor. Starting from a simple geometry with only two tables, several elements including two persons and equipment will be added to resemble different circumstances.

This research has been carried out at Prodrive Technologies by which access to MATLAB and Star-CCM+ software from respectively the Eindhoven University of Technology and Prodrive Technologies was granted. Furthermore, it is possible to experimentally validate parameters in the cleanroom from Prodrive Technologies. In order to answer the research question a theoretical framework about Mie scattering, particle dispersion and turbulent flow models and the associated parameters will be formulated. After defining this, two simulation models will be created. First in MATLAB by simulating and numerically solving the Mie equations, a relationship between intensity and particle radius and the Mie scattering patterns was investigated. The Star-CCM+ program was used to investigate the turbulent airflow in a section of the the cleanroom at Prodrive Technologies, which is called an impingement flow. This means a flow from an inlet impacting on a surface perpendicular to the flow. In section 2 we will elaborate on the theory behind Mie scattering, the impingement flow in the cleanroom, and the modeling of these phenomena. Section 3 will expand on which models and assumptions were made in each one of the two research questions. Subsequently the results of my investigation are being dealt with in section 4 and conclusions are drawn from these in section 5. This section will also give a discussion of the obtained results.

2 Theory

This section reports on the theory related to a potential sensor in which subjects such as Mie theory, bulk/particle counting and light source characteristics are featured. From section 2.6, a switch is made to part two about cleanrooms, cleanroom certification and flow theory.

2.1 Mie Scattering

Mie Theory describes the behaviour of light scattering for particle in the size range of the light wavelength. The solution to Maxwell's equations describing light scattering by a homogeneous sphere was found by Gustav Mie and is referred to as Mie scattering or Mie theory [8, 11]. The scattering processes for larger and smaller particles are respectively called Rayleigh scattering for smaller particles and geometric scattering for much larger particles. This division over three domains is based on a dimensionless size given by

$$x = kR = \frac{2\pi R}{\lambda},$$

(2.1)

with k being the wave number, R the radius of the sphere and λ being the wavelength. If

- $x \ll 1$, Rayleigh scattering,

- $x \approx 1$, Mie scattering,

- $x \gg 1$, Optical/geometric scattering.
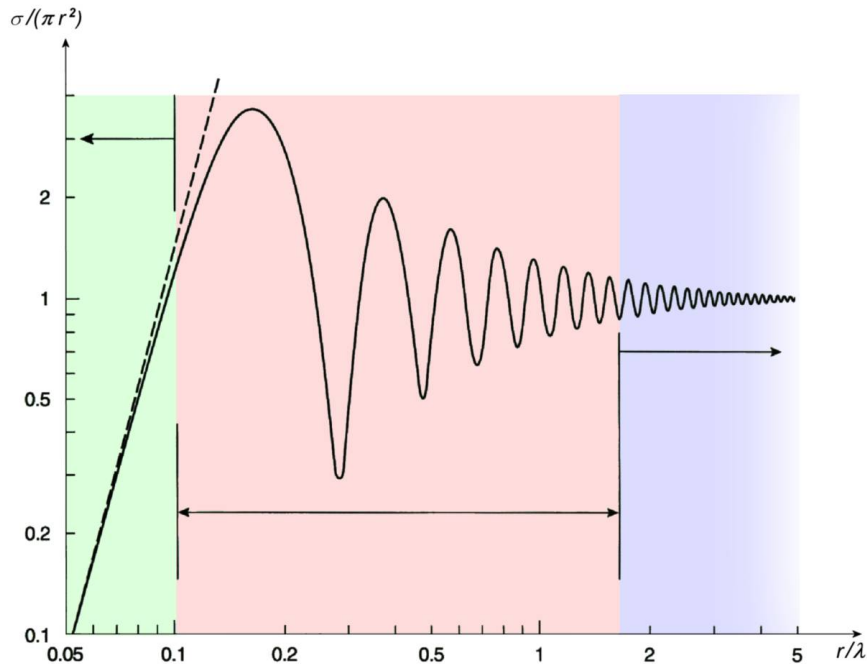
Figure 2.1 – The three distinctive regions for EM wave scattering by particles. The scattering efficiency '$\sigma/(\pi r^2)$' for interaction with radiation with wavelength λ for the scattering spheres with radius r. The Rayleigh region (green) can be approximated by a linear relationship for $\frac{r}{\lambda} \ll 1$ and the optical region can be approximated by a constant value of 1 in the limit $\frac{r}{\lambda} \gg 1$. The oscillations in the Mie regime (red) illustrate the complicated relationship for scattering of particles when $\frac{r}{\lambda} \approx 1$[25].

In the case of cleanroom cleanliness the particle sizes are in the same order of magnitude as the wavelength of the light, which is in the range of 0.1 μm to 10 μm in diameter. Compared to the other size regions, determining particle size in the Mie scattering region contains many difficult

relations [12]. In Fig. 2.1, we distinguish the above mentioned three different regions for scattering efficiencies as function of $\frac{r}{\lambda}$. The exact definition of the scattering efficiency will be given in section 2.2, but the dimensionless efficiency factors are a ratio of the cross section of the particles for extinction, absorption and scattering and the geometrical cross section. These ratios are functions of the orientation of the particle and state of polarization of the incident light [12]. For Rayleigh and optical scattering a forward relationship can be defined by a linear function. In the Mie scattering regime defining particle size from the intensity of the light is complicated due to resonances occurring in the efficiencies as function of the size parameter. One of the difficulties comes from the calculation of the Mie coefficients used for calculation of the amplitudes of the scattered field. Due to computational advances [26] [27] these problems have recently become more tractable.

In his paper Mätzler provides scripts for the calculation of the coefficients and scattering amplitudes for a polar plot of the scattering of a particle. This paper limits its capabilities to a homogeneous dielectric sphere without change in the magnetic permeability between the inside and outside of the particle. The derived expressions and equations in this section can be found in Van de Hulst et al. (1981) and by Bohren et al. (1983)[12, 14]. The equations that arise from the Mie coefficients and that need to be solved for every particle size or scattering angle can be very time consuming. The coefficients are the key parameters and are determined by the following definitions

$$
\begin{aligned}
a_n &= \frac{m^2 j_n(mx)\,[xj_n(x)]' - \mu_1 j_n(x)\,[mxj_n(mx)]'}{m^2 j_n(mx)\left[xh_n^{(1)}(x)\right]' - \mu_1 h_n^{(1)}(x)\,[mxj_n(mx)]'}, \\[2mm]
b_n &= \frac{\mu_1 j_n(mx)\,[xj_n(x)]' - j_n(x)\,[mxj_n(mx)]'}{\mu_1 j_n(mx)\left[xh_n^{(1)}(x)\right]' - h_n^{(1)}(x)\,[mxj_n(mx)]'}, \\[2mm]
c_n &= \frac{\mu_1 j_n(x)\left[xh_n^{(1)}(x)\right]' - \mu_1 h_n^{(1)}(x)\,[xj_n(x)]'}{\mu_1 j_n(mx)\left[xh_n^{(1)}(x)\right]' - h_n^{(1)}(x)\,[mxj_n(mx)]'}, \\[2mm]
d_n &= \frac{\mu_1 m j_n(x)\left[xh_n^{(1)}(x)\right]' - \mu_1 m h_n^{(1)}(x)\,[xj_n(x)]'}{m^2 j_n(mx)\left[xh_n^{(1)}(x)\right]' - \mu_1 h_n^{(1)}(x)\,[mxj_n(mx)]'},
\end{aligned}
\tag{2.2}
$$

in which $m = m_1 + im_2$ is the complex refractive index, $x = kR$ is the size parameter, R is the sphere radius and $k = \frac{2\pi}{\lambda}$ the wave number and λ the wavelength in the ambient medium. The ratio of the magnetic permeability of the sphere to the ambient medium is denoted by μ_1. The magnetic susceptibility is defined as $\chi_m = \mu_1 - 1$. We put the magnetic susceptibility to zero and the magnetization of the spherical particles is zero, so $\mu_1 = 1$ [11]. The functions $j_n(z)$ are spherical bessel functions of the first kind and $h_n^{(1)}(z) = j_n(z) + iy_n(z)$ is the spherical Hankel function of the first kind of order n ($n = 1, 2, ...$), also $z = mx$. Here $y_n(z)$ is the spherical Bessel function of the second kind. The primes behind functions in between brackets denote derivatives with respect to the argument inside the functions. Derivatives of spherical Bessel and Hankel functions and the relationship between the Bessel and spherical Bessel functions can be found in Bowman (2012) and will not be discussed here [28].

2.2 Scattering Efficiencies

In order to quantify the intensity division between scattering, absorption, extinction and back scattering we use the efficiencies Q_i. We normalize the cross sections of these processes σ_i to the geometrical cross section πa^2. The i runs over the scattering, absorption, extinction and back scattering efficiency. Figure 2.2 gives a schematic overview is given of the difference between σ_i and the geometrical cross section. Energy conservation requires

$$
Q_{ext} = Q_{sca} + Q_{abs}, \Rightarrow \sigma_{ext} = \sigma_{sca} + \sigma_{abs}.
\tag{2.3}
$$

By integrating the scattered power over all directions we obtain explicit expressions for the scattering efficiency Q_{sca} in terms of the Mie coefficients and from the Extinction theorem mentioned in Van de Hulst et al. we get an expression for Q_{ext}[12] as

$$Q_{sca} = \frac{2}{x^2} \sum_{n=1}^{\infty} (2n+1) \left(|a_n|^2 + |b_n|^2 \right), \tag{2.4}$$

$$Q_{ext} = \frac{2}{x^2} \sum_{n=1}^{\infty} (2n+1) \operatorname{Re}(a_n + b_n). \tag{2.5}$$

Combining these two equations into Eq. 2.3 we can derive Q_{abs}. The last term needed is Q_b the back scattering efficiency given by

$$Q_b = \frac{1}{x^2} \left| \sum_{n=1}^{\infty} (2n+1)(-1)^n (a_n - b_n) \right|^2. \tag{2.6}$$

Although calculations of scattering amplitudes are based on infinite series in terms of the Mie coefficients, in practice the terms start to become negligibly small when the index is somewhat larger than the size parameter x, so the series can be taken up to a finite upper bound n_{max}, which has been determined by Bohren et al (1983)[14] as

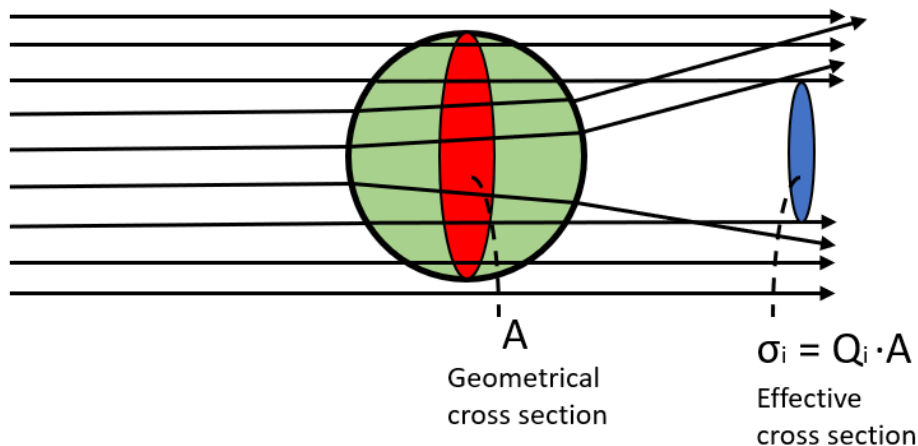$$n_{max} = x + 4x^{\frac{1}{3}} + 2. \tag{2.7}$$

Figure 2.2 – Schematic overview of the effective cross section compared to the geometrical cross section of a particle with Q_i being the efficiency, A the geometrical cross section and σ_i the effective cross section. σ_i can be lower due to scattering, absorption, extinction or back scattering.

2.3 Calculating an intensity from a scattering amplitude

To characterize the scattering around a particle we use the intensity. For determining the angular distribution of light intensity the scattering amplitudes S_1 and S_2 need to be defined as in Bohren and Huffman [14]. These scattering amplitudes are used for determining both intensity I and the scattered field $\vec{E}_s$. In the following equations the time variation is left out.

$$S_1(\cos(\theta)) = \sum_{n=1}^{\infty} \frac{2n+1}{n(n+1)} (a_n \pi_n + b_n \tau_n),$$

$$S_2(\cos(\theta)) = \sum_{n=1}^{\infty} \frac{2n+1}{n(n+1)} (a_n \tau_n + b_n \pi_n), \tag{2.8}$$

$$E_{s\theta} = \frac{e^{ikr}}{-ikr} \cos(\phi) \cdot S_2(\cos(\theta)),$$

$$E_{s\phi} = \frac{e^{ikr}}{ikr} \sin(\phi) \cdot S_1(\cos(\theta)). \tag{2.9}$$

In equations 2.8 and 2.9, θ is the scattering angle in the horizontal scattering plane and ϕ is the angle between the incident electric field and the vertical scattering plane, as seen in Fig. 2.3. Furthermore $E_{s\theta}$ and $E_{s\phi}$ are the components of the scattering field respectively in the plane and orthogonal to the scattering plane. The angular scattering patterns of the spherical harmonics are described by $\pi_n(cos(\theta))$ and $\tau_n(cos(\theta))$, which are used in the calculations of the scattering patterns according to the following formulas [14],

$$\pi_n = \frac{2n-1}{n-1}\cos\theta \cdot \pi_{n-1} - \frac{n}{n-1}\pi_{n-2},$$
$$\tau_n = n\cos\theta \cdot \pi_n - (n+1)\pi_{n-1}. \tag{2.10}$$

The intensities of the vertically and horizontally polarized components of the scattered light I_1 and I_2 can be derived from the scattering amplitudes with $I_1 = |S_1|^2$ and $I_2 = |S_2|^2$. For unpolarized light we can determine the angular intensity distribution for a single particle under the same assumptions as mentioned above and $I(\theta)$ is

$$I(\theta) = \frac{I_0}{2k^2l_d^2}\left(I_1 + I_2\right) = \frac{I_0\lambda^2}{8\pi^2l_d^2}\left(|S_1|^2 + |S_2|^2\right), \tag{2.11}$$

in which l_d is the distance from the particle to the light intensity detector [29, 16]. These above mentioned equations have been formulated in the past century, but defining and visualising the intensity as a function of radius for different parameter values remains a topic of interest. The visualisation is done by using polar plots. Besides this, evaluating the light source options to create a more straightforward relation between the intensity and the particle radius will be added. The scattering amplitudes can be used in order to make a polar plot to illustrate the direction and magnitude of the scattered light for different sizes of particles and other parameters, such as shown in figure 2.3. In such a polar plot we can distinguish scattering to the front and backward scattering with relative high intensity and the side lobes with lower intensity.
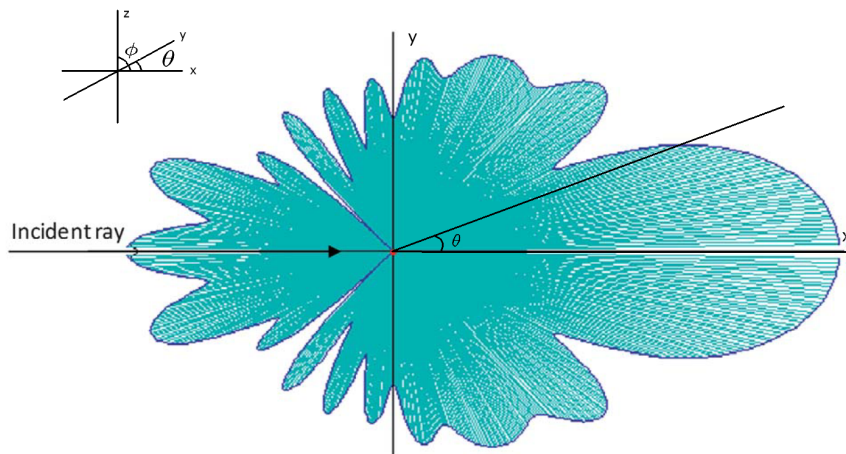
Figure 2.3 – Example for the 2D angular distribution in the horizontal plane for a monochromatic light source with λ = 960 nm, scattered by a spherical particle of $R = 1.5\,\mu m$ and $m = 1.5 - 0i$. [30]

As discussed before in section 2.1 the three different particle size regions in the plot have three general different scattering patterns for Rayleigh, Mie and optical scattering. Whereas Rayleigh scattering is symmetric in the center, Mie scattering is more focused to the front. The larger the particles, the more focused to the front the light intensity is, until they eventually reach the optical region. Figure 2.4 gives a schematic overview of these relations.

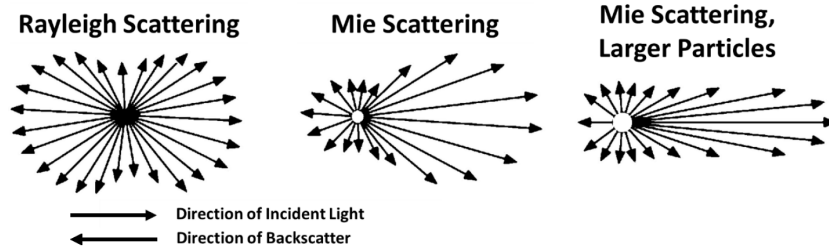*Figure 2.4 – Three different regions of scattering have three distinctive scattering patterns. While Rayleigh scattering is symmetric, with Mie scattering the intensity is more focused to the front lobe. In general the larger the particles becomes, the more focused to the front the intensity will become [31].*

These lobes occur due to constructive and destructive interference of the scattering signal. In Mie scattering the front lobe has a much higher intensity compared to the other lobes. The amount of lobes and the angular distribution of these ripples depend on the particle properties, size and the wavelength of the light source [14]. Properties of the particle are volume, shape, material, roughness of the surface and orientation.

The shape of the particle matters: Particles are seldom smooth and spherical like the PSL (Polystyrene latex spheres) particles that are used for calibration. Particles are often flakes of skin or jagged fibers and when they float with a different orientation, a different amount of light is scattered [32]. Another contribution to the amount of light perceived by the detector is the reflectivity of the particles. Particles, like aluminum, reflect more light than others, which leads to more light reaching the detector. The pulse that is generated is higher in amplitude and the particle counter presumes a bigger particle than it truly is [32].

Mie theory can be extended to different shapes of particles or with different material properties. Latimer et al. [33] pointed out that in case a spheroid particle is orientated at an angle of $45°$ to the incident light, asymmetry in the scattering pattern is observed. There tend to be less lobes near directions the particle is directed, but they are higher in intensity. In Fig. 2.5 one can see an illustrative approach for the distinctive scattering patterns by Bohren [14]. In the left top a perfectly spherical particle creates a similar symmetrical pattern as in Fig. 2.3. When the particle tend to be more spheroidal and orientated at an angle of $45°$, as seen in the bottom figures, asymmetry appears with more intensity of light scattered towards the orientation of the particle. For the prolate spheroid small lobes appear on the left side indicated by the dashed line. For prolate and oblate spheroids the efficiencies for scattering and thus extinction are different [14]. When comparing the dashed line from the prolate with the line on the right for the oblate spheroid one can see that these are different, even though the aspect ratio a/b is the same. For now we limit ourselves to perfectly spherical particles.

Another phenomenon that occurs when particles travel through the particle counter is particle aggregation. Aggregation is the clustering of particles and the formation of irregular particle assemblages or agglomerates [34]. The clustering leads to the non-sphericity of the composite, causing the scattered light to scatter different than when the particles would be spherical. Furthermore the size of the total cluster is different, leading to possibly more scattering, compared to the individual particles.
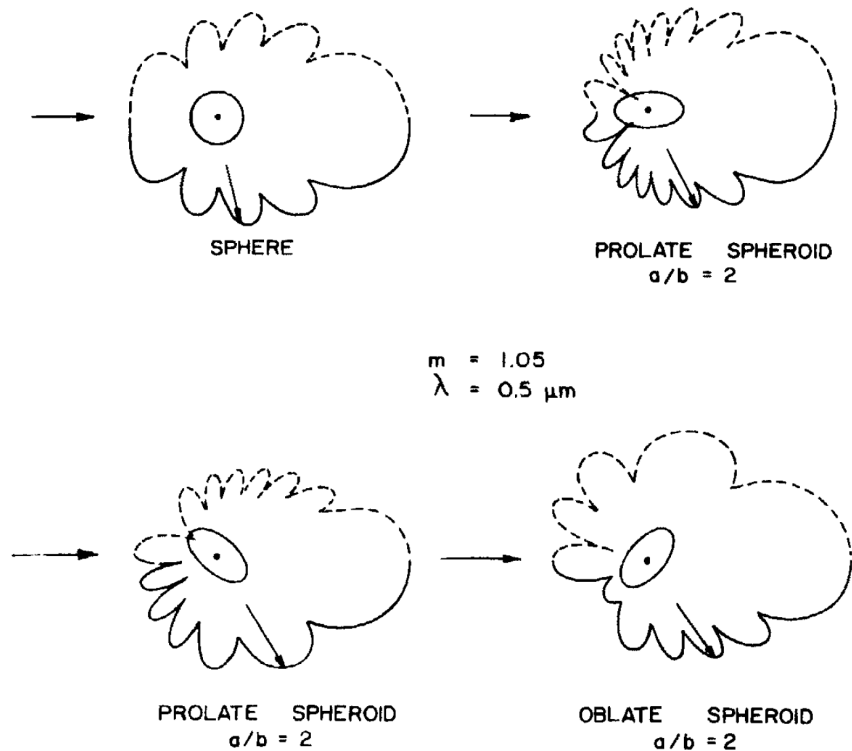
Figure 2.5 – Four spheroids with the two top pictures indicating different volumes and the bottom pictures having different orientation. The dashed line represents the left side of the scattering pattern. a and b are respectively the equatorial and the polar diameter, m = 1.05 and λ = 500 nm. Un-polarized incident light coming from the left [14].

These relationships are not straightforward and will be elaborated on in chapter 4. The sensor mechanism consists of inverting the relationship and obtain particle size from the scattering intensity of the particle at a certain angle.

2.4 Particle counting using Mie theory

2.4.1 Nephelometry

A method that is often used in this field is nephelometry or bulk counting. Bulk counting is a technique where the total amount of light from Mie scattering is measured and integrated over a certain time period. Instead of identifying individual particles, the sensor accumulates the signal of several particles over a certain integration time. The intensity of this scattered light is a direct measure for the particle concentration. Companies calibrate their sensor beforehand at a known concentration. An essential note here is that one cannot obtain any information about the particle size distribution with nephelometry (for example PM1.0, PM2.5 etc.). Here PM1.0 means Particulate Matter smaller than 1 micron and is the bin size. Bin sizes are the channels in which we sort the particles per size. What some companies do is by having a sensor calibrated to PM2.5 concentration, they estimate the PM10 concentration to be 4 times higher, which is not the case.

2.4.2 Particle counting

To determine the particle size of individual dust particles from the scattered intensity we need a particle counting sensor. Here we evaluate the scattering of individual particles and thus complementing the nephelometry technique. A basic particle counter consist of a light source, photodetector, a dust flow passing through the system and possibly two lenses to focus the light beams on the dust flow and photodetector, but these are not mandatory. Besides these a light trap can be useful to avoid back reflections. In this viewing volume of the light source the scattering by dust particles takes place. The viewing volume is the volume of the dust flow intersecting with the illumination from the light source. After the light has scattered in all directions, a certain fraction of the light is collected by the photodetector. The photodetector is placed at a certain angle compared to the original light beam. This photodetector generates an electrical current proportional to the incident

light power which is then converted to a digital signal by a analog digital converter to establish the particle size. As seen in Fig. 2.6b the horizontal lines are intensities belonging to a PM value. So if we have bins PM1.0 and PM2.5, PM1.0 means all particles smaller than 1 µm and PM2.5 collects all particles between 1 and 2.5 µm. The total path of the light beam can be found in Fig. 2.6a. Figure 2.6b shows a possible digital signal representing particle flow through a viewing volume.

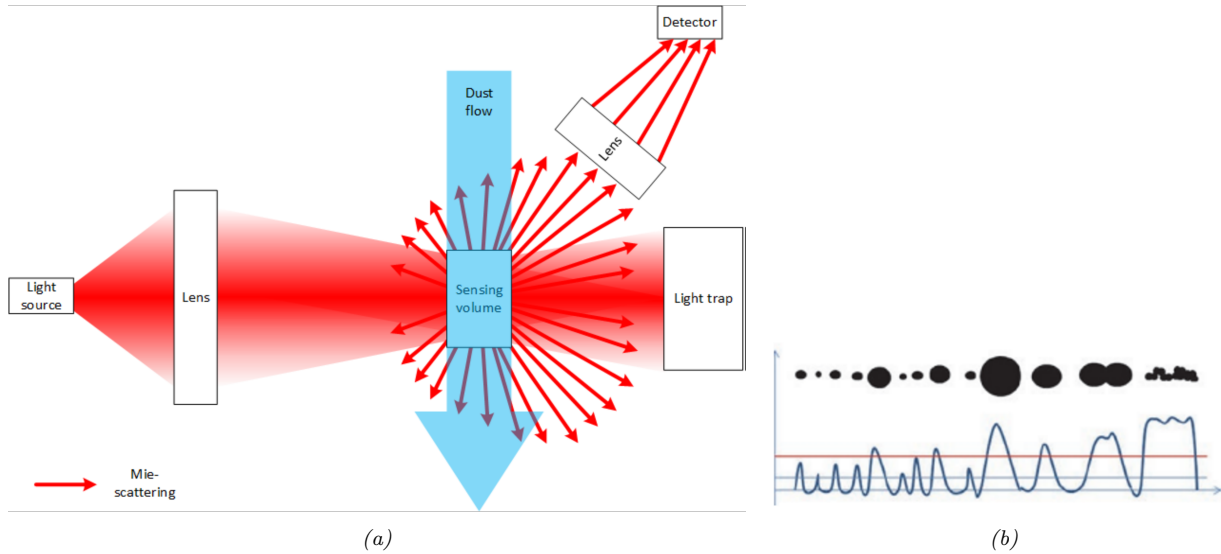<center>(a)</center>
<center>(b)</center>

Figure 2.6 – a) Schematic overview of the path that light travels inside a particle counting sensor from the light source to the photodetector. First the light beam is directed at a dust flow with particles by a lens. In this viewing volume the particles scatter the light in all directions. A certain fraction of the light is focused on the detector by a second lens. This photodetector is placed at a fixed angle and captures the light and converts it to a signal. b) Possible signal with the peak height as indicator for the particle size. When multiple particles are inside the viewing volume the peaks of the individual particles overlap. As long as the sampling frequency is high enough this does not need to be a problem. The horizontal lines indicate the calibrated bin thresholds needed to determine the typical particle size [35].

In the case of particle counting, the intensity reaching the detector due to scattering will increase if a particle enters the viewing volume. As mentioned in section 2.3 larger particles are expected to have higher intensities. In Fig. 2.6b this is also indicated by larger spheres generating larger peaks. At the right multiple particles have entered the viewing volume at once, causing an overlap of peaks. The individual scattering intensities are accumulated on the detector causing a small plateau with bumps. A high enough sampling frequency f_s is then needed to still differentiate between the individual particles. Sampling frequency means samples per second made. The sampling frequency for distinguishing peaks is based on the Nyquist theorem, which states that the sampling frequency should be twice the Nyquist frequency in order to correctly sample a continuous signal in a discrete sequence [36]. In case the highest frequency of the signal is lower than the Nyquist frequency, the discrete-time sequence contains no distortion or aliasing and is correctly sampled. The process is illustrated in Fig. 2.7. Here the correct intensity as function of time is given for two overlapping particles with a Δt between the peaks by the blue line. Between the peaks we see a summation of the individual signal intensities. In case f_s is not high enough only the large points are sampled and a possible wrong signal is sampled reading out the wrong particle size. For overlapping particles or particles separated 0.1 µm the sampling frequency needs to be tens of MHz at a velocity v=2 m/s. Increasing the sampling frequency might cause noise to be problematic, due to the averaging of signals being excluded [37]. In the case the sampling frequency is not high enough the intensities in that time interval would be accumulated as one large particle by the photodetector instead of multiple smaller particles, creating an error in the binning output, which is quantifying the particles size in predefined ranges. Other phenomena such as particles moving in front of one and other also contribute to inaccurate binning. It therefore remains important to have one particle in the viewing volume at once.
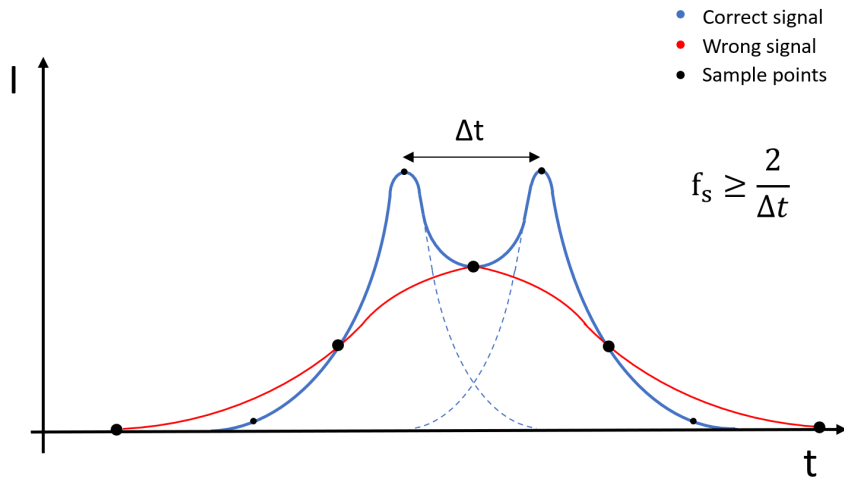
Figure 2.7 – Schematic representation of how the sampling frequency should be determined. When two individual particles have overlapping intensity peaks, the sampling frequency should be twice the frequency between the peaks determined by the Δt between the peaks. A possible wrong signal created by a too low f_s is indicated by the red line using only the large points.

Another important feature that is essential to ensure that we measure one particle at the time is the viewing volume. When the particle concentration in the flow is high, the viewing volume should be small to maintain one particle in the viewing volume per sample. If the concentration is low we increase the viewing volume. This idea is illustrated in Fig. 2.8. The expansion or shrinking of the viewing volume can be done by changing the optical beam size, or by changing the flow diameter. In case we know the concentration of particles we can adjust the viewing volume to the correct size. The relationship between concentration and viewing volume can be calibrated beforehand. Once these are set, we calibrate the intensities for our bin sizes [32].
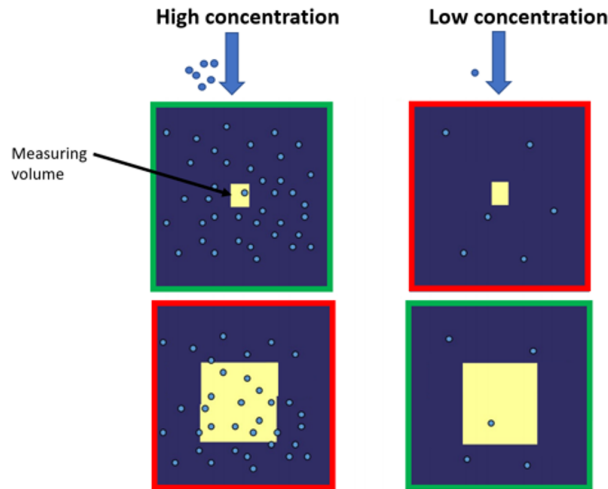

Figure 2.8 – Schematic representation of a small and large viewing volume in different concentrations. A small viewing volume in a high concentration or a large viewing volume in a low concentration is desirable to measure individual particle sizes [35].

Particle counters do not actually count every particle in the room. Particle counters often have 0.1 or 1 CFM (cubic-foot-per-minute) as a volume per time that is analysed. This means if we have a 5000 ft^2 cleanroom with a 12 foot ceiling a 1 CFM particle counter would analyse 0.001% of the total volume in an hour. In order to portray correct results from such a small sample, the counter should sample enough volume of air to statistically represent the volume. The sampling techniques appear simple, but particles not always truly diffuse within a sample volume. Particles often stay in laminar flow, accumulate inside turbulent flow, deposit, and rise in warm air. Although cleanrooms minimize these problems, there will always be areas where particles congregate [32].

11

2.5   Light source characteristics

For the light source, we can have several options. Two options will be considered: a monochromatic laser and a white LED light source. A monochromatic laser therefore radiates light at a narrow spectral width [38]. For our purposes we assume a (theoretical) single frequency laser. A white LED light source contains the spectrum of radiation with wavelengths from the visible light range, which is from around 400 nm to almost 800 nm. We consider a white LED light source with a spectrum between 380 and 780 nm as in Tosini (2016)[39]. Below in Fig. 2.9 one can see the relative spectrum belonging to a white LED for each wavelength.
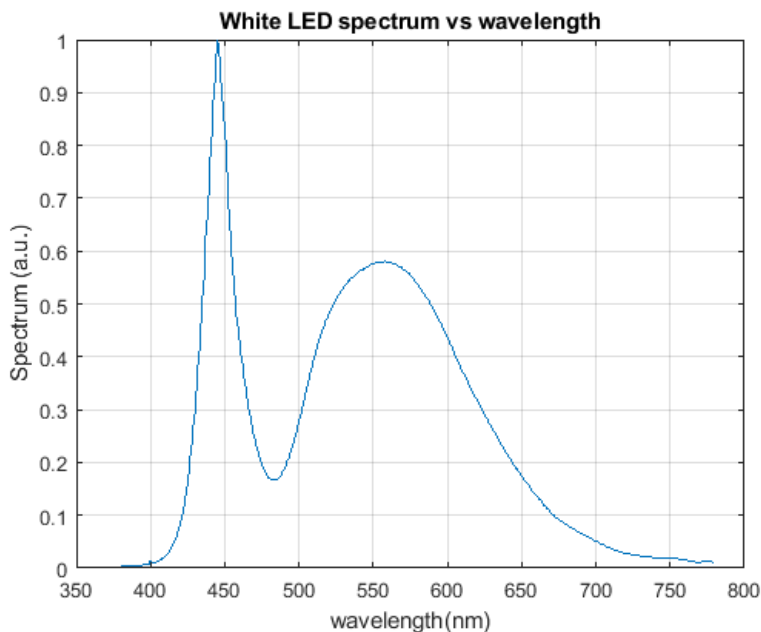

Figure 2.9 – Relative spectrum of a white LED for the wavelength range of 380 nm to 780 nm.

Another aspect to consider is the Gaussian radial intensity variation [40]. From the center outwards the intensity declines according to a Gaussian profile with maximum at $r=0$. For a laser, this circular profile at a certain wavelength and polarization is determined by the waist w_o. The waist is a measure of the beam size at the point of its focus. The intensity is the largest at (0,0) of a Gaussian profile [41]. When the laser is focused on a dust flow, all particles will presumably not move through the laser at the same position. This would mean that two identical particles of the same size, with one of them having a larger distance from the center of the laser beam, acquire a different intensity from the source. This in turn leads to the photodetector picking up a different signal from the scattering intensity, leading to particle sizing errors in the output data. This can be especially problematic in intensity regions around the binning thresholds as illustrated in Fig. 2.10. Here the three colour regions are indications of different acquired intensity from the source, in real life this is a continuous process when moving radially outwards. Knowing this, it is important to realize where the particle passes through laser in order to lower the sizing error.
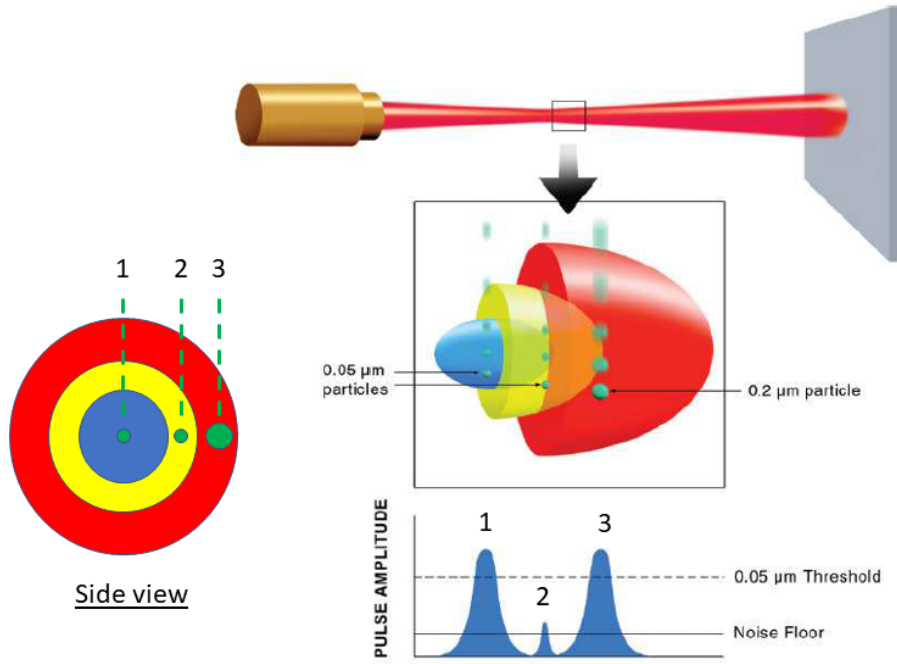
Figure 2.10 – Output signal amplitude for three particles moving through the laser at different positions. Due to the Gaussian character of the laser beam, particles passing through the different coloured regions obtain a varying intensity of light from the source. Radially outwards the intensity decreases according to the Gaussian profile. Two equal in size particles entering at position 1 and 2, therefore create a signal varying in amplitude. The same holds for a larger particle entering the laser at large radial distance 3 from the center, generating an equal amplitude signal to 1, although they are different in size. This phenomena causes particle sizing errors [32].

2.6   Cleanliness in cleanrooms

As stated in the introduction, cleanrooms are a vital element of the semiconductor production chain to limit the particle contamination on products. The design of a cleanroom is a crucial contributing factor to the isolation and active removal of dust particles. This consists of preventing dust from entering and improving the removal of contaminants in the cleanroom. The first bit is done by creating an overpressure relative to the surroundings [42]. This is done by blowing more clean air in than is going out until a minimum pressure requirement is met. The air coming in is filtered using high-efficiency particulate absorbing (HEPA) and/or ultra-low particulate air (ULPA) filters [32]. With HEPA filters removing 99.97% particles larger than $0.3\,\mu$m and ULPA filters taking out 99.9997% of particles larger than $0.12\,\mu$m. The overpressure causes leakages of air out of the cleanroom instead of the dust drifting inside. In the opposite case of producing vaccines, a company does not want a virus or bacteria to leave the cleanroom and for that purpose they create a lower pressure inside.

The size of cleanrooms can range from a single user laboratory being a few square meters to complete factories consisting of thousand square metres of floor levels [1]. With the variety of size and the variety in applications of cleanrooms, each cleanroom is designed differently. Although the cleanrooms are often different, the basic principles in relation to airflow, air refresh rate, building materials, clothing regulations and pressure inside the cleanroom have similar approaches. The ISO-14644 document defines measurement standards and regulations for the the maximum allowed particles per volume [5]. Examples of categories that are dealt with are design, classification of air cleanliness and how the surfaces should be cleaned. With the use of these requirements, companies get their cleanrooms certified at a certain class ranging from ISO 1 to ISO 9, with each of the allowed particles per volume per particle diameter based on the following equation [43]

$$C_N = 10^N \left(\frac{0.1}{d}\right)^{2.08}. \tag{2.12}$$

Here N is the ISO class and d is the particle diameter in microns. With this particle diameter we define bin sizes. For the ISO standard these bin sizes are $\geq 0.1\,\mu$m, $\geq 0.2\,\mu$m, $\geq 0.3\,\mu$m, $\geq 0.5\,\mu$m,

$\geq 1\,\mu\text{m}$ and $\geq 5\,\mu\text{m}$. Table 2.1 lists the allowed particles belonging to each respective bin size. The missing numbers in the left bottom are due to the concentration limits not being applicable for these bin sizes. For the right top of the table the concentrations are too low and this makes the sampling inappropriate. From class 5 up to 1, the $\geq 5\,\mu\text{m}$ size of particles are not allowed inside the cleanroom.

Table 2.1 – Classification of ISO cleanroom levels illustrating the maximum allowed of contaminants per m^3 for each particle bin size [42]

ISO Classification number	Maximum concentration limits (particles/m^3 of air)					
	$\geq 0.1\,\mu\text{m}$	$\geq 0.2\,\mu\text{m}$	$\geq 0.3\,\mu\text{m}$	$\geq 0.5\,\mu\text{m}$	$\geq 1\,\mu\text{m}$	$\geq 5.0\,\mu\text{m}$
ISO Class 1	10	2				
ISO Class 2	100	24	10	4		
ISO Class 3	1000	237	102	35	8	
ISO Class 4	10,000	2370	1020	352	83	
ISO Class 5	100,000	23,700	10,200	3520	832	29
ISO Class 6	1,000,000	237,000	102,000	35,200	8320	293
ISO Class 7				352,000	83,200	2930
ISO Class 8				3,520,000	832,000	29,300
ISO Class 9				35,200,000	8,320,000	293,000

A crucial element in the design is the airflow inside a cleanroom. The two main types of cleanroom are a 'Turbulent cleanroom' and a 'Laminar Flow cleanroom'[32]. Both designs are schematically illustrated in Fig. 2.11. A 'turbulent cleanroom' uses a non-unidirectional airflow from an inlet in the ceiling to keep the air in constant motion downwards where it is extracted on the sides at the bottom of the walls [43]. The contamination is diluted and mixed with the new air coming from the ceiling when pushed downwards. Due to the mixing and swirling of the flow there is a possibility of additional recirculating flows appearing across the cleanroom, which is undesirable when you want contaminants to move to the outlets directly. In the laminar flow cleanroom, air is coming from multiple inlets in order to create a unidirectional air flow coming from the top to the floor. The air leaves the room via the floor or vents close to the floor. This methods lets in significantly more air, but the spreading of contaminants is limited as a result of the directional airflow. An indication for this is the relative air changes per hour, which for a turbulent cleanroom is given by [43]

$$\text{Air changes / hour } [\text{h}^{-1}] \ = \ \frac{\text{air volume rate } \left[\text{m}^3\,\text{h}^{-1}\right]}{\text{volume of room } [\text{m}^3]}. \tag{2.13}$$

Turbulent cleanrooms have between 10 and 100 air changes per hour and inlet velocities of below 0.20 m/s depending on the ISO class. For the laminar cleanroom the air changes becomes less relevant since we have unidirectional airflow. Therefore the air changes are not dependent on the volume of the room, but more on the height of the ceiling [43]. The inlet velocity and ceiling coverage are good parameters for indicating the cleanliness in the laminar cleanroom. With the inlet velocity ranging between 0.3 and 0.5 m/s we obtain more air changes per hour. Ceiling coverage means the number of inlets in the ceiling compared to the total area of the ceiling. Variations on the ceiling coverage case can cause differences in the air changes per hour. At Prodrive Technologies there is an ISO-6 and ISO-5 cleanroom. The ISO-5 cleanroom uses the laminar air flow principle with pillars spread out through the cleanroom sucking in air that is removed via vents close to the floor. The ISO-6 area allows more particles and thus a turbulent airflow is used, with less ceiling coverage. This because a laminar flow cleanroom is more expensive to build and maintain.
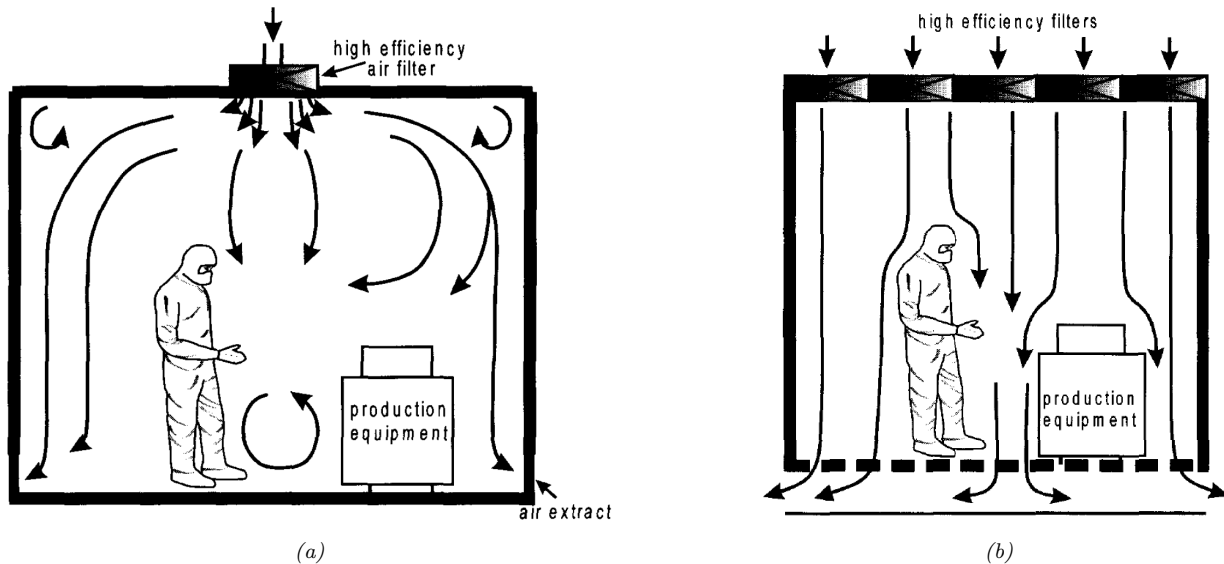
Figure 2.11 – The two common types of cleanrooms illustrating the airflow patterns of a) a turbulent airflow and b) a laminar airflow. The laminar airflow uses more air through its inlets, but has an enhanced effect on the limited spreading of contaminants [43].

2.7 Jet impingement flow

The development of a flow and resulting heat transfer depends on various parameters, such as Reynolds number (Re) and the Prandtl number (Pr). The Reynolds number is the ratio of inertial forces to viscous forces within a fluid which is subjected to relative internal movement due to different fluid velocities. $Re = \frac{u \cdot L}{\nu}$, with u being the flow speed in m/s, L the characteristic length scale in m and ν the kinematic viscosity of the fluid in m^2/s. The Reynolds number can be an indication of turbulence in a flow. For example, for Reynolds' pipe flow around Re=2300 is often considered to be the transition from laminar to turbulent flow [44]. Below this value a flow is often considered to be laminar. Such a flow with high Reynolds number will have more fluctuations in velocity or pressure. The large scale motions of the flow are influenced by the geometry of the flow too, for example by boundary conditions along the wall. For the case of the cleanroom, the geometry generates a recirculation zone causing the mixing and merging with the flow from the inlets generating dynamic behaviour and thus turbulence. Due to this unsteady and irregular behaviour of the flow, turbulent flows are normally treated statistically rather than deterministically.

The Prandtl number is a dimensionless number defined as the ratio of momentum diffusivity ν to thermal diffusivity κ, thus $Pr = \frac{\nu}{\kappa} = \frac{c_p \mu}{k}$. While containing the specific heat c_p, dynamic viscosity μ and the thermal conductivity k, this number is not dependent on a typical length scale and only dependent on the fluid and fluid state. Pr can therefore change for different fluids, temperature or other relevant parameters. For air this number is considered to be Pr=0.71 and for other gases similar values around 1 are found [45]. In our case momentum and heat dissipate at approximately the same rate through the fluid, but for example with liquid metals Pr is much smaller than one, since heat diffuses very quickly.

As previously mentioned, characterizing the flow in our cleanroom requires more than these dimensionless parameters. We also have to take into account the geometry of flow. Fig. 2.11b illustrates an airflow coming from the inlets in the ceiling impacting on the floor. Such a flow, where the flow from the inlet impacts on a perpendicular surface, is called a jet impingement flow. Since the same flow phenomenon happens in our cleanroom, a few of the characteristics are discussed in their distinctive region. After the inlet the flow can develop into a free jet flow. Here the entrainment of mass, momentum and energy takes place due to shear-driven interaction with the surrounding ambient air [46]. Fluid gets dragged into the jet on the sides, causing the jet to lose its kinetic energy, while increasing the total mass flow rate. The jet becomes broader in spatial direction and obtains a lower velocity. The distance over which this process takes place is called the potential core region. In this region the fluid velocity is approximately equal to the inlet velocity. A fully developed profile is obtained after the developing region. In the developing zone large shear stresses cause the axial velocity profile to decay in intensity [46]. The region where the jet hits on

the impingement surface (or target plate) is called the stagnation zone. Here the flow loses his axial velocity, causing a quick rise in the static pressure. After this, the flow moves radially outward along the wall at a lower velocity. In the case of multiple jets this flow along the wall will collide with the same radially outward flow from the opposite jet, causing an upwash of fluid dragged into vortices between the upwash and the original jet, see Fig. 2.12 for a schematic overview of multiple jets.
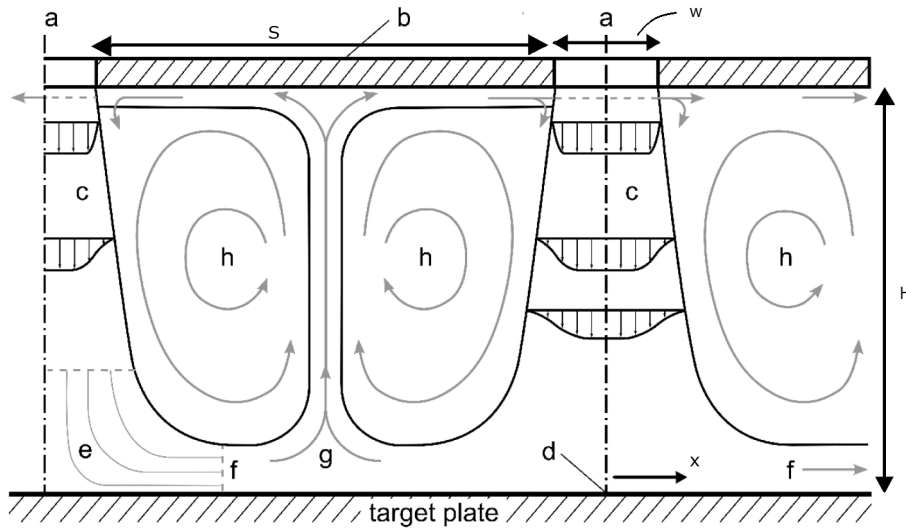

Figure 2.12 – Schematic overview of multiple jet impingement flows. Impingement flows from the inlets impacting on the floor, creating an upwash when colliding. Between the upwash and the inlets a recirculation zone is created. The high Reynolds number at the inlets and the merging of flows generates turbulence. The following components are labelled. (a) inlet, (b) target plate, (c) free jet, (d) stagnation point, (e) stagnation zone, (f) decelerated flow near the wall, (g) recirculating zone, (h) generated vortex, w jet exit width, S spacing between jet inlets, x distance from stagnation point and H is the distance from the inlet to target plate [47].

Parameters that should be taken into account for a jet impingement flow are turbulence at the jet exit, the distance to the impingement plate over the width of the jet exits (H/w) and the relative distance from the stagnation point (x/w) with x the distance from stagnation point, H the distance from the inlet to the target plate and w is the jet exit width. A large impact distance can lower the turbulence intensity at the impact plate. Another variable, in case of multiple jets, that should be considered is the spacing between the centers of two equal jets ($S+w$) that can play a role. For larger spacing the upwash and corresponding vortices generated by this upwash will not be as vigorous. In order to fully grasp the development of the flow in our geometry, the use of the Navier-Stokes equations is demanded.

2.8   Reynolds-Averaged Navier-Stokes equations

$$\frac{\partial u_i}{\partial x_i} = 0,$$
$$\rho\frac{\partial u_i}{\partial t} + \rho u_j\frac{\partial u_i}{\partial x_j} = -\frac{\partial p}{\partial x_i} + \frac{\partial}{\partial x_j}\left[\mu\left(\frac{\partial u_i}{\partial x_j} + \frac{\partial u_j}{\partial x_i}\right)\right].$$

(2.14)

The Navier-Stokes equations in Eq. 2.14 describe the motion of viscous Newtonian fluids and were first derived by Claude-Louis Navier and George Gabriel Stokes [48]. In these equations ρ is the density, p the pressure and μ the dynamic viscosity of the fluid. The terms u_i are the corresponding velocity components in the x, y and z direction and the x_i denote the three position coordinates (x,y,z). These equations prescribe conservation of momentum and conservation of mass for fluids and a viscosity term. This latter term is not included in the Euler equations for inviscid flow [49]. The Navier-Stokes equations often have no analytic solution, due to their mathematical structure. In some of these flows the Navier-Stokes equations can be numerically solved by computers, but for larger Reynolds numbers the computational effort rises dramatically as $\sim Re^{9/4}$, based on the requirement to resolve the Kolmogorov scale, assuming the flow is turbulent in the whole domain of interest [50]. The Kolmogorov scale are the smallest scales in turbulence where turbulent kinetic

energy dissipates in heat [44]. Turbulent kinetic energy is based on the sum of the variance of the velocity components. When simulating turbulence physics, a particular modeling approach is used in computational fluid dynamics (CFD) to keep down the computational effort: the Reynolds Averaged Navier-Stokes (RANS) model.

The RANS model uses the Reynolds decomposition, in which, for example the velocity, is separated into a time-averaged component U and a fluctuating component u'. So the time-dependent velocity would be decomposed as $u = U + u'$ and the pressure as $p = P + p'$. Obviously, the mean of the fluctuating component is equal to zero. By substituting the Reynolds decomposition for velocity components and the pressure into the Navier-Stokes equation we can derive the following set of equations for the mean flow.

$$\frac{\partial U_i}{\partial x_i} = 0,$$
$$\rho U_j \frac{\partial U_i}{\partial x_j} = -\frac{\partial P}{\partial x_i} + \frac{\partial}{\partial x_j}\left[\mu\left(\frac{\partial U_i}{\partial x_j} + \frac{\partial U_j}{\partial x_i}\right)\right] - \frac{\partial}{\partial x_j}\left(\rho\overline{u_i'u_j'}\right).$$

(2.15)

The last term $\rho\overline{u_i'u_j'}$ indicates the Reynolds stress term and is the main focus of the RANS-model. The '-' indicates the time-average operator. The physics which gives rise to Reynolds stress are different from viscous stress. Whereas the viscous stress term is related to the other flow properties by equations, depending on fluid properties (and having a molecular origin), the Reynolds stress is a result of the momentum transfer due to fluid velocity fluctuations.

For a general statistically steady three-dimensional flow we have more unknowns than the four independent equations for the velocity field. The Reynolds stress term already contains six unique stress terms. In order to close the RANS equations with the non-linear Reynolds stress term, many different turbulence models have been proposed. The one that is used in our simulation is the k-ε turbulence model, in which k is the turbulent kinetic energy and ε the rate of dissipation of turbulent kinetic energy [44, 51]. This model assumes that the ratio between the Reynolds stress and the mean rate of deformations (or strain rate) is the same in all directions, so called isotropic turbulent viscosity. This model is therefore only usable for fully turbulent flows. For modeling flows with the inclusion of wall effects the k-ω model is a more suitable option. Here ω is the specific rate of dissipation of turbulent kinetic energy into internal thermal energy per unit volume and time, often denoted as $\omega = \frac{\varepsilon}{k}$[44, 51]. ω is therefore referred to as the turbulence frequency due to the unit of 1/s. In this thesis we will only focus on the first mentioned model due to the large scale of the flow compared to the scale of wall effects. Since the k-ε model has many unknowns and non-quantifiable terms, we use the 'Standard k-ε model' for a more practical approach [44]. The two equations that correspond with this model can be found in Eq. 2.16 with the top equation belonging to turbulent kinetic energy k and the lower to the dissipation rate ε,

$$\frac{\partial(\rho k)}{\partial t} + \frac{\partial(\rho k u_i)}{\partial x_i} = \frac{\partial}{\partial x_j}\left[\frac{\mu_t}{\sigma_k}\frac{\partial k}{\partial x_j}\right] + 2\mu_t E_{ij}E_{ij} - \rho\varepsilon,$$
$$\frac{\partial(\rho\varepsilon)}{\partial t} + \frac{\partial(\rho\varepsilon u_i)}{\partial x_i} = \frac{\partial}{\partial x_j}\left[\frac{\mu_t}{\sigma_\varepsilon}\frac{\partial\varepsilon}{\partial x_j}\right] + C_{1\varepsilon}\frac{\varepsilon}{k}2\mu_t E_{ij}E_{ij} - C_{2\varepsilon}\rho\frac{\varepsilon^2}{k}.$$

(2.16)

From left to right these terms belong to: rate of change in time, advection, diffusion, rate of production and rate of destruction of k and ε with similar structure as equation 2.15. $\mu_t = \rho C_\mu \frac{k^2}{\varepsilon}$ is the eddy viscosity and E_{ij} is the rate of deformation in matrix form, representing the expansion or compression of the fluid. The other variables σ_k, σ_ε, $C_{1\varepsilon}$ and $C_{2\varepsilon}$ have been empirically found values for a wide range of turbulent flows and universally set at σ_k=1.00, σ_ε=1.30, C_μ=0.09, $C_{1\varepsilon}$=1.44 and $C_{2\varepsilon}$=1.92[44]. The two σ's are the turbulent Prandtl numbers for k and ε. With these known constants the k-ε model is a very robust model with a reasonable accuracy. For the use of jets the 'Realizable k-ε model' is often used. The term "realizable" means that the model satisfies certain mathematical constraints on the Reynolds stresses, consistent with the physics of turbulent flows. This means that C_μ in the definition of μ_t is not assumed to be a constant, but based on the mean deformation and turbulence by k and ε[52]. A benefit of the realizable k-ε model is that it accurately predicts the spreading rate of both planar and round jets. It is also

superior in performance for flows involving rotation, boundary layers under strong adverse pressure gradients, separation, and recirculation [52]. Because this model has shown great improvement in accurately modeling turbulent flows, combining the above mentioned elements leads to an accurate representation of the flow field.

2.9   Lagrangian modeling

Particle contamination in cleanrooms closely relates to particle dispersion and modeling can be achieved by tracking the individual particles and their trajectories. A common and widely used approach is the Lagrangian model, which tracks individual particles and their trajectories. The determination of complete trajectories is computational heavy, since at every time step the interaction with the fluid properties is computed and the resulting movement implemented for each individual particle [53]. A way to circumvent this is by using parcels. Parcels are a group of identical particles which are statistically averaged to obtain the most probable trajectory [54]. Individual particles might deviate in their trajectories and this statistical average illustrates the most feasible outcome for many particles creating a more tractable model. The Lagrangian method solves the following equations of motion to obtain the particle trajectories for a particle with mass m_p and velocity v_p in case of no collisions between particles and no charge

$$m_p \frac{dv_p}{dt} = F_d + F_g + F_p + F_{vm} + F_B + F_{Ba} + F_s, \tag{2.17}$$

consisting of the drag force F_d, gravity F_g, pressure gradient force F_p, virtual mass F_{vm}, the Brownian force F_B, the Basset Force F_{Ba} and the Saffman's lift force F_s. This simplification is allowed since we are dealing with particles of micron size, resulting often in a particle Reynolds number $Re_p < 1$. In that case, we consider the particle to be in the Stokes regime [55]. The Stokes drag force and gravity for spherical particles can be described as

$$F_d = 6\pi \mu v_s R, \tag{2.18}$$

$$F_g = m_p \cdot g = V_p \rho g. \tag{2.19}$$

In Eq. 2.18, v_s the particle slip velocity as $v_s = v - v_p$, the difference between the instantaneous velocity of the fluid and the particle velocity, μ is the fluid viscosity and R the particle radius. For Eq. 2.19 V_p is the particle volume and g is the universal gravitational constant. In the case of particles with a density ρ_p much higher than the surrounding fluid density ρ, the virtual mass, the Basset force and the pressure force are small and can be neglected, see Zhao [56]. In our case $\rho/\rho_p \approx 1/1200$, so compared to the drag force these can be neglected. The resulting approximations are given in Table 2.2.

Table 2.2 – Force amplitudes relative to F_d due to high ρ_p/ρ [56].

Force	Relative to F_d
F_d	1
F_p	$\frac{\rho a_a}{\rho_p a_p} \approx \frac{\rho}{\rho_p}$
F_{vm}	$\frac{1\rho}{2\rho_p}$
F_{Ba}	$\left(\frac{19\rho\tau_r}{C_D \pi \rho_p t} \right)^{\frac{1}{2}}$
F_s	in 3D flow : $\frac{0.288 d_p C_c d_{ij}}{v^{0.5}(d_{lk} d_{kl})^{0.25}}$

with C_c being the Cunningham correction factor and d_{ij} the deformation tensor. In the case of $Re < 1$ the Cunningham correction factor approaches $24/Re$ and it can be seen that this lift force becomes only relevant for large particles in a high shear flow close to the walls, so we can neglect

it [53, 56]. The Brownian force becomes important for sub-micrometer particles and is a result of random movements due to particle collisions with the surrounding fluid. In order to determine its relevance we use the particle Strouhal number Sr_p. to compare the relevant time scales for the external forces $\tau_d = R/v_d$ and Brownian motion $\tau_B = \frac{R^2}{D}$, with v_d the drift velocity and $D = \mu k_B T$ the diffusion coefficient, k_B the Boltzmann constant and T the temperature.

$$Sr_p = \frac{\tau_d}{\tau_B} = \frac{D}{R \cdot v_d} = \frac{k_B T}{R \cdot F}, \tag{2.20}$$

where we use $v_d = \mu F$[57], with F being the external force, for example gravity. Brownian motion becomes irrelevant for $Sr_p \ll 1$, so for particle radius R holds

$$R \gg \frac{k_B T}{F}. \tag{2.21}$$

When comparing to gravity at 20 °C we obtain

$$R \gg \frac{k_B T}{\frac{4}{3}\pi R^3 (\rho_p - \rho) g} \tag{2.22}$$

leading to $R \gg \sqrt[4]{3 k_B T / 4\pi (\rho_p - \rho) g}$, which is $R \gg \mathcal{O}\,(1\,\mu m)$. This means that for simulations with particles of 1 µm and higher we can leave out F_B for Lagrangian modeling and still have accurate results, since gravity is a more dominant force. The equations of motion become

$$m_p \frac{dv_p}{dt} = F_d + F_g. \tag{2.23}$$

Another dimensionless number to characterise the behaviour of particles suspended in a fluid is the Stokes number. The Stokes number is defined as

$$St = \frac{t_0 \cdot u_0}{l_0}, \tag{2.24}$$

with in case of a Stokes flow t_0 is the relaxation time of the particle, u_0 is the fluid velocity of the flow well away from the obstacle and l_0 the characteristic dimension of the obstacle (often the diameter of the obstacle)[58]. t_0 is given by

$$t_0 = \frac{\rho_p d_p^2}{18\mu}. \tag{2.25}$$

The relaxation time, or particle response time, is the time required for particle to respond to a change of the fluid's velocity such that when the surrounding fluid velocity changes, as it might when encountering an object, the particle follows the fluid and flows around the object, as stated by Pruisner [59]. When $St \ll 1$, particles tend to follow the streamlines (passive particles) and in the case of a $St \gg 1$ particles have a large inertia and ignore the streamlines. Between these extremes, particles do not ignore but deviate from the streamlines. For small particles, the diameter of particles is in microns, t_0 will be small as derived from equation 2.25 and St becomes small. For a particle of 1 µm $St < 10^{-5}$. Deviating from the streamlines and settling of particles on a surface is dependent on the particle radius. For particles with a $R \geq 10\,\mu m$ gravitational settling caused 80% of the surface deposition [60]. The other 20% involves Brownian motion and electrostatic attraction. Gravity remains an important force for deposition down to 0.5 µm. Since our Stokes number is low and gravity is negligible for most particles of micron size in the cleanroom, we are often dealing with passive particles that follow the streamlines. In case of passive particles, solving the flow accurately leads to more probable particle trajectories.

Wall interaction in Lagrangian modeling can be specified per boundary surface [54]. Particles either rebound from the surface or stick to the surface. How and when the particle rebounds or escapes is not only dependent on the velocity and size of the particle, but also highly dependent on the material and roughness of the surface (in our case the top of a table). The last characteristic is often only experimentally verifiable by zooming in on the structure. For modeling, one can set

conditions for rebound to occur. These conditions involve the probability a particle rebounds or escapes and the momentum loss for a particle. For the latter, we base this on the coefficient of restitution which is defined as $e_r = |\vec{v_f}|/|\vec{v_i}|$ [54]. The coefficient indicates the fraction of momentum from the initial velocity transferred to the final velocity after collision. Without experimental validation, giving an exact number to the probability of rebound and the coefficient of restitution is difficult and often left out by researchers. Because no literature can be found on (experimentally) defined values for cleanrooms, we assume particles to rebound and no loss of momentum. In the case a particle deposits on the top of a table we assume it sticks to the surface.

2.10 Mesh independence study

In 3D modeling, a mesh is the collection of faces, vertices and edges that define the modeled geometry. In general, a finer mesh gives more accurate results at the cost of computational expense, possibly impeding convergence to a steady state. Choosing a correct mesh size is challenging and is studied in mesh independence study (MIS). In this field, one looks at the change of parameters when altering the mesh, in order to limit their change, for example a few percent of compared to the finest mesh. Other parameters that are often compared involve, pressure drop, mass flow through planes or velocity profiles. Plotting the variables after a certain number of iterations as function of the number of cells gives an indication of the minimal cell size needed. After the mesh independence study, refinements in sections where the flow is difficult to model can be made.

In order to correctly determine the most probable trajectories in our geometry the MIS study provides a correctly determined mesh that is able to prescribe the flow field. Chang [61] compared the Lagrangian method with the Eulerian model to determine the Particle Residence Time (PRT) in indoor environments with instantaneous and continuous injection of particles of 1 and 10 µm. He determined that the Lagrangian approach can give a more accurate prediction on the PRT compared to the Eulerian approach. Lai [62] used Lagrangian modeling to determine particle deposition in an indoor environment and concluded that the Lagrangian modeling agreed well with his empirical model for particle deposition for particles in the range of 0.01 to 10 µm. Since we are using passive 1 µm particles as injected particles we can say that the Lagrangian model provides a decent approach to determine the PRT of particles in the steady solution of our flow in the cleanroom segment.

3 Method

For the numerical simulation of the particle counter, the numerical algorithm that solves the Mie Scattering equations defined in sec. 2.1, 2.2 and 2.3 was written in MATLAB programming language. As stated earlier, two types of investigations were carried out. First, the properties of Mie scattering and its dependencies on radius and other parameters are investigated. After that, recreating a signal of particles passing through a sensor viewing volume and inspecting requirements, such as a minimum sampling frequency, to fully reconstruct the signal is being carried out for different light sources.

In the second part the location of where in the cleanroom such a sensor should be placed is investigated. Examining the flow and particle dispersion inside the cleanroom is done by two injection types. For statistical representation an injection plane that releases thousands of particles is used and for simulating full trajectories an injection line probe releases particles from a fixed position. For the first case, research is done on where particles deposit. In the second part, a property such as the particle residence time (PRT) inside the cleanroom is reviewed.

3.1 Numerical simulation of particle counting

Reproducing a possible theoretical signal that reaches a photodetector when particles pass through a measurement volume requires tracking of particles. A schematic overview of the particle flow through such a light beam is given in Fig. 3.1, illustrating individual particles passing through the duct.
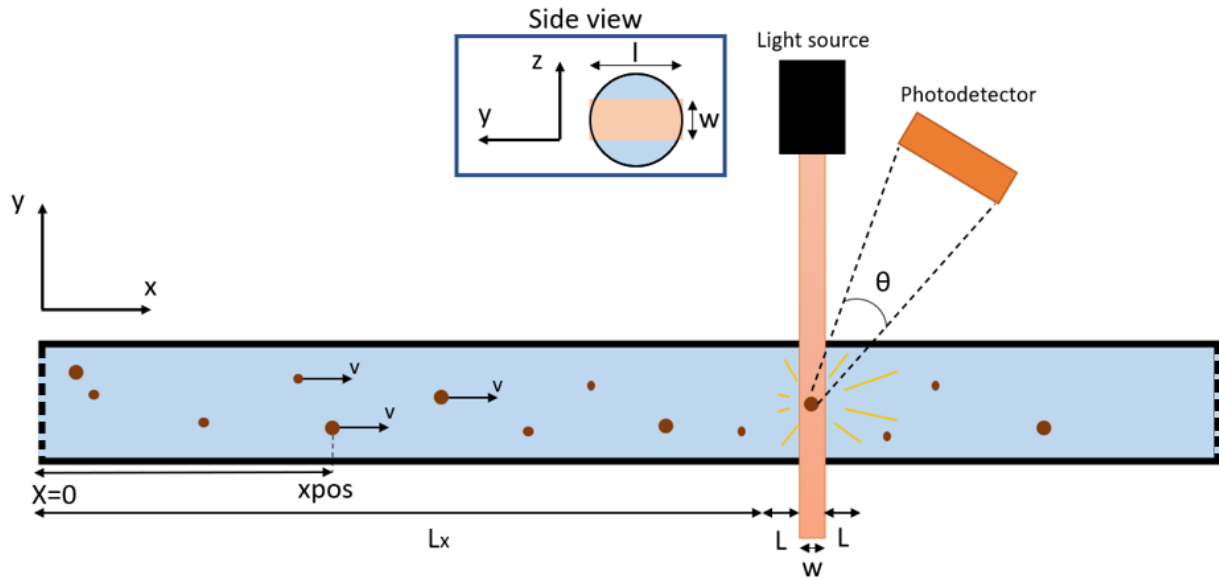
Figure 3.1 – Schematic drawing of the simulated particle flow. Particles enter the sensor on the left with a constant velocity v from an initial position xpos in L_x. When they pass through the light beam, Mie scattering takes place. The intensity can be measured by a photodector. In the side view, the frontal area of the viewing volume can be approximated by a rectangle. w is the width and l the length of the viewing volume. L is a specified distance to make sure particles their initial position is not in the light beam. θ is the detection angle of the photodetector.

In the most simple case particles with different diameter come into the sensor area at a velocity v based on the flow rate and the area of the rectangular duct. In real life cases, the velocities will fluctuate slightly, but since the flow rate is kept constant in the sensor, we can neglect this. The process of tracking particles and calculating their scattering pattern is described below.

1. First we define a concentration of particles in μg/m^3 and an external volume in m^3, which we fill with randomly selected particles from a certain particle size distribution function based on 'Arizona Road Dust' (and thus different spherical volume) until the desired concentration

is reached. Arizona Road Dust is a manufactured particle size distribution of dust used for calibration of sensors.

2. Then we distribute these particles randomly with uniform spatial distribution in L_x in which L_x is the x component based on the external volume divided by the area of the laser beam. This in order to preserve the same volume and therefore the same concentration.

3. Each particle is given an initial constant velocity and with the sampling frequency we can track each particle at each instance.

4. We verify if the position of the particle including its radius is within the measurement area.

5. Lastly we determine the Mie scattering intensity for each particle according to the following equation

$$I(\theta, r) = \underbrace{\frac{I_0}{2 \cdot k_0^2 \cdot l_d^2} \left(S_1(\theta)^2 + S_2(\theta)^2\right)}_{\text{Mie scattering}} \cdot \underbrace{\frac{A_{\text{inlaser}}}{A_{\text{TotalArea}}}}_{\text{partial scattering}} \cdot \underbrace{\exp\left(\frac{-2r^2}{w_0^2}\right)}_{\text{Gaussian}} \cdot \underbrace{\exp\left(-y \cdot l_d\right)}_{\text{Light extinction}}, \qquad (3.1)$$

in which the Mie scattering term is already discussed in Eq. 2.11, $A_{inlaser}$ the frontal area of a particle partially in the laser and $A_{TotalArea}$ the area of a particle when it is completely in the laser, r the radial distance from the center of the laser, w_0 is the radius at which the intensity falls to $1/e^2$ of the axial values. We assume w_0 to be at $2/3$ of the maximum beam width w[14, 40, 41]. With regard to light extinction, y equals the extinction coefficient and l_d the length to the detector [63], which is 12.5 mm. The SGPS project is a sensor that uses nephelometry for particle counting made by Prodrive Technologies. We can use already obtained data by this sensor for comparison of the scattering intensity values [64]. All quantities are based on the SGPS project within Prodrive Technologies.

The front view of the intersection of the laser beam with the flow (the viewing volume cross section) can be approximated by a 2D rectangle of area ($l \times w$) in which l is the diameter of the cross section and w the diameter of the laser beam intersecting with the flow, or the diameter of the laser beam. We assume that all particles move through the laser at a horizontal line. In the real situation, the viewing volume is much smaller than the flow volume, as explained in Fig. 2.8, leading to particles not passing through the viewing volume. When the concentration of particles is too high, the viewing volume needs to be smaller in order to maintain one particle in the viewing volume. Therefore particles can move past the viewing volume. Then using statistics the total amount of particles in the whole flow is determined by multiplying with the fraction of the left out volume. We define l=4 mm for the flow and w=1 mm. Once the particles have an initial position and velocity we know when particles enter the laser beam. In order to make sure that particles need to move into the laser and are not giving an initial position half inside the laser, a length L is defined in front and after the laser beam. Since most particles inside a cleanroom are within 0.1 and 10 µm, L should be larger than half of the largest particle to not be in the laser beam. With the sampling frequency f and a total sampling time $t_{sampling}$, we can track the position of all individual particles at each time instance. Overlap in intensity peaks between particles is possible due to random initial positions. A high enough sample frequency is required to fully resolve the intensity peaks of the particles, see Sec. 2.4.

We used a concentration of 10 µg/m^3, a wavelength of λ=663 nm and a power of 1 mW. Other important values such as dust density and complex refractive index were based on the Arizona Road dust characteristics [65]. The Arizona Road dust particles are characterized by a refractive index of $m = 1.46$ and bulk density of 2650 kg/m^3. For the photodetector the detection angle is varied, but the distance is kept the same at 12.5 mm. Here we assume that all light in the detection angle is perfectly focused on the photodetector and no signal is lost. The reason for a laser as a possible light source is their low cost, collimated light beam and built-in feedback control by means of a photodiode. In this simulation we used a beam width of 1 mm, large enough to grasp the Gaussian character and give a clear indication of overlap. Lower limits for this application are in the range of (tens of) micrometers. When multiple particles are in the measurement volume at the same time,

22

the scattering intensities are added, since we assume coherent scattering. The difference in path length to the photodetector, due to a variation in the x position in the laser beam, is assumed to be negligible.

As seen in Eq. 3.1, before the light reaches the detector there are a couple of factors that bring down the intensity. In case the light source is a laser, the Gaussian character seen from the center of the laser causes an intensity drop from the light source when particles are not in the center of the laser, see Sec. 2.5. Another effect that takes place is scattering from a particle with partial beam illumination, which we call partial scattering. There are time steps in which particles are not completely in the laser beam, but only a part of the surface scatters the light. From our simulations it was found that this effect is very minimal, since it only takes place while entering or leaving the laser beam. Entering and leaving the laser is hereby defined by the maximum beam width. For example, with a particle of $1\,\mu m$ and a velocity of 1 m/s the time partial scattering takes place, when entering, is $\frac{1 \cdot 10^{-6} m}{1 m/s} \approx 10^{-6}$ s. Because we are using a beam width which is a thousand times larger. One can imagine, when using smaller viewing volumes this process is of larger importance. In theory, you would be able to determine particle size from partial scattering, since a larger size particle has a longer time in which partial scattering takes place, but in reality this is not possible due to noise and low intensity levels and not high enough sampling frequency. Therefore, we will not further discuss this effect. A third effect that occurs is light extinction, which causes light to decrease due to absorption of the medium and the spreading of light over a larger surface [63]. Combining these three factors we get the intensity of the scattered light on the photodetector formula according to Eq. 3.1. Investigating the wavelength and radius dependence combined with the corresponding angular distribution of light around a particle will be the key elements in order to determine a useful relationship between intensity and particle size. For particle sensor purposes this relationship will be reversed to estimate the particle size and the possible corresponding error.

3.2 Air flow in the cleanroom

For investigating the air flow and particle dispersion in the cleanroom, 3D simulations in Star-CCM+ were done. Whereas the total cleanroom at Prodrive Technologies involves many squared metres, we limit ourselves to a repetitive geometry in the cleanroom, where there is a high risk in contamination. This part involves two pillars with outlets near the floor on each of the four sides with in between these pillars desks with equipment. On these desks product assembly inside the cleanroom takes place. This makes the desks a high risk area for contamination of the product. Filtered air flows into the cleanroom via inlets from the ceiling. Because of the higher restriction on particle concentration, we restrict ourselves toe restrict ourselves to the ISO-5 part of the cleanroom. Besides that the flow profile from the inlets in ISO-5 cleanroom is more straightforward than an ISO-6 cleanroom, see Sec. 2.6. Fig. 3.2 illustrates a schematic 2D overview to get a clear understanding of the direction of the flow and the important dimensions.
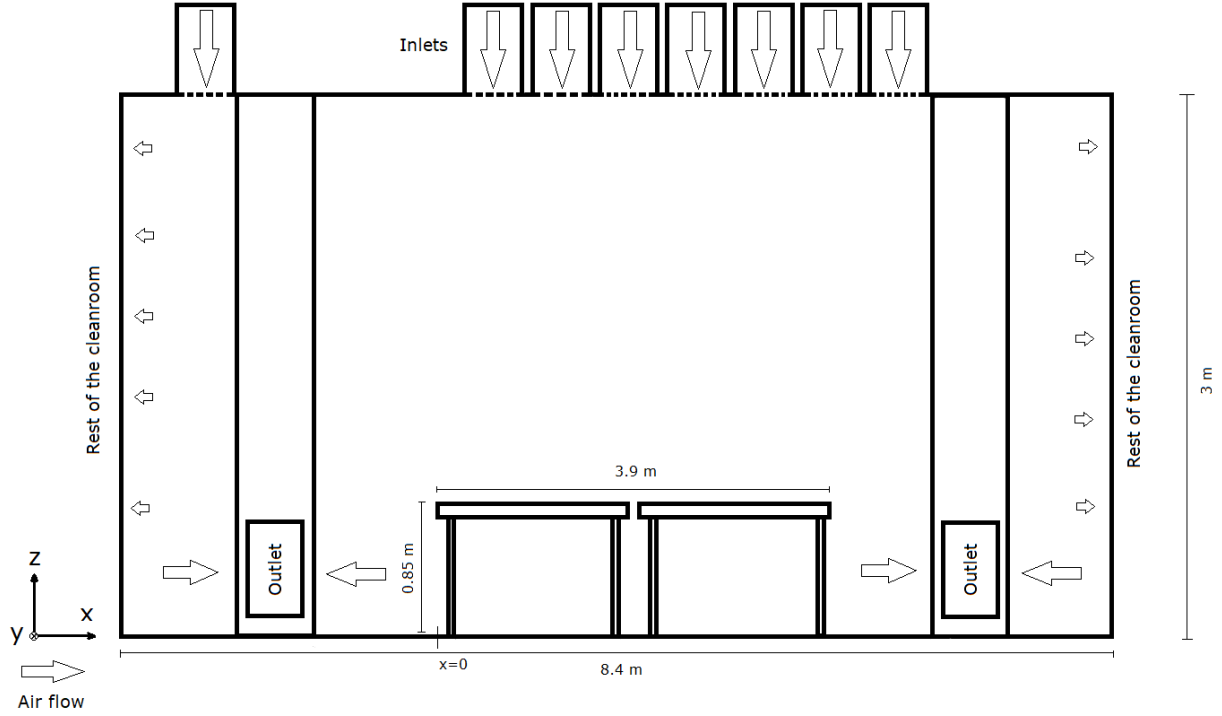
Figure 3.2 – Schematic 2D overview of the geometry with tables. The arrows indicate the airflow from the inlets towards the outlets and the rest of the cleanroom. x=0 is located at the left side of the first table.

In Fig. 3.2 air enters via the air inlets in the ceiling and leaves the cleanroom via the air outlets in the pillars and at the bottom to the rest of the cleanroom. For the inlets, the velocity is set at 0.5 m/s per inlet and for the outlets in the pillars the velocity is experimentally measured to be 0.47 m/s per vent. Since in the real situation we have an opposing line of inlets at a certain distance, separate simulations were done, in which two inlets were placed opposite each other at variable distance. These showed that the upwash due to the collision of flow from the inlets and from the opposite inlets would be negligible. Therefore the other inlets are not incorporated our geometry. Because of this a pressure outlet boundary condition on the sides was the best option at the boundary surface to mimic the flow field. Here, air flows from our segment of the cleanroom to the rest of the cleanroom. From the simulations a pressure outlet at 0.0 Pa was defined, which acts as a plane through which the fluid flows.

The air is considered to be T=20° C, causing ρ=1.204 kg/m^3, μ=1.813·10^{-5} Pa/s and ν=1.506·10^{-5} m^2/s at atmospheric pressure [66]. Based on a velocity of 0.5 m/s and a diameter of the inlet equal to 0.58 m, the Reynolds number is $\approx$ 20,000. Since a lot of mixing occurs between the multiple inlets located besides each other and the flow is an impingement flow, we are dealing with a turbulent flow. This turbulent flow is described by the k-ε model, see Sec. 2.8. Besides this, the particle trajectories often take place above the table, so wall effects become less relevant, strengthening our choice of the k-ε model. In order to define the turbulence intensity I and the viscosity ratio β, which is the ratio between the turbulent viscosity and the molecular dynamic viscosity, we use the following equations for a fully developed duct flow:

$$I = 0.16 \cdot Re_{d_h}^{-\frac{1}{8}}, \tag{3.2}$$

$$k = \frac{3}{2}(UI)^2, \tag{3.3}$$

$$\beta = \frac{\rho k^2}{\mu \varepsilon}. \tag{3.4}$$

With the Reynolds number using the hydraulic diameter of the inlets, the turbulence intensity was set at 10% of the velocity components and the viscosity ratio is set at 30, also taking into account that flow at the inlets in our geometry is not a fully developed duct flow [44, 67]. Based on

$$\delta(y) \sim \frac{y}{\sqrt{Re_y}}, \tag{3.5}$$

the boundary layer thickness δ at the table (region of interest) was estimated at approximately 0.0053 cm[1] based on the Reynolds number Re_y above the table using y, the length of the table in y-direction of 0.7 m, as a typical length scale in the calculation of Re [44, 68].

Other important dimensions and figures of the 3D geometries can be found in Tab. A.1. Our initial simulations showed that changing the boundary layer did not change the particle trajectories significantly, so for the simulations the boundary layer of 1 cm was used to make particles able to deposit on the table. The constant temperature and pressure allows for the definition of a constant density of air in the cleanroom.

At first instance, we kept the geometry simple in order to understand the flow path. This means only two tables in the center. The flow will impinge a bit on the table since in the yz-plane the inlets are slightly above the right side of the tables. When extending the geometry, equipment and cabinets in the form of rectangles are rectangles on and under the desks, see chapter 4.

3.2.1 Quantifying particle contamination and dispersion

For the Lagrangian modeling of particle trajectories two options are considered. In the first a statistical analysis is done using the ensemble theory. Since in many simulations all the individual particles are identical and independent of each other ensemble theory holds here. By injecting approximately 30.000 particles across the whole cleanroom we can see if particles deposit on or around the tables and contaminate. We inject particles with a velocity in the positive y-direction at 0.1 m/s, which is at the speed of a slow cough by personnel [69]. Simulating the full trajectory of this many particles is computationally expensive, therefore we use the parcel depletion criterion. This means that when a parcel reaches set conditions the parcel is deleted from the simulation. The following conditions were set. Deposition takes place towards the table, so we are only interested in particles moving towards the table. Particles towards the ceiling, underneath the table or away from our region of interest are deleted. Some particles stay in the recirculation zone above the table and never drop to the table. In order to still quantify particle dispersion, deposition planes at 20 cm above the table were used for intersection studies. The 20 cm is based on the height of handling the products. Particles at this distance from the table can drop down and contaminate the product. From here on, we assume that an intersection above the table with this plane corresponds to a contamination of the product. The trajectories are calculated with 'perfect' conditions. In real life many small changes in conditions, such as the velocity components of the flow field, could take place causing the trajectory to deviate from the simulated path. The assumption of not colliding into each other is justified by the fact that a cleanroom does not contain a high particle density. Fig. 3.3a depicts the above described situation.

---

[1]Our initial calculations yielded 0.04 m, in later revisions we found Eq. 3.5 to be erroneous and the actual value should be 0.0053 m. Because the boundary layer thickness is not significant for our purposes we had already put it at 0.01 m, which was fortunately in the right direction.
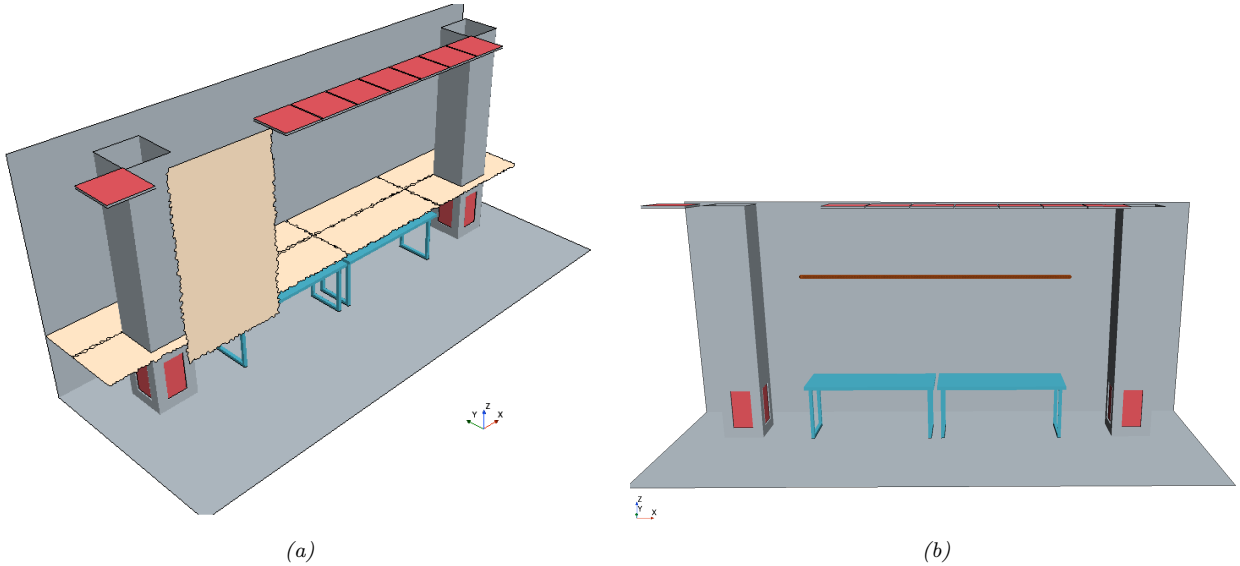
Figure 3.3 – a) 3D view of the model indicating the nine different planes, eight horizontal and one vertical between the inlets. The intersections with the trajectories are a measure for contamination or for the vertical plane how many particles escape the volume above the table. The blue parts are the tables, the top red squares are the inlets and in the pillars the outlets are depicted. b) The injector, indicated in brown, with 500 injection points above the table between x=0.0 and x=3.9 m for the line probe simulations at z=2.5 m.

Another option used in our simulations is 500 point injectors from which particles are released between $0 \le x \le 3.9$ m. Per injection point we can vary the amount of released particles and the diameter/particle size distribution of particles. For simulations with constant particle size, sizes of 1 µm were used. For the uniform particle size distributions two ranges were used: From 0.1 µm to 10 µm and the second distribution 1 µm to 50 µm. The actual particle size distribution is much more focused towards the small particles, but illustrating the effects on 'large' particles requires a uniform distribution. The probe line was set at z=1.6 m, due to humans being the largest contamination source in a cleanroom as mentioned in section 2.6, based on the height of a human mouth. Often cleanroom staff have to wear protective gear that covers most of the body, except the face. The y values of the injectors will be varied to check the influence of the position regarding to the table on the dispersion of particles. This mimics the positioning of a person above-, close to- or far from the table. The injector illustrated in brown in Fig. 3.3b are 500 point injectors, but since they separated less than 1 cm they appear as a line. Furthermore one vertical plane between the inlets on the left side is placed to verify how many particles escape the circulation above the table (in the interesting region) towards the rest of the cleanroom. Simulating the full trajectory of up to 500 or 4000 particles gives an indication of the duration particles stay above the table or in the cleanroom. Using the particle residence time (PRT) could help in a search for optimizing the cleanroom design. Although we are simulating possible trajectories, with a lot of uncertainties, they could provide insight about the working of the vents and inlets combined with the particles recirculating in the cleanroom.

For the modeling of the particle trajectories several assumptions are made. The solid particles are assumed perfectly spherical with a constant density of 1200 kg/m^3[60]. Forces that are taking into account are gravity, drag force and the pressure gradient force. Although the pressure gradient force was determined to be less relevant for our equation of motion, Star-CCM+ automatically incorporates it in Lagrangian modeling. Drag force is determined by Eq. 2.18. We can leave out the other terms as mentioned in Sec. 2.9.

3.2.2 Defining the correct mesh

In order to grasp the geometry correctly we use a polyhedral mesher. Polyhedral cells come in various shapes and sizes and are therefore easy to implement in a geometry. The benefit of polyhedral cells is the approximation of gradients due to the many neighbouring cells per individual cell, compared to tetrahedral and hexahedral mesh elements [70]. This increase in neighbours allows mass transfer over non-perpendicular faces, leading to more accurate results. Because these

cells are adjustable and stretchable cells, Star-CCM+ optimizes the cells better leading to more numerically stable models.
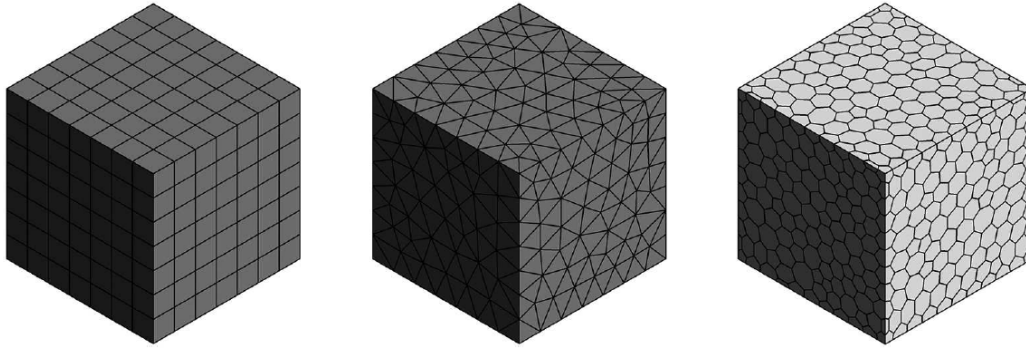

Figure 3.4 – Three different meshes from left to right a hexahedral, tetrahedral and polyhedral mesh. Indicating the increased amount of neighbours for a polyhedral mesh leading to a more numerically stable solution [70]

The base size is determined by the mesh independence study. The minimal base size is set at one third of the base size. Because there is no perfect template in defining a mesh, a visual inspection of the mesh combined with the development of variables in varying mesh sizes is required. We refine our mesh relatively high in the middle, and low on the outsides, because wall effects are less relevant in our case. Therefore, values for surface and volume growth rates were set at 5%. Since our particle trajectories are happening above the table in the middle of the volume, we do not want our cells to be to large in the middle.

(a) 3D view

(b) Side view
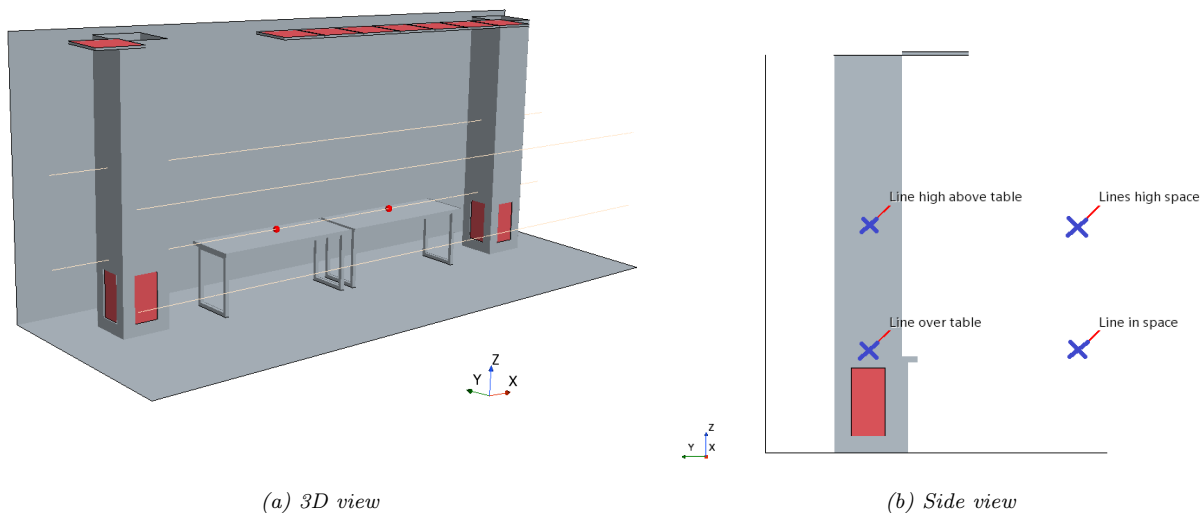
Figure 3.5 – Four probe lines used for the mesh independence study with velocity profiles from two different views. The beige lines in a) indicate the probe lines.

For defining the correct base size, we used four velocity probe lines at two different heights and two different y position, based on the MIS in papers from Yun-Chun Tung et al. and Lai [71, 62]. We concluded that 0.03 m as a base size was good enough, but needed refinement above the table. The total number of cells after refinement is above 2.2 million cells. In Fig. 3.6 it can be seen that a base size larger than 0.03 m does not portray the velocity field correctly. A base size of 0.04 m portrays velocities approximately 15% lower than the finer meshes for $0 \leq x \leq 4$. This is high above the allowed error limit of 5 percent. If 0.04 m would not be able to portray the flow field correctly, larger base sizes are not an option. For base sizes of 0.06 m and 0.07 m, the velocities are off around 20% for $2.5 \leq x \leq 3.5$. The base size of 0.03 m corresponds very well with the finer meshes often staying within 4% of the finest mesh of 0.02 m and 0.015 m illustrated in Fig. 3.7a and 3.7b where a good characterization of the flow can be noticed. A refinement of maximum cell size of 0.03 m seen in Fig. A.1 above the table solved the chaotic discrepancies in figure 3.8a. Without refinement Star-CCM+ is not able to solve the solutions in each cell correctly due to the cells being too large

at 0.09 m. Since our region of interest is above the table, the inconsistency of the graphs in Fig. 3.8b can be neglected due to low velocity values below 0.05 m/s and being on the other side of the inlets, which is not our region of interest. From here on, we continue with the base size of 0.03 m with the added refinement above the table, the mesh can be found in Fig. A.1.
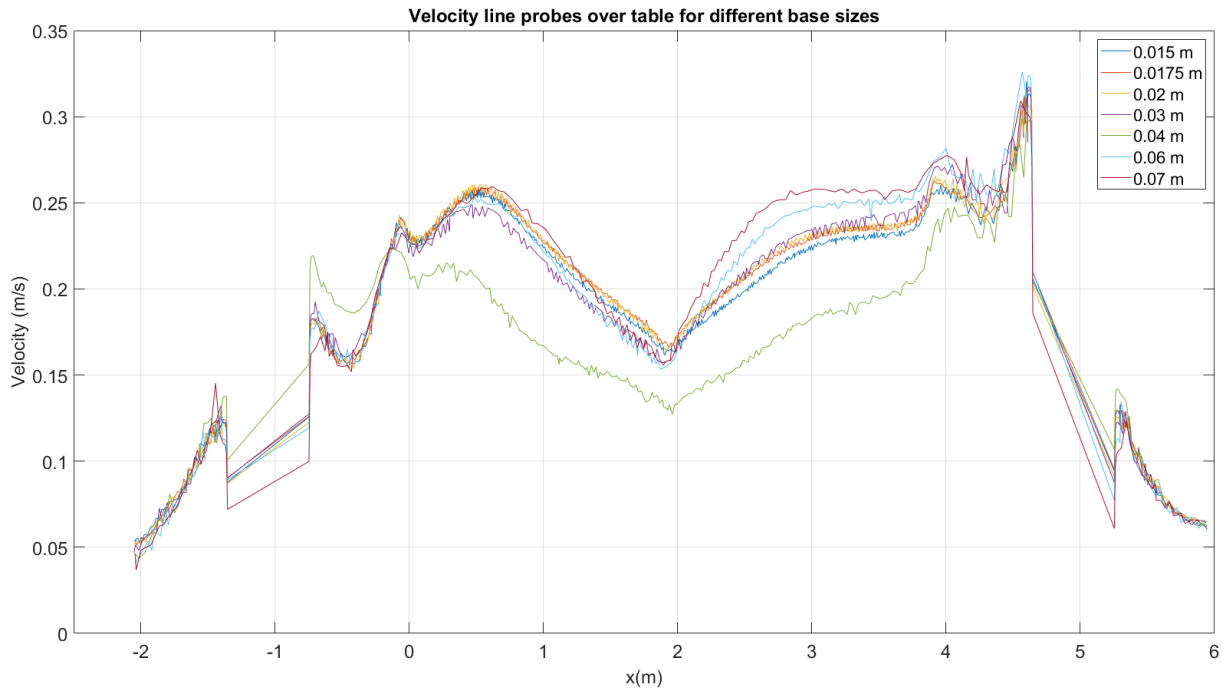

Figure 3.6 – The same velocity profile for different base sizes over the table at z=0.9 m. For a base size of 0.04 m and larger the model is not able to describe the flow correctly, the same as the refined mesh. From here on we can conclude that a base size of 0.03 m or lower is required to stay within the prescribed limits for correctly describing the flow. Velocities of base sizes of 0.04 m(too low) and 0.06/0.07 m(too high) are out of the designated error limit of 5%.
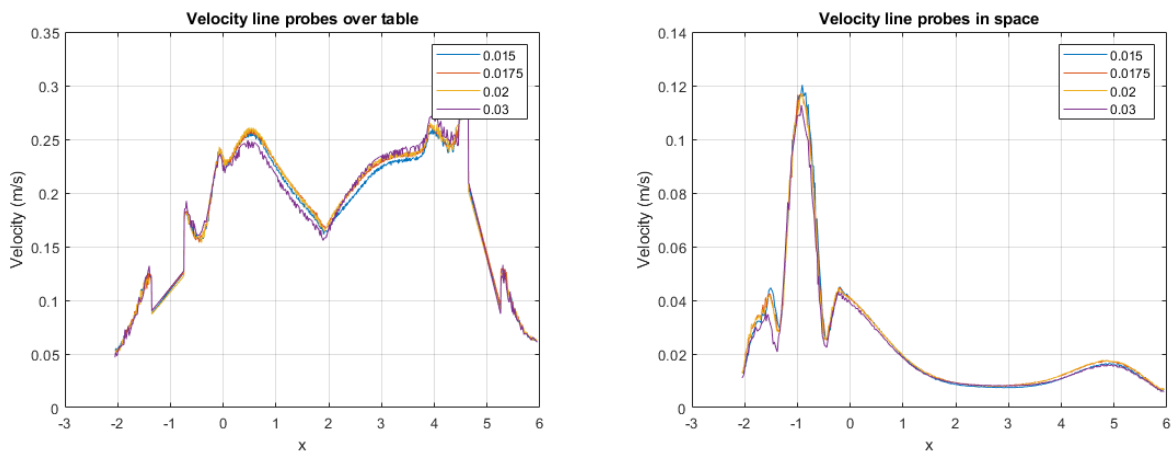
(a) Above the table z=0.9 m. *(b) In space z=0.9 m.*

Figure 3.7 – Velocity line probe at four different base sizes for z=0.9 m indicating that base size of 0.03 m is good enough to describe the flow, because the probe lines correspond well with the finer mesh.
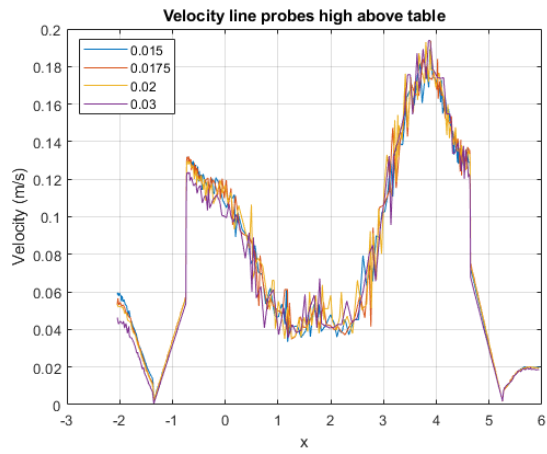
(a) Above the table z=2.0 m.
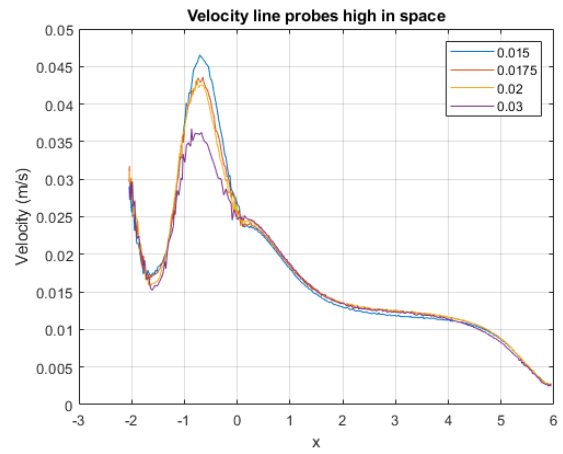
(b) In space z=2.0 m.

Figure 3.8 – a) Velocity line probe at four different base sizes for z=2.0 m indicating that base size of 0.03 m is good enough to describe the flow. The discrepancies come from the fact that the cell sizes are too large. b) We see a discrepancy at x=-0.5 m. The velocity values are really low and the region of the probe line is not in the area of interest.

4   Results & Discussion

4.1   Light simulations

In this chapter the numerical simulation of the particle counting sensor is presented first. What light source suits best at what detection angle in order to find a one-to-one relation between intensity and R is one of the key question for particle counting. How is the scattered intensity dependent on the particle radius R and how can we distinguish particles that enter the laser beam at the same time are the main focuses. First, we highlight the process of finding this relation, resulting in a possible correct solution at the end of this section about light simulations.

4.1.1   Intensity signal simulation

In the interest of understanding Mie scattering of particles moving through a light beam, a theoretical signal that would reach the photodetector was modelled. The used configuration is elaborated on in Sec. 3.1. After tracking the Arizona Road dust particles through the duct, the particle scatters a certain amount of light when entering the laser beam. Using an adaptation of the scripts from Mätzler we can determine the Mie scattering intensity. Quantifying how much intensity arrives at the detector is what we are going to investigate. A typical intensity signal with a laser as light source is illustrated in Fig. 4.1. Here the laser has a wavelength of λ=663 nm with a detection angle of 75 to 85 degrees. The sampling frequency is 10 MHz and flow rate 2 L/min with a particle concentration of $10\,\mu\text{g/m}^3$.
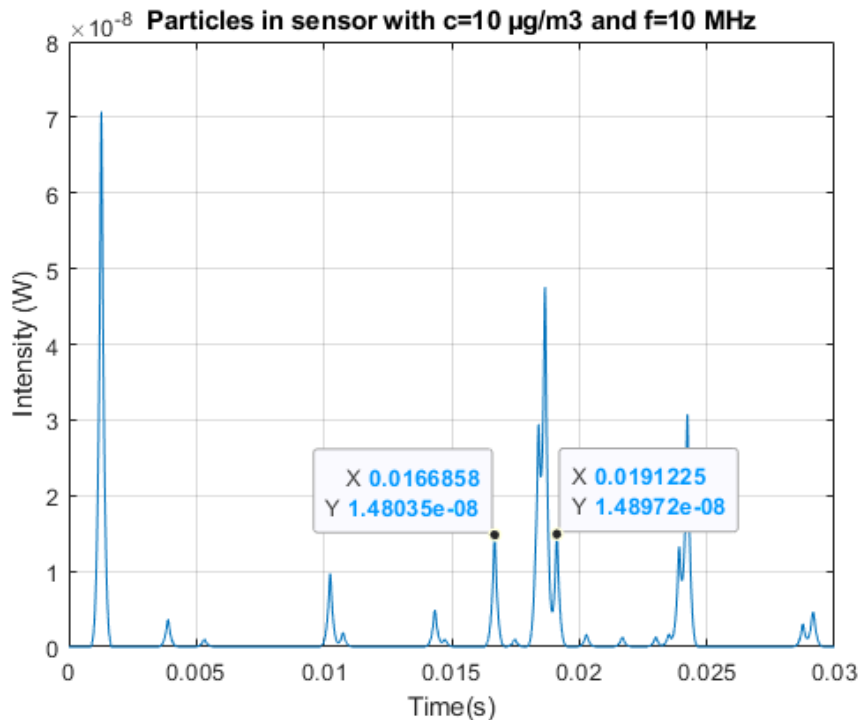
Figure 4.1 – The theoretical signal of intensity as a function of time produced by random sized particles passing through a laser beam with λ = 663 nm and sampling frequency of 10 MHz. Detection angle is 75° to 85°.

One can see that peaks of different intensities are observed for different particle sizes. The intensity levels are in the nW range or lower. In the SGPS project the intensity levels for a bulk of particles is measured to be hundreds of pW. In real time, signal might be disturbed due to noise or other contributing factors, possibly changing the intensity. Because we assume perfectly spherical particles and no loss of signal on the photodetector, the theoretical signal is produced under perfect conditions. When looking at Fig. 4.1, an overlap of intensities can be noticed around 0.018

s and 0.024 s. Multiple particles move through the laser beam and scatter light at the same time, generating the overlap between individual particles intensity signals. Because of this overlap, not all particles are distinguishable with a frequency of 10 MHz. An example of this is the situation in which there are 3 particles present in the laser beam at 0.018 s. In this situation, there are 3 particles in the laser, only two peaks can be distinguished. A possible solution to this would be increasing the sampling frequency. We zoom in on the large peak at a sampling frequency of 40 MHz in Fig. B.1. Even for a higher sampling frequency, no differentiation between particles can be done, because these particles are too close to each other and therefore have too much overlap. Due to computational memory limits, the range of GHz was not simulated.
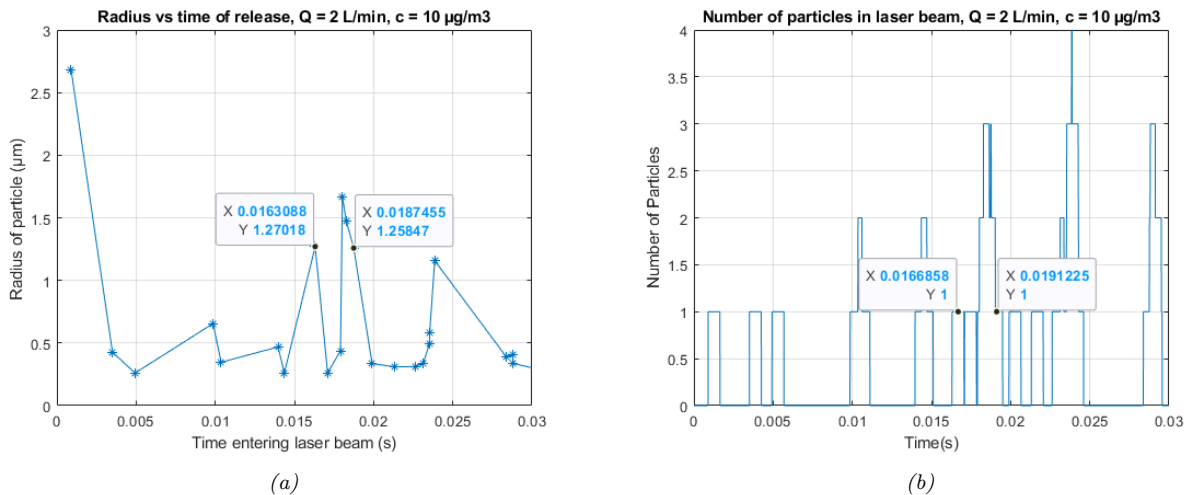
Figure 4.2 – a) R plotted as a function of time and in b) the number of particles in the laser beam as function of time both corresponding with Fig. 4.1.

After verifying which peak corresponds with what particle radius, a few things could be noted. In Fig. 4.2a the particle radius R is plotted as function of the time of entering the laser beam. The particle entering the laser at $t=0.0163$ s and $t=0.0187$ s are both around 1.25 μm. In the figure, the right peak is larger in intensity, whereas the particle size is twelve nanometers smaller($1.270\,18$ μm compared to $1.258\,47$ μm. This contradicts the hypothesis of 'larger particles scatter more light'. As the frontal surface scales with r^2, we would expect a similar scaling in the scattering intensity. In order to verify that at these data points only one particle is in the laser beam and no summation of intensities takes place, the number of particles in the viewing volume as a function of time is plotted in Fig. 4.2b. Indeed the two data points at $t=0.0167$ and $t=0.0191$ correspond with moments of time where there is only one particle in the laser beam. This contradicts our hypothesis that a larger frontal area scatters more light and a new relationship should be established.

Another option to make the particles distinguishable is making the waist smaller by focusing the beam. A negative side effect is that particles might be missed due to a smaller viewing volume, as illustrated earlier in Fig. 2.8. A solution to this would be using a convex cylindrical lens, which keeps the area of the flow similar, but the dimension of the laser beam in the direction of the flow shorter. In this case, the intensity of the light is focused on a smaller volume, creating a higher intensity to scatter for a particle. Since we are dealing with intensity ranges of nW or hundreds of pW an increase in intensity reaching the particle is beneficial. Keeping in mind the Gaussian character of the laser beam, the intensity signal decreases with a factor $\sim exp\left(-r^2/w_0^2\right)$ when a particle moves out of the center of the laser beam. So if w_0 becomes smaller, the intensity at a fixed point becomes lower and peaks are more distinguishable, as seen in Fig. B.2. Whereas in figure 4.1 we use a waist of $w_0=\frac{2}{3}w$, a value of $\frac{1}{6}w$ is used in B.2. In this case the two peaks with overlap are separated. Several options for better differentiating of particles have been discussed, but we are also in nead for a better definition of the intensity as function of R.

4.1.2 Intensity determination for lasers

As stated in Sec. 2.3, there is no easy calculation for the scattering intensity in Mie scattering. In the previous section the initial hypothesis that larger particles scatter more light was proven incorrect, due to smaller particles generating more intensity on the photodetector. In order to investigate this observation, the scattering intensity of an array of particle sizes was calculated for the same laser wavelength used and detection angle. From Fig. 4.3, we can easily conclude that there is no one-to-one relation between intensity and R, since one intensity level can correspond to multiple values of R. This confirms the conclusion from the previous section: particles of higher radius do not always scatter more light. Here we assume that the particles are in the center of the laser and thus the full frontal area is used for scattering. This excludes effects of the partial scattering and Gaussian terms in intensity calculations. Here the detection angle is set at 5° to 10° with the photodetector having the same distance of 12.5 mm from the viewing volume.
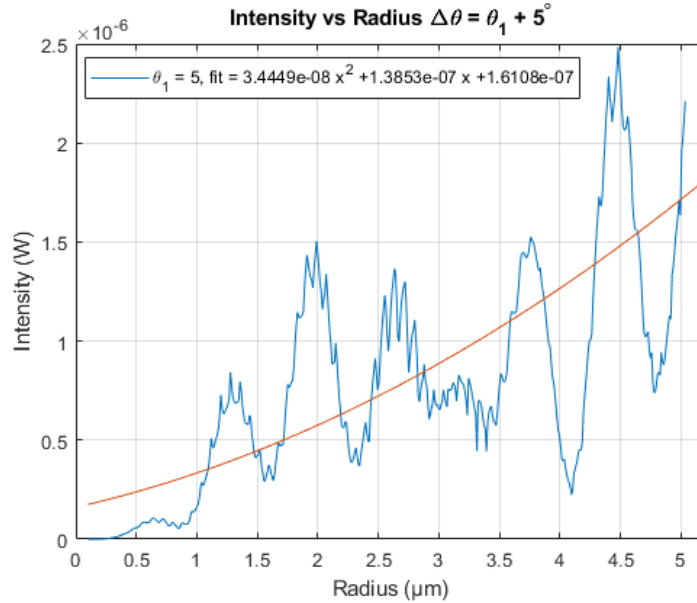
Figure 4.3 – Intensity vs particle radius measured at a detection angle 5° to 10°. λ=663 nm and m = 1.46. Illustrating the non-monotone relationship for a laser at this wavelength.

Figure 4.3, the complex relation that appears with a lot of high and low frequency oscillations. Going back to the data points in Fig. 4.1, the intensity signal decreased for a larger particle of around $1.27\,\mu m$. This decrease can be explained by the oscillating behaviour, causing a drop in intensity level after $1.25\,\mu m$. The trend of these oscillations seems to follow a quadratic relation in R, represented by the red line. The large errors in determining the particle radius can be seen at several instances, for example an intensity of $0.5 \cdot 10^{-6}$ W, which corresponds to several particle radii in the range of 1.2-$4.2\,\mu m$. Besides that the intensity becomes six times as large for a particle with radius changing from $4\,\mu m$ to $4.5\,\mu m$. It is possible to predict particle size till approximately $0.5\,\mu m$ for this case, since the relationship is one-to-one until this point. The detection angle of 5 to 10 degrees is measures intensity in the front lobe. The intensity levels for the same particle sizes of around $1.25\,\mu m$ are 100 times higher than in Fig. 4.1, measured at an angle of 85°-90°, which is what we expect from Fig. 2.3.

Changing the detection angle from 5° to 10°, to 5° to 50° we see the oscillations decreasing in amplitude but retaining their frequency, as in Fig. 4.4. The maxima and minima for the lower frequency oscillations are at the exact same location. Since increasing the detection angle is not the way to solve our problem, we take a look at the wavelength of the laser.
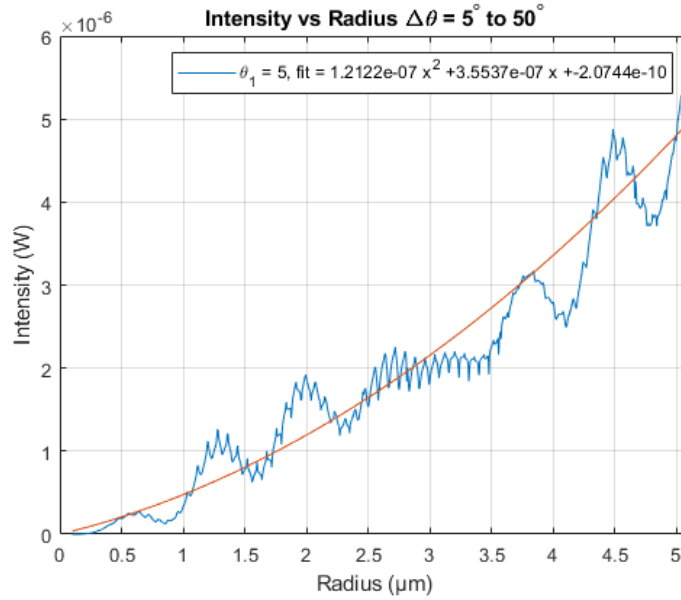
Figure 4.4 – Intensity vs. particle radius measured at a detection angle 5° till 50°. λ=663 nm and m = 1.46. Increasing the detection angle does not remove the oscillations, but the problems appear to be less in amplitude compared to Fig. 4.3.

When doing simulations at a detection angle of 5° to 10° for three different wavelengths of 300, 600 and 900 nanometer, we obtain similar graphs as shown in Fig. 4.5. For increasing λ the amplitude of the oscillations increases and the oscillations have a lower frequency. When comparing 300 and 900 nm, respectively R=0.9 µm and R=2.7 µm correspond to the second large oscillation for both wavelengths. The λ dependence can be explained by the use of the size parameter x in the Mie scattering equations, which has a $1/\lambda$ dependence. This also means that the range increases in which we can use the front lobe for particle sizing. For 900 nm one can determine its size till almost 0.9 µm, whereas for 300 nm this is three times as small at 0.29 µm. We have seen that for a laser beam oscillations appear and that increasing the detection angle or changing the wavelength of the light used, does not result in a one-to-one relationship between R and I. In order to eliminate these oscillations, a better understanding of where these oscillations are coming from is required.
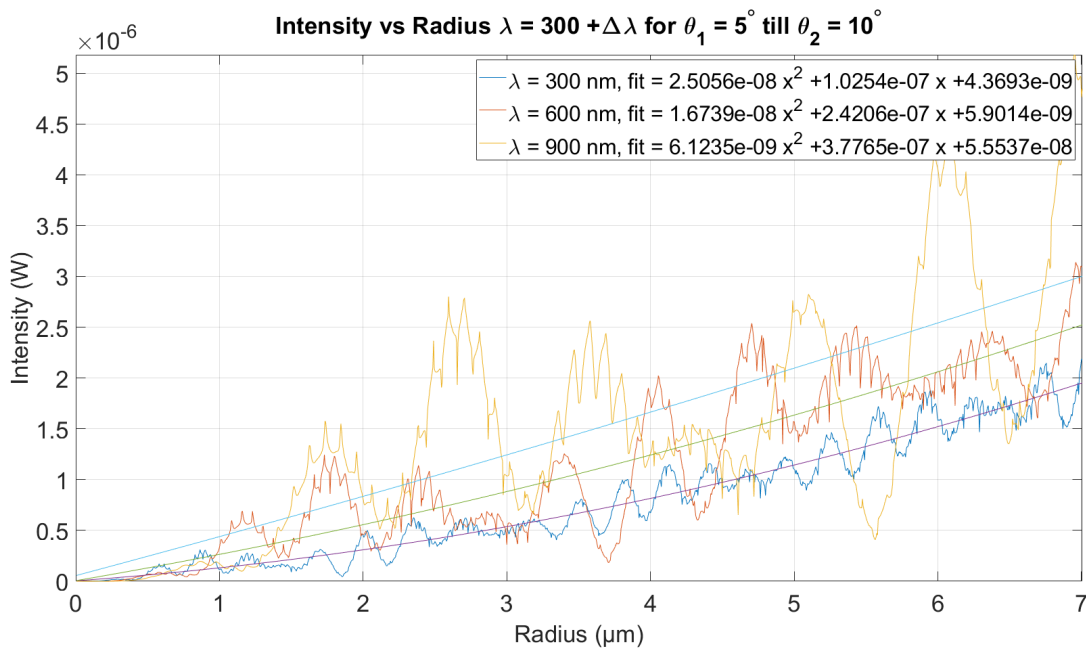
Figure 4.5 – Intensity vs. particle radius measured at a detection angle 5° till 10° for three different λ. The wavelengths used are λ=300, 600 and 900 nm respectively and m = 1.46. Increasing λ creates a similar graph, but with a phase offset and larger amplitudes.

4.1.3 Angular scattering pattern

In order to explain the origin of these oscillations, we need to take a closer look at the positioning of the lobes. The angular distribution of intensity is dependent on many factors including the particle size. When measuring at a constant angle, independently of the range of the detection angle, the shape of lobes is different for particular particle sizes. This means that maxima and minima are relocated when the particle size increases. This relocating of lobes causes intensity levels to oscillate when measuring at a constant angle. The same phenomena of relocating lobes happens for different angles, wavelengths and refractive indices. In Fig. 4.5, we illustrated this for different wavelengths. Simulations of various angles and refractive indices are shown in Fig. 4.6 and B.3.
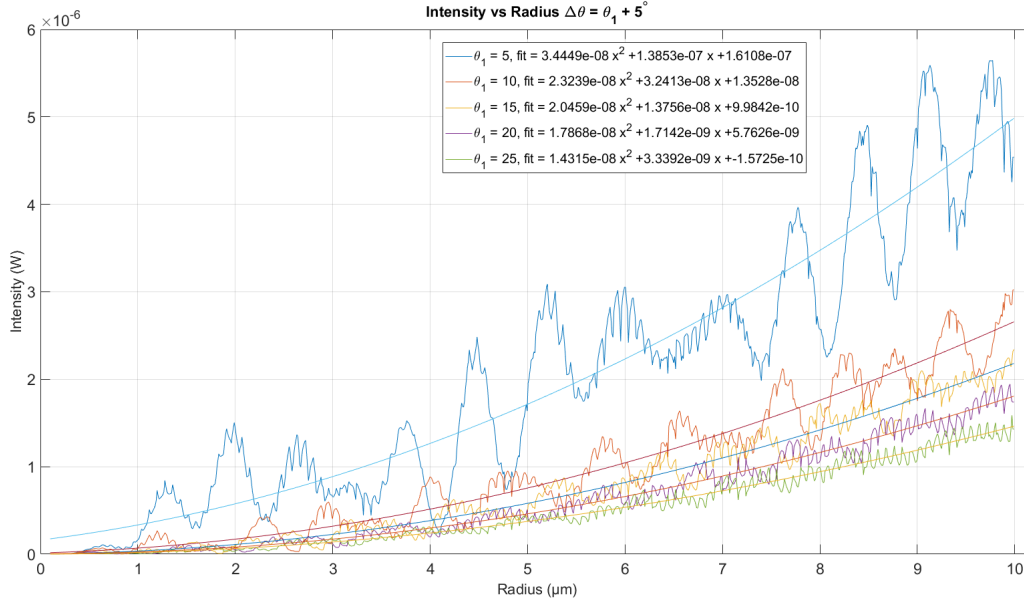
Figure 4.6 – Intensity vs Radius for different θ and a constant Δθ=5°. Different relationships with oscillations are observed with the intensity becoming lower for increasing θ at constant λ=663 nm.

When comparing the graphs for different θ, as the angle increases, in general both the intensity and the oscillations become smaller in amplitude, as seen in Fig. 4.6. The first graph at an angle of 5° to 10° measures a large portion of the front lobe. The front lobe contains the highest scattering intensity, if minima and maxima relocate in and out of the photodetector detection angle, the absolute difference in intensity is a significant amount. This in turn generates the large oscillations in intensity as function of λ and θ. When the angle increases, these differences between maxima and minima become more constant. This relatively low scattering intensity are the low side lobes. The dependency on the refractive index m can be seen in Fig. B.3. All together, these graphs show the intensity and its most important dependencies, raising more questions on how to obtain an easy relation for the intensity as function of R.

An important parameter that incorporates the effect of both the wavelength and the particle size is the dimensionless size parameter, which was defined in Sec. 2.1 as $x = \frac{2\pi R}{\lambda}$ and used in calculations for the Mie coefficients in Eq. 2.2. For increasing R and decreasing λ, the size parameter becomes larger and larger oscillations will appear, creating a larger difference between the intensity maxima and minima. Another analysis will be done for different wavelengths and the corresponding angular distribution of lobes. The QR-codes in Fig. 4.7 link to videos illustrating the dependence of the angular scattering pattern and evolution as function of R, λ and the size parameter x incorporating both of these parameters.

(a) Radius   (b) Size parameter   (c) Wavelength

Figure 4.7 – QR-codes linking to a video about the development of the angular scattering pattern as function of a parameter for a laser beam with λ=663 nm.

Fig. 4.8 shows the scattering pattern on a logarithmic scale with the scattering amplitude as the radial parameter. The red angle indicates the detection angle of 5° to 10° for the photodetector. The right plot is an extension of the plot we saw in Fig. 4.3 with the red circle belonging to the polar plot on the left. Snapshots of the first two videos for a particle with radius of 3 µm are given in Fig. 4.8 and 4.9. Since the size parameter figure would resemble the radius dependence it is left out as a snapshot.
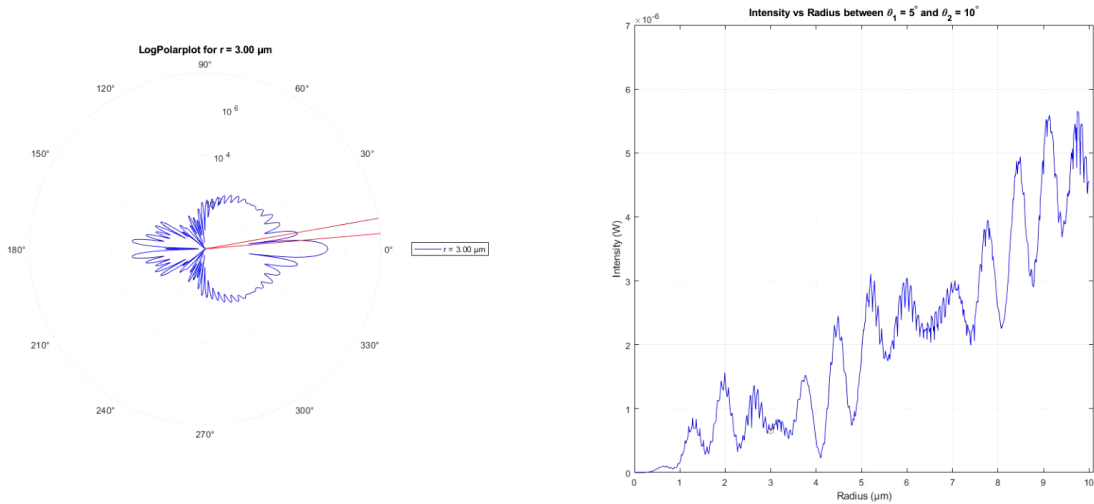
Figure 4.8 – Snapshot of the video with a 3 µm particle in which the angular scattering pattern is depicted.
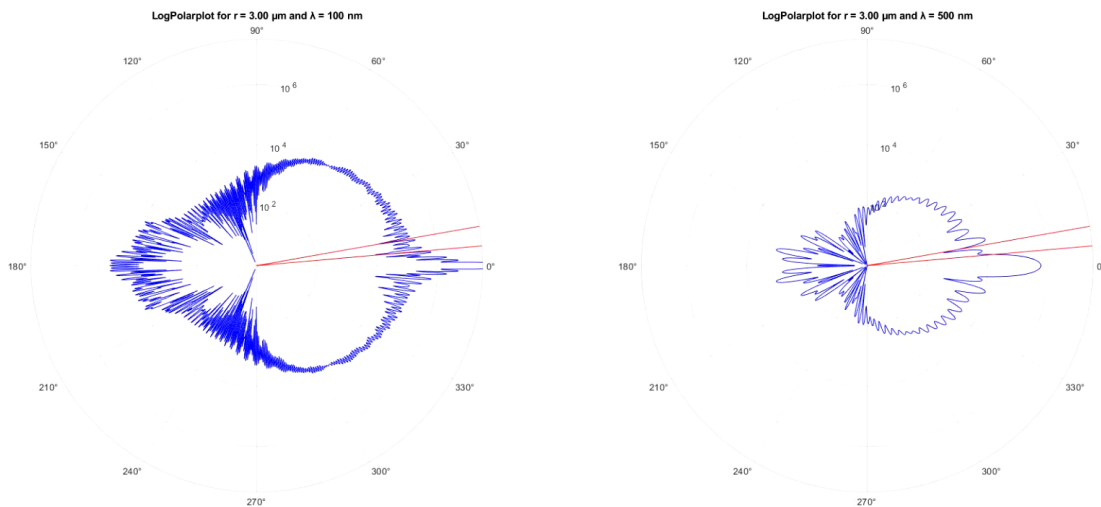
Figure 4.9 – Snapshot of the video with a 3 µm particle in which the angular scattering pattern for two different wavelengths is depicted.

For the video with the angular scattering pattern as function of the radius, until a radius of 0.3 µm there is only one front lobe and no backwards scattering. The intensity reaching the photodetector is only increasing, confirming our previous conclusion about size prediction till around 0.5 µm. Since at this particle size we are just past the Rayleigh regime (<0.1 µm), depending on the wavelength we can see in Fig. 2.1 the scattering efficiency is strictly increasing till $0.2\frac{r}{\lambda}$. As the pattern develops, the lobes seem to arise at $120°$ and $240°$ and move towards the front lobe. Finally they merge into the front lobe. The front lobe becomes larger, but the intensity drops. This relocating of lobes with maxima and minima is causing the oscillating behaviour when measuring at a constant angle. Similar process happens for backscattering. Since the pattern is symmetrical, in the horizontal axis only the 0-180 degrees will be analysed. Actual dust particles are very irregular in shape, this will cause deviations in the scattered intensity angular profile as explained in Fig. 2.5. When the detection angle is specified at a larger angle (between 60 and 90 degrees for example), the behaviour of the lobes becomes more constant, which we also the result from Fig. 4.6. The amplitude differences between maxima and minima become small since most of the light is scattered towards the front, especially for larger radii.

The same analysis holds when looking at the size parameter in Fig. 4.7b. Here we have plotted intensity as function of the size parameter ranging to 200. For example, a particle with 10 µm in radius and a wavelength of 500 nm give a size parameter of around 125. From Eq. 2.1 one can see that many combinations can lead to the same size parameter. The pattern development is illustrated in the video in figure 4.7c. Here we compare wavelengths of 100 nm on the left and 500 nm on the right and their scattering amplitude patterns. From these results we can conclude that at low wavelengths the patterns develop more quickly than at large wavelengths. The unique progression of scattering patterns at different wavelength raises the question whether for a broadband light source oscillations cancel each other, creating a workable one-to-one relation between intensity and R.

4.1.4   Intensity determination for white light source

By comparing different wavelengths, it was noted that the peaks looked similar with a phase offset, as shown in Fig. 4.5. This lead to the idea of trying a broadband light source, causing the oscillations to cancel each other and thus creating a smooth relation. White light is a continuous spectrum and the individual intensity versus radius relations for all wavelengths in the visible light range (380 to 780 nm) were investigated with a stepsize of $\Delta\lambda = 1$ nm. In white light all wavelengths are equally represented in the spectrum. By doing this we obtain an approximation of graph from the whole continuous spectrum when the particle is in the middle of the laser beam and each wavelength has the same intensity.

We will now consider the intensity as function of R at different angle of detection for the cases of $5°$, $45°$ and $85°$. As seen in Fig. 4.10 a very useful relation appears for an angle of $85°$ to $90°$. With errors not going over 0.1 µm, particles could be binned more accurately according to size. Here we determine the error as the difference between maximum and minimum value in R belonging to a certain intensity value. There is also an indication at the left bottom for a minimal sizeable particle radius of around 0.2 µm, just above the Rayleigh regime. With a detection angle of $5°$-$10°$ seen in Fig. 4.12, no good relation can be established due to high error ranges in the mid section from 2.0 till 3.5 µm with errors of 0.8 µm. This is due to the large oscillations occurring during the merging of lobes into the front lobe. For the case of $45°$-$50°$ in Fig. 4.11 we have an uncertainty under 0.03 µm for most intensities, except for the range of 0.5 or 0.8 µm. Here, the uncertainty increases above 0.1 µm. Combining all of this, we can conclude that a white light source works well and establishes a workable relation between intensity and particle radius R. In literature there are a few mentions of using a white light source in combination with Mie theory or scattering, such as by Mcgrory [72] and Pinnick [73]. But in these studies they do not mention why a broadband source is used instead of a monochromatic source. Pinnick's research focuses on the calculation of pulses on a particle counter for two configurations of particle size and refractive index. Furthermore Mcgrory focuses on the refractive index and its dependence on wavelength. Actual visualisations of the intensity as function of the particle radius R are not represented in these papers.
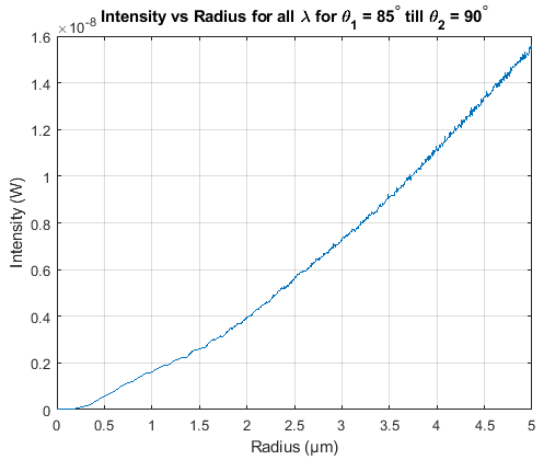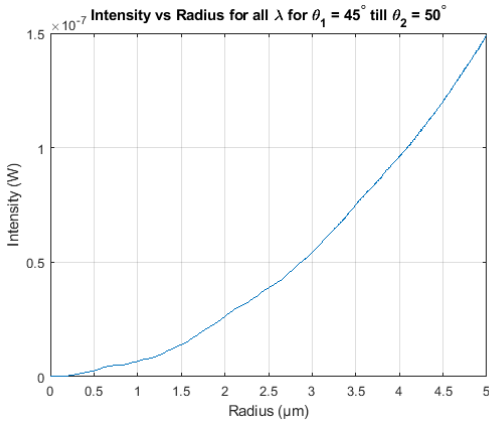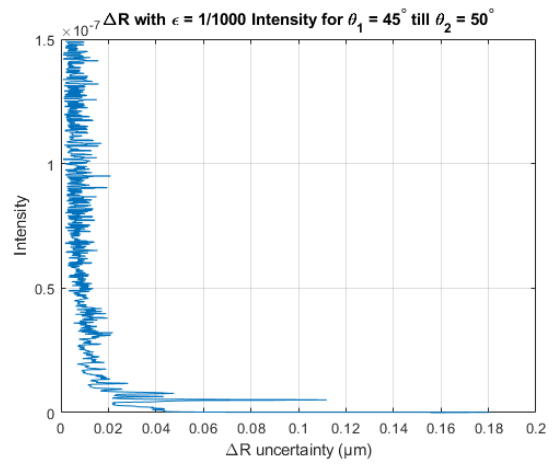
(a) Intensity white light source.
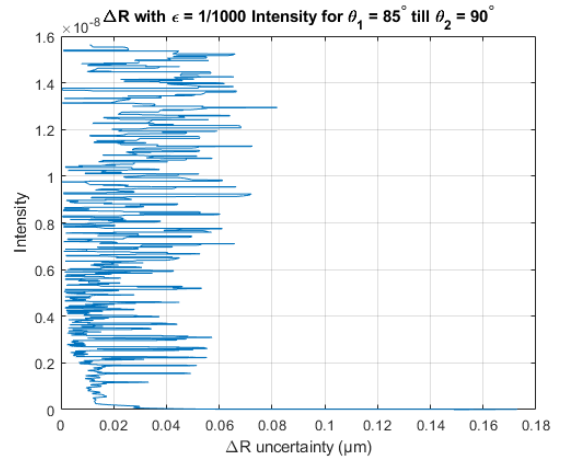
(b) Uncertainty ΔR

Figure 4.10 – Intensity versus radius relationship for a white light source at detection angle of $85°$-$90°$ and the corresponding uncertainty.
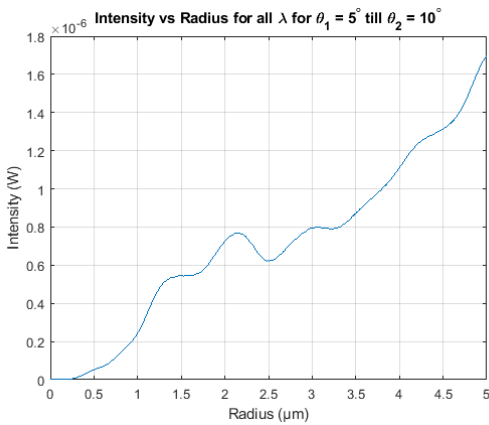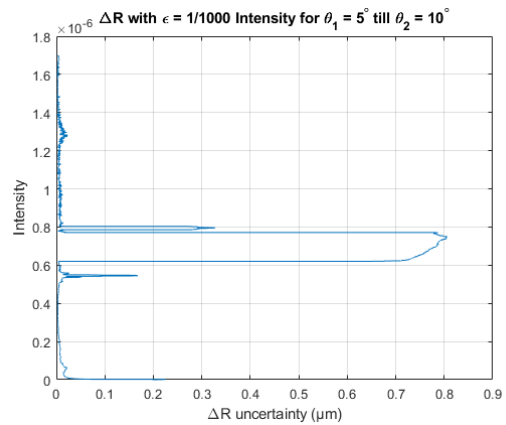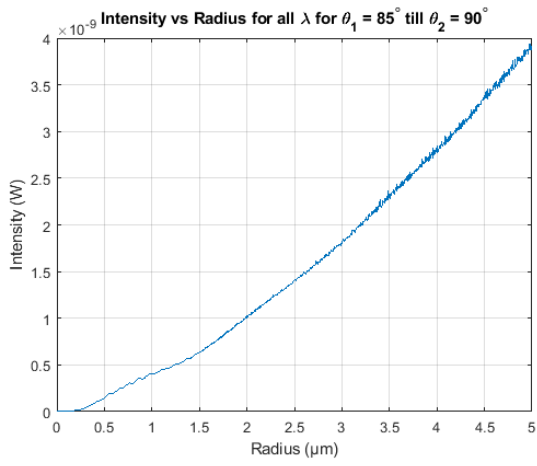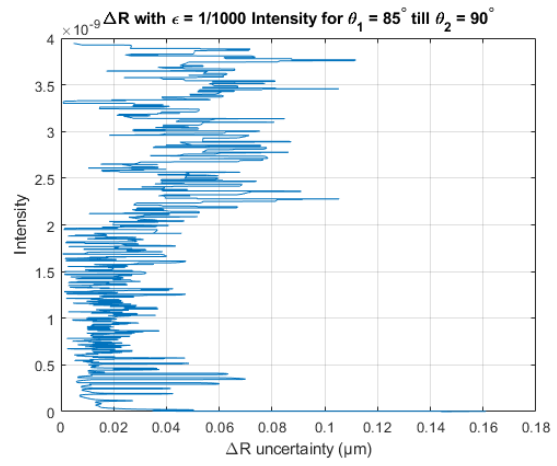

(a) Intensity white light source.

(b) Uncertainty ΔR.

Figure 4.11 – Intensity versus radius relationship for a white light source at detection angle of $45°$-$50°$ and the corresponding uncertainty.

(a) Intensity white light source.

(b) Uncertainty.

Figure 4.12 – Intensity versus radius relationship for a white light source at detection angle of $5°$-$10°$ and the corresponding uncertainty.

37

We compare a white light source with a white LED source by adding weights to the white light graphs in correspondence with the white LED spectrum in Fig. 2.9. In a white LED some wavelengths from the continuous spectrum have a higher intensity. After implementing the weights to each wavelength, we obtain Fig. 4.13, 4.14 and 4.15 for detection angles similar as in the white light simulations. Their respective uncertainty expressed as ΔR is shown besides the graphs. For the white LED in figure 4.13 we obtain a similar graph with lower intensity levels and slightly higher uncertainty for larger radii. It is noticeable that the intensity for the white LED is a factor of four lower than the constant white light source. This might come from the fact that wavelengths that scatter more at this detection angle are less represented in the LED spectrum, as in Fig. 2.9. Besides this, an angle of above 45° is recommended due to the lower uncertainty for larger angles. A trade-off needs to be made, since the intensity does drop down quite a bit for larger angles. The white light source was also simulated for an angle of 20-25 degrees, but still large errors appeared at this angle, as seen in Fig. B.4. So the lower limit is somewhere around 45° for a 5 degree detection angle. For a 5 degree detection angle and a distance to the photodetector of 12.5 mm, the photodetector would be 0.5 mm in width. Photodetectors come in all kind of sizes, therefore a larger detection angle could be used as well.

Our simulations have shown that a white light source gives a great perspective for defining a one-to-one relation between intensity and R. The white LED is a more realistic solution, after implementing the weights to the intensity for each wavelength. Another method for the sizing of particles was looked at based on the amount of lobes and the angular peak width. This can be found in appendix D.
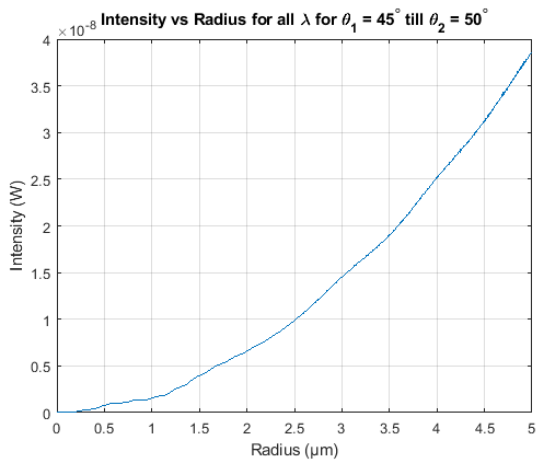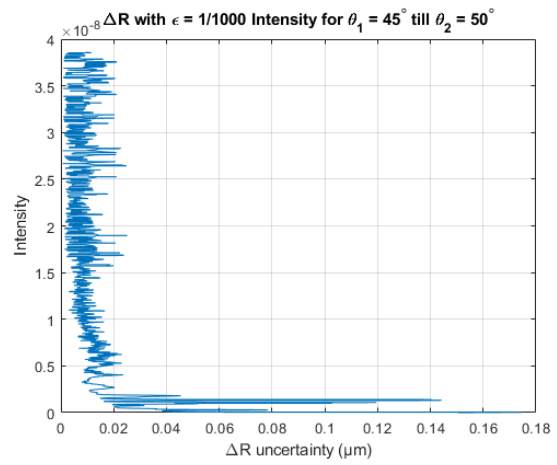
(a) Intensity white LED source.

(b) Uncertainty ΔR

Figure 4.13 – Intensity as function of ΔR for a white light or LED source at detection angle of $85°$-$90°$ and the corresponding uncertainty.
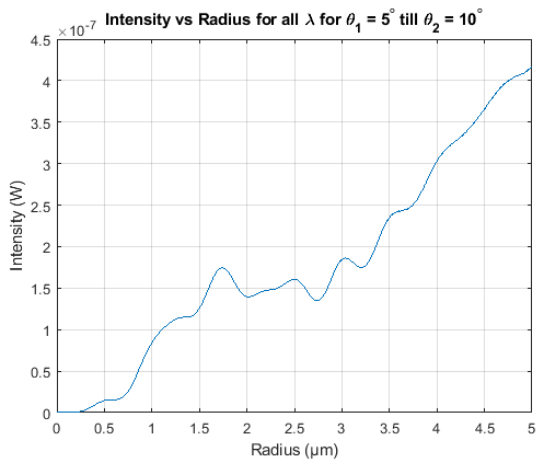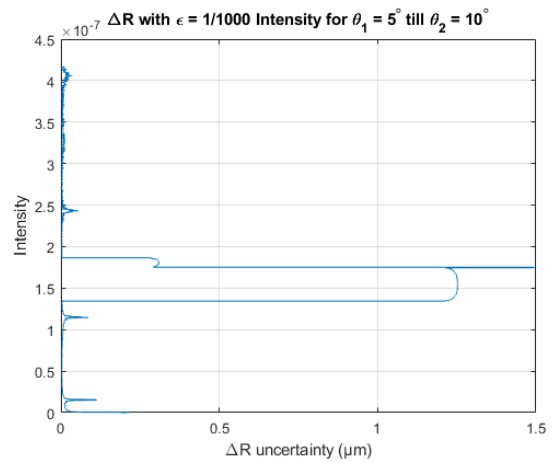

(a) Intensity white LED source.

(b) Uncertainty ΔR

Figure 4.14 – Intensity as function of ΔR for a white LED source at detection angle of $45°$-$50°$ and the corresponding uncertainty.

(a) Intensity white LED source.

(b) Uncertainty ΔR

Figure 4.15 – Intensity as function of ΔR for a white LED source at detection angle of $5°$-$10°$ and the corresponding uncertainty.

4.1.5 Summary of findings

After doing these simulations, results have shown that when using a monochromatic laser as a light source, at a 5° detection angle, it is impossible to obtain a workable one-to-one relation for intensity as function of R. This because oscillations generated a high uncertainty in sizing, with errors over 1 µm. When using a larger detection angle or a different wavelength of the laser beam the amplitude of oscillating behaviour could be limited or increased, but not removed. When switching to a white light source a proper smooth relation could be defined, in which errors did barely come above 0.1 µm for a detection angle of 5° ranging from 45°-50° and 85°-90°. This would provide a solid basis for a particle counter. Since the first had a higher intensity, the detection angle of 45°-50° is desirable at these low intensities. When using the spectrum of a white LED, the intensity dropped and for the largest detection angle the errors increased a little, which is unfavourable.

4.2 Flow simulations

The Star-CCM+ simulation results for the second part are aimed on characterization of the airflow and particle dispersion inside the cleanroom. Conclusions on whether a sensor could portray correct results will be drawn from the deposition positions, velocity probe lines and the particle residence time for different geometries.

4.2.1 Particle deposition in the cleanroom

For testing and validating the practicality of a sensor in a cleanroom environment, we will investigate the surroundings of the sensor with simulations in various geometries. Because of the uniqueness in cleanroom design, depending on the available space, placement of air vents and type of equipment that is dealt with, we limit ourselves to a segment of the cleanroom at Prodrive Technologies, but simplified to keep it translatable to other configurations. We want to characterize the flow in different geometries shown in Fig. 4.16, 4.17 and 4.18. Here, the configuration of the tables and the air columns remains the same, but two persons and equipment are added in two separate geometries. The influence of a person and equipment is investigated by using intersections of the planes and the particle trajectories as deposition location, velocity probe lines and the particle residence time. Exact dimensions of the geometries are illustrated in appendix A. Studying the variations induced on the flow field by these two elements can help to find placement options for a particle counting sensor, limit particle dispersion and validate the design of the air extraction system. Besides this, advice on lowering computation time is given for these simulations.
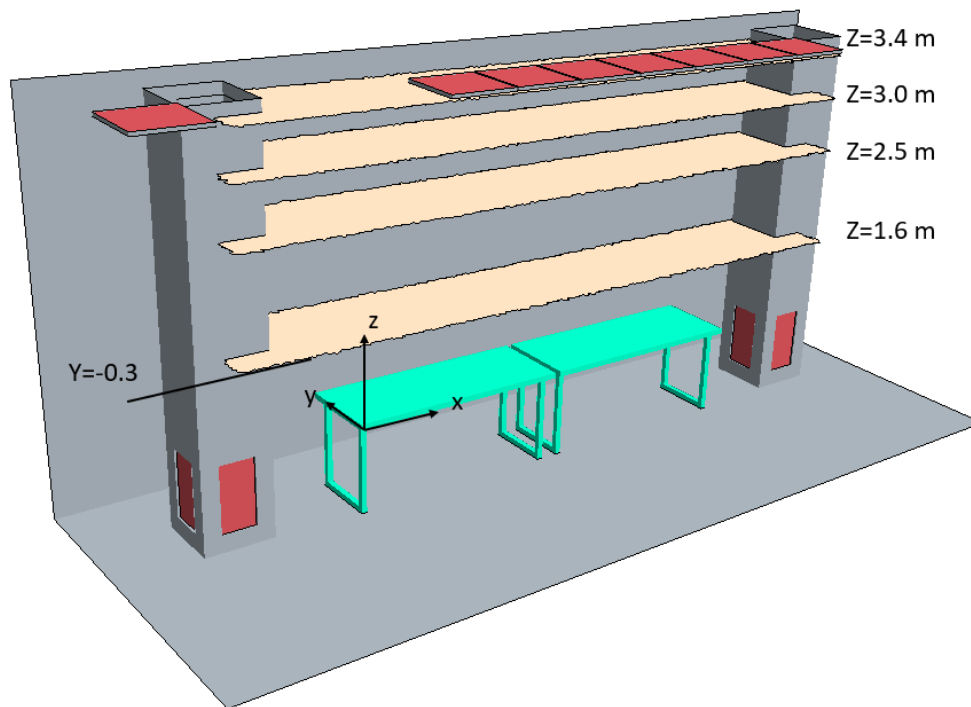

Figure 4.16 – Geometry in order to investigate the general flow path of different sized particles and different positions of release. Release planes at different z after analysis on deposition, limiting the release of particles at -0.3< y <0.7 and between the pillars.
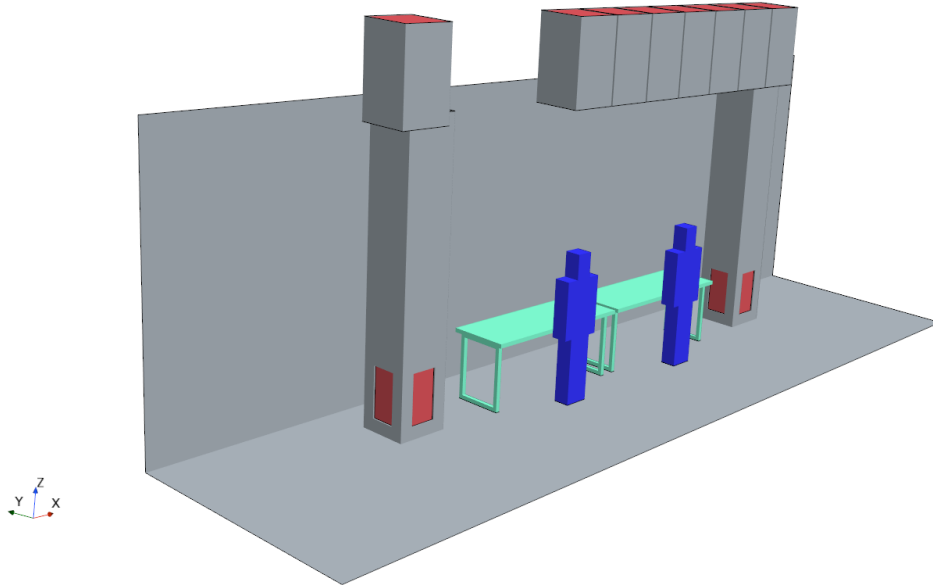
Figure 4.17 – Geometry in order to investigate the influence of two persons on the particle trajectories of different sized particles and different positions of release. The persons are standing in the middle of the table, with height 1.80 m
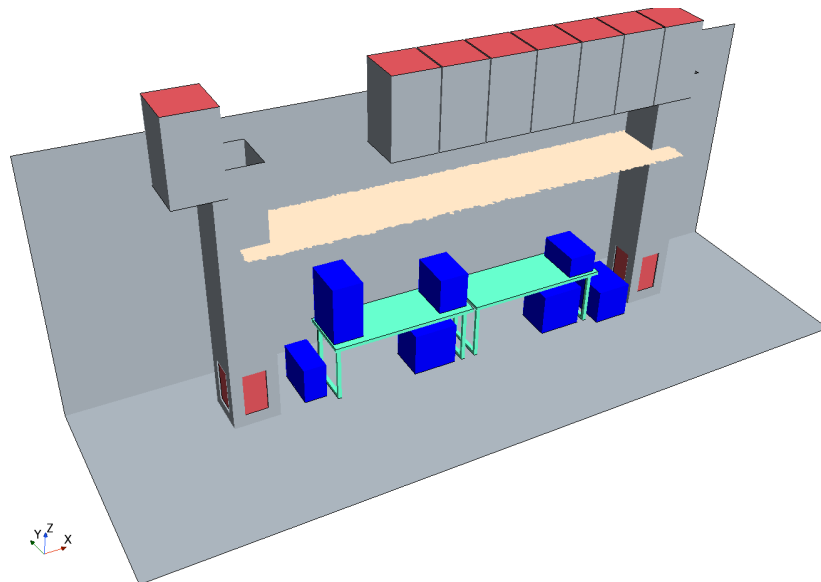

Figure 4.18 – Geometry in order to investigate the general flow path of different sized particles and different positions of release for a full geometry with equipment on and under the table illustrated as boxes and the plane used for injection of particles.

As mentioned in section 3.2.1, we simulate the trajectory of particles launched from injection points at different locations and analyse their trajectory through the clean room. With a plane at different z across the whole cleanroom, we inject up to 30 thousand particles to explore where they deposit on these horizontal planes at different z. The origin is at the edge of the left table, indicated by the Cartesian frame in Fig. 4.16. Simulations in the geometry with only the tables showed that particles, which are released at y smaller than half of the inlets ($y <$-0.3), follow the flow lines away from the tables and leave the simulation via the pressure outlet to the rest of the cleanroom, as illustrated in Fig. 4.19. Here, the streamlines from the inlets indicate the flow field nicely, clearly showing a separation between the region of interest above the table and the rest of the geometry.
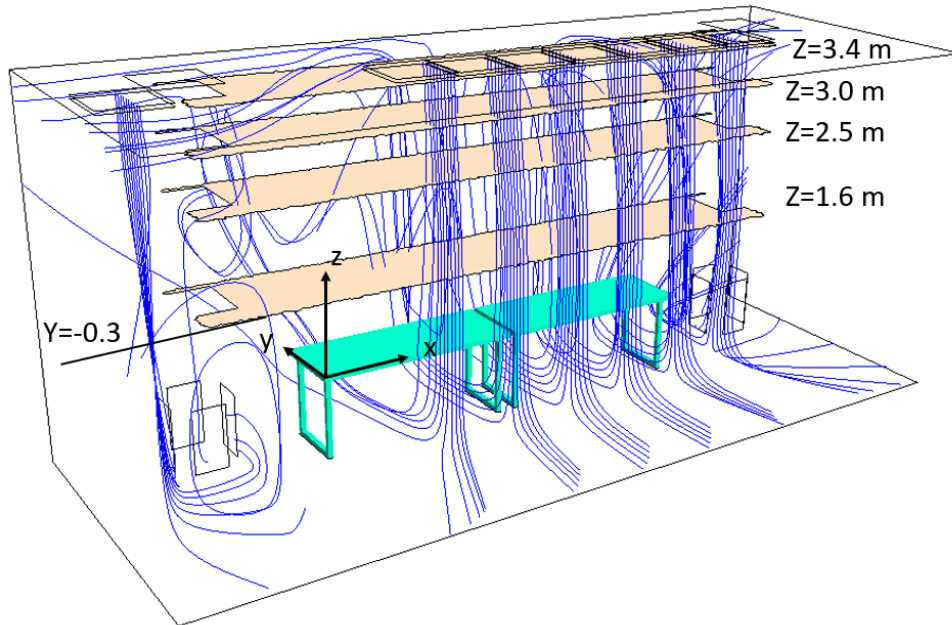
Figure 4.19 – Streamlines from the inlets indicating, when particles are released at y <-0.3 the particles move away from the table towards the rest of the cleanroom, leaving the simulation. The streamlines on the other side circulate above the table or eventually leave towards the outlets or leave between the column and the inlets.

Using this, we can optimize for computation time and limit the injection plane to our region above the table. Injecting single sized particles of 1 μm in diameter, but varying the height, we can verify where the particles deposit. This particle size is representative for the class 5 cleanroom and based on the approximations in Sec. 2.9 usable for obtaining practical data. For the injection plane we vary the height from z=1.6 m to z=3.4 m, which is just below the ceiling. Besides these, two intermediate steps at z=2.5 m and z=3.0 m are shown. The eight planes in Fig. 3.3a are indicated by the thin black lines and numbered one to eight in Fig. 4.20. With planes 6 and 7 being the actual tables indicated by the thick black lines. This configuration of planes is used in all similar figures.
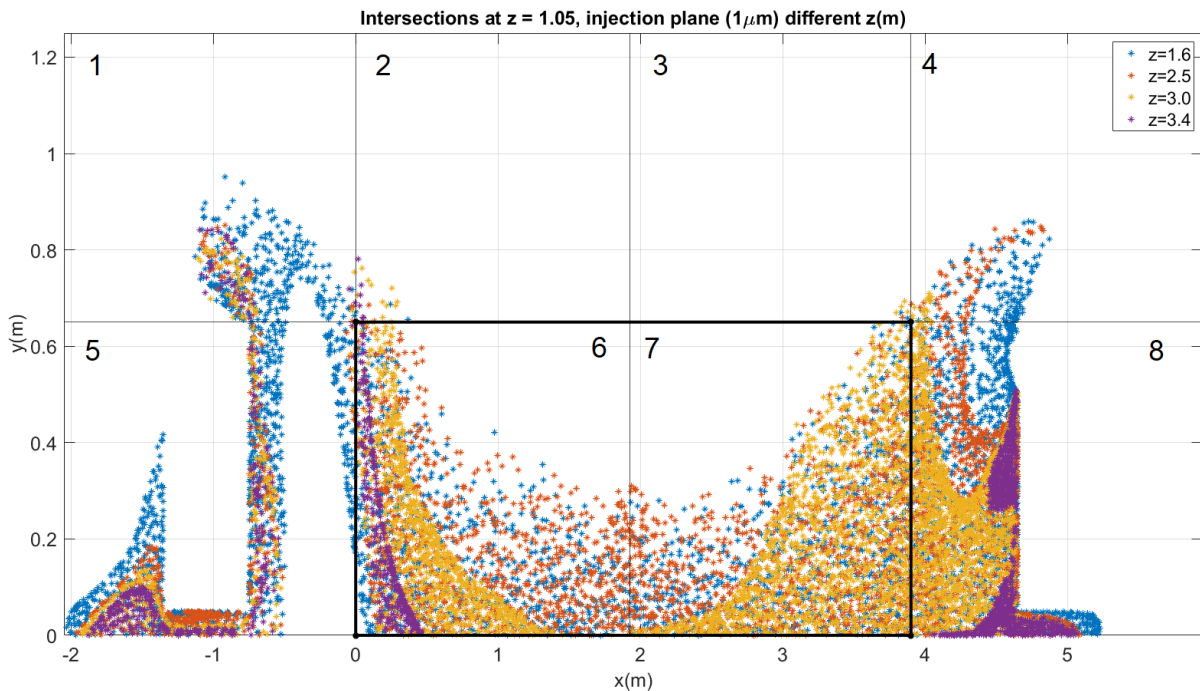

Figure 4.20 – Dispersion of 1 μm particles in the cleanroom for varying z.

As seen in Fig. 4.20, for all four cases particles deposit on the tables. When looking at the z=1.6 m case, in the middle particles drop till y=0.4 on the table. After that particles follow the flow upwards into the recirculation zone, seen in Fig. 4.21a above the table. In that figure the

43

arrows represent the direction and magnitude of the velocity field in that cell. Flow from the inlet impinges on the table and on the floor due to the inlets being slightly above the table and this impingement flow is a resemblance with the theory discussed in section 2.7 and figure 2.12. In case of the inlets being at larger distance from the table, a similar impingement flow with recirculation zone would occur, but the velocity in the middle (the circulation zone above the table) would be smaller, leaving particles circulate above the table longer. The wall of air from the inlets separating the two regions can be seen in the middle as the high velocity field indicated in red in Fig. 4.21a. The outlets can be recognised by the rectangular cut offs (pillars) of intersections in the middle of the figure or in planes 5 and 8 in Fig. 4.20.

(a) x = 0.5 above the table   (b) x = -0.25 beside the table
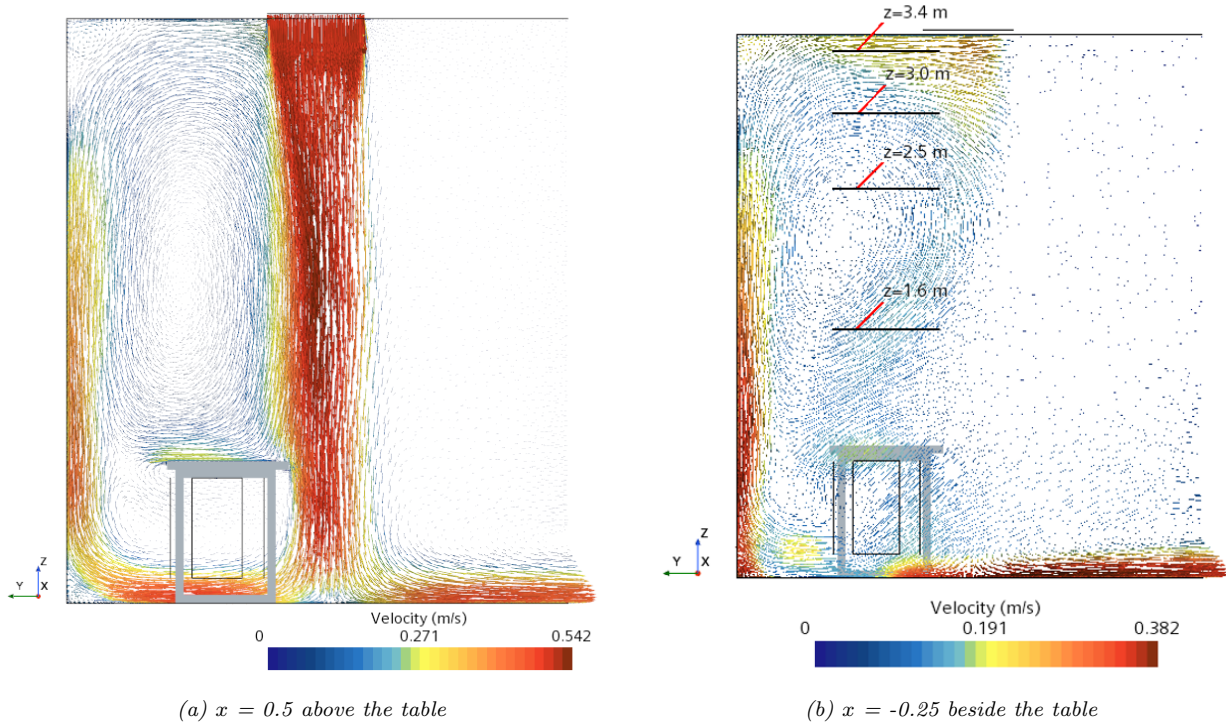
Figure 4.21 – Velocity fields in the YZ-plane for two different x positions. a) represents the recirculation zone above the table, whereas b) represents the flow field between the pillar and the table.

When particles are released from x <1 m or at x >3 m they are able to deposit on the table at y >=0.35 m. Rather than going upwards into the recirculation zone, particles follow the flow lines towards the outlets, getting drawn to the table and deposit. Intersections from height z=2.5 m agree well with the lower height of 1.6 m, but have a difference before -0.5< x <0. Here, two flows from the inlets in the ceiling merge, as seen in Fig. C.1, creating a downwards flow in the positive y direction. The velocity field causing the contamination towards the wall at y=1.25 for z=1.6 m is illustrated in Fig. 4.21b. These intersections show that when released at z >1.6, particles between the pillar and the table move into the circulation zone rather than moving down to the table or the outlets. A calculation of the deposition surface on the table as percentage of the total table surface is given in Tab. 4.1.

Table 4.1 – Particle deposition surface indicated as percentage of the whole table surface.

Geometry only Tables	
z(m)	Particle dispersion on table (% of Table)
1.6	63.6
2.5	61.0
3.0	37.7
3.4	3.9
Geometry with Equipment (minus area boxes)	
2.5	64.9
Geometry with Persons	
2.5	62.5

When z becomes larger, the particles deposit on the table closer to $y=0$ decreasing the particle deposition surface. When they are released close to the ceiling at $z=3.4$ m the particles get dragged into the flow from the inlets and mostly pushed in front of the table. So no deposition takes place for $0.5 \leq x \leq 4$, lowering the deposition surface
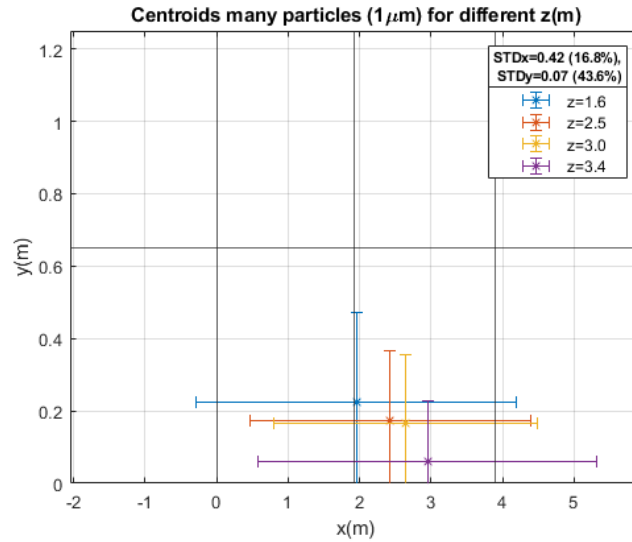

Figure 4.22 – Centroids of all particle intersections per varying height of release plane.

Looking at the centroids in Fig. 4.22 the same conclusion can be drawn. For larger z the centroid moves away from the center, to smaller y and to the right. The errorbars illustrate the large spreading in the intersections. Since $z=3.4$ m has no contamination in the middle of the tables the spreading is larger. Same yields for the standard deviation of the $z=1.6$ in the y direction. An example of the particle trajectories of $z=2.5$ m is portrayed in Fig. 4.23. Here, the beige spheres represent intersections with the plane, the squares correspond with a deleted trajectory due to meeting one of the depletion criteria mentioned in Sec. 2.9. The small blue cubes on the top mean that a particle is released and deleted immediately. These squares provide a constraining of the injection plane, since the particles move away from the table and do not deposit when released behind the table. In order to get a constant and balanced dispersion in x direction we can use the height of $z=1.6$ m and $z=2.5$ m for future simulations. Besides this releasing particles only above the table is computationally less expensive. Only particles released above or close to the table at $y >-0.1$ deposit on the table and can be measured by a potential particle counting sensor. The limited area on which particles deposit on the table creates limitations in the placement of a sensor. It is difficult to obtain correct data when placing a sensor on the back of the table, because particles deposit in front of the sensor on the table or have moved up not reaching the sensor.
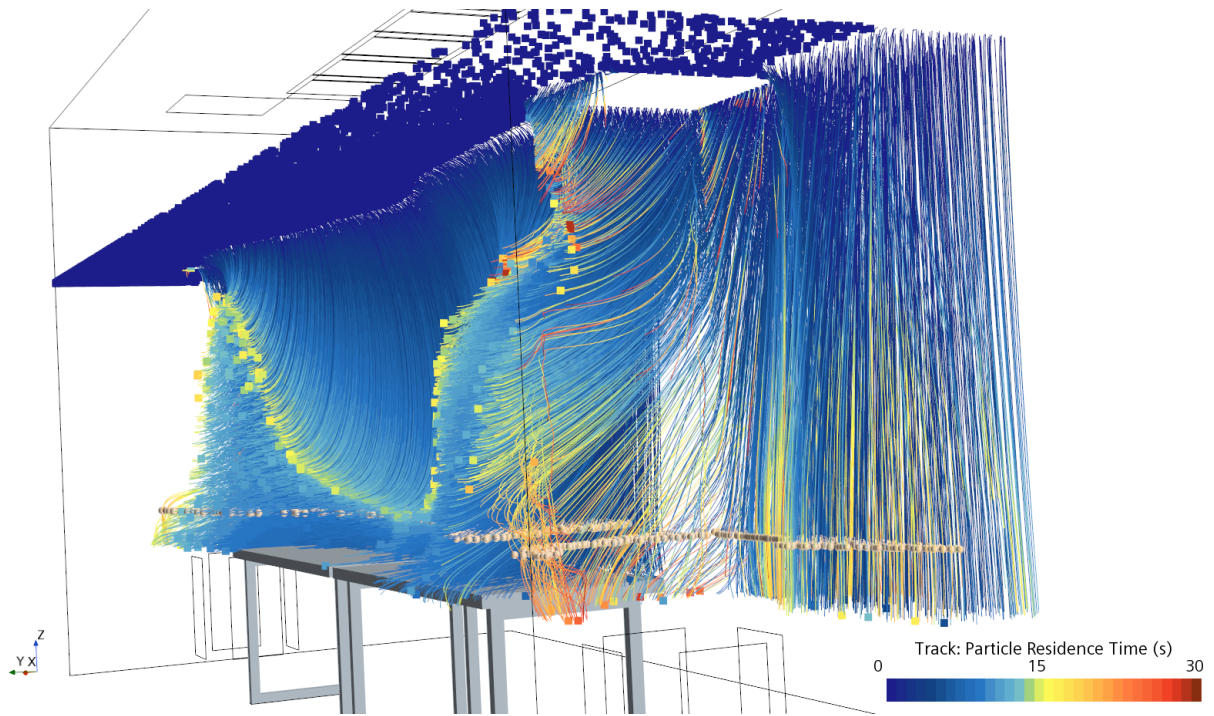
Figure 4.23 – All 1 µm particle trajectories for z=2.5 m. The beige spheres indicate intersections with the planes at 20 cm above the tables. The squares correspond to the depletion of trajectories for meeting one or more of the depletion criteria. The blue squares in the top are particles being released and immediately meeting one of the criteria, because the flow field is pointing upwards.

When instead of a injection plane a probe line is used as an injector, the particle residence time (PRT) as function of the release position can be determined by analysing the full trajectory. The result is illustrated in Fig. 4.24.
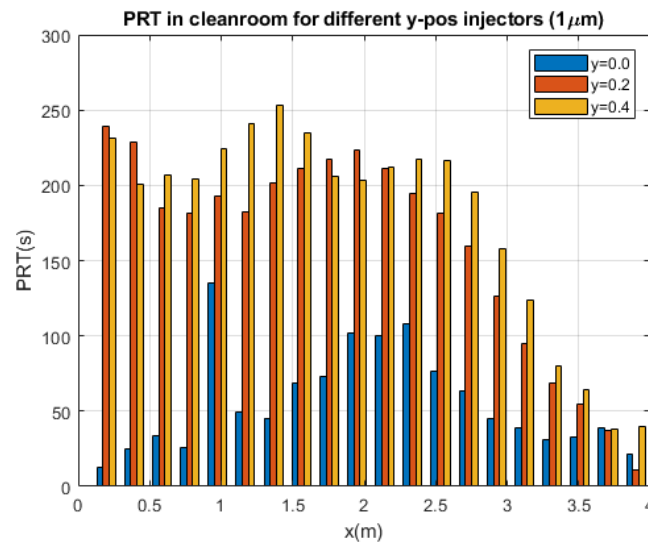

Figure 4.24 – Particle residence time for 500 injectors as function of their release position x for three different y. The bars give an average per 0.2 m. Particles released on the left side on average have a longer particle residence time for positive y.

Here we use 1 µm particles released from y positions 0.0 m, 0.2 m and 0.4 m by 500 injectors in a horizontal line above the table for x between 0 and 3.9 m. Per 20 injection points we take the mean average of the residence time. Since we have two pillars with equal positioned vents on both sides and the tables in the middle, we expect particles released from the middle having a high PRT before leaving the simulation via the outlets. When we look at particles released from $y=0$, this is the case. The histogram shows one exception at around $x=1$ m with a high PRT. Here particles move through the inlets away from the table. For the other two cases, looking at $x<2$ m the PRT decreases before moving up again. The particles for $y=0.2$ m and $y=0.4$ m are released closer to the recirculation zone and stay circulating at low velocity high above the table moving from the left

46

towards the outlet on the right, obtaining a high PRT. The reason for this could be two missing inlets in the ceiling generating the overall velocity gradient to the right. Due to lack of space in the ceiling the inlets have not been placed there. Trajectories escape the region above the table through these inlets for $y=0.2$ m and $y=0.4$ m. In Fig. 4.25, an example of $y=0.2$ m illustrates possible trajectories with the overall velocity gradient towards the right outlet and some escaping via the opening in between the inlets. When comparing $y=0.2$ m and $y=0.4$ in general $y=0.4$ m has a higher PRT, since the particles released closer to the center of the circulation zone obtain a lower velocity from the flow. The asymmetry in deposition on the table and increased PRT for larger y, questions the design of the cleanroom with the asymmetrical positioning of the inlets.

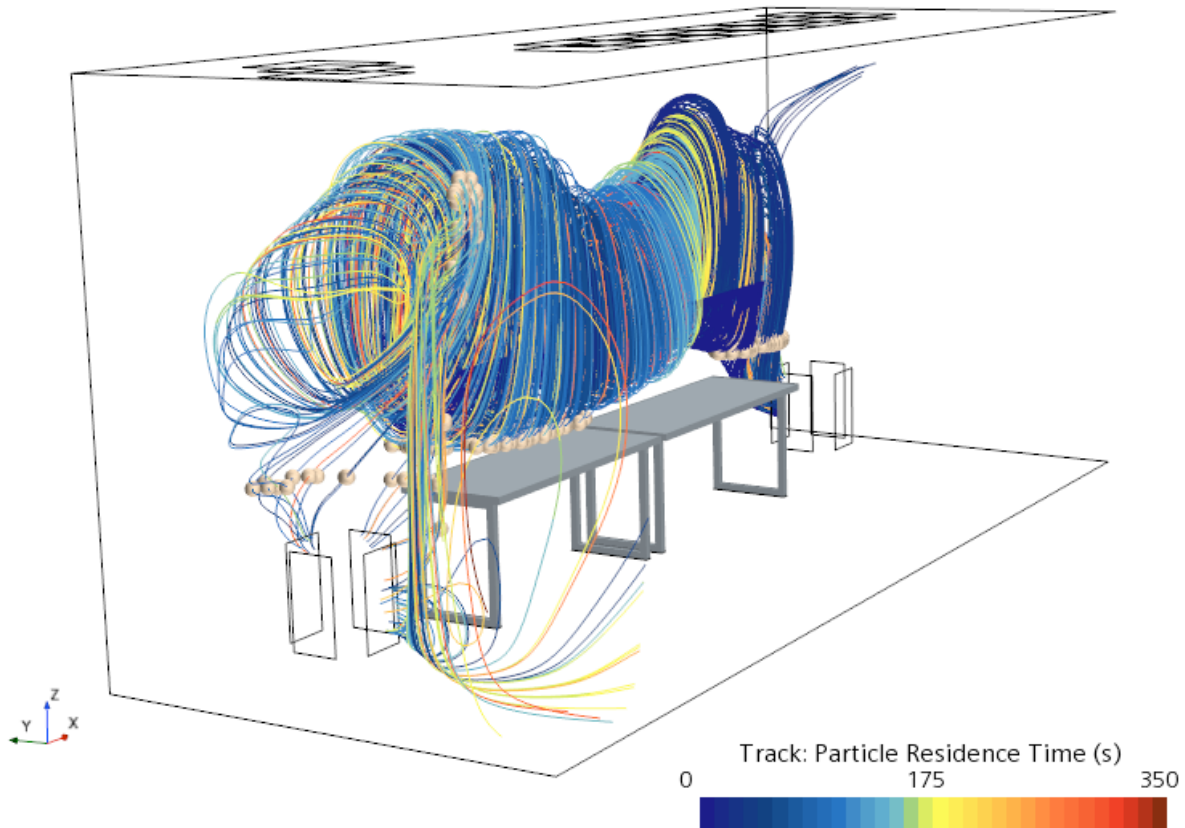*Figure 4.25 – Example of trajectories from a 500 injector line probe at y=0.2 with the colours indicating the particle residence time. Illustrating the main movement of particles from the left side towards the right outlet. Besides this particles escape the region above the table through the opening between the inlets.*

Another phenomenon considered is the opening of a door, thus generating a large breeze of air into the cleanroom. In literature it was experimentally verified by Bhattacharya that opening a door could increase particle contamination in the cleanroom [74]. Our simulations have used a release plane on the side of the cleanroom with a velocity of 1 m/s in the negative x direction. As seen in Fig. 4.26, particles are not able to enter the risk area above the table. Due to the velocity field pointed outwards behind the table, particles either return to the rest of the cleanroom or leave via the air vents. This is of course beneficial when handling a product on the table. Even when velocities were increased to 5 m/s no particles went through. When released from the other side of the geometry, similar behaviour was found.
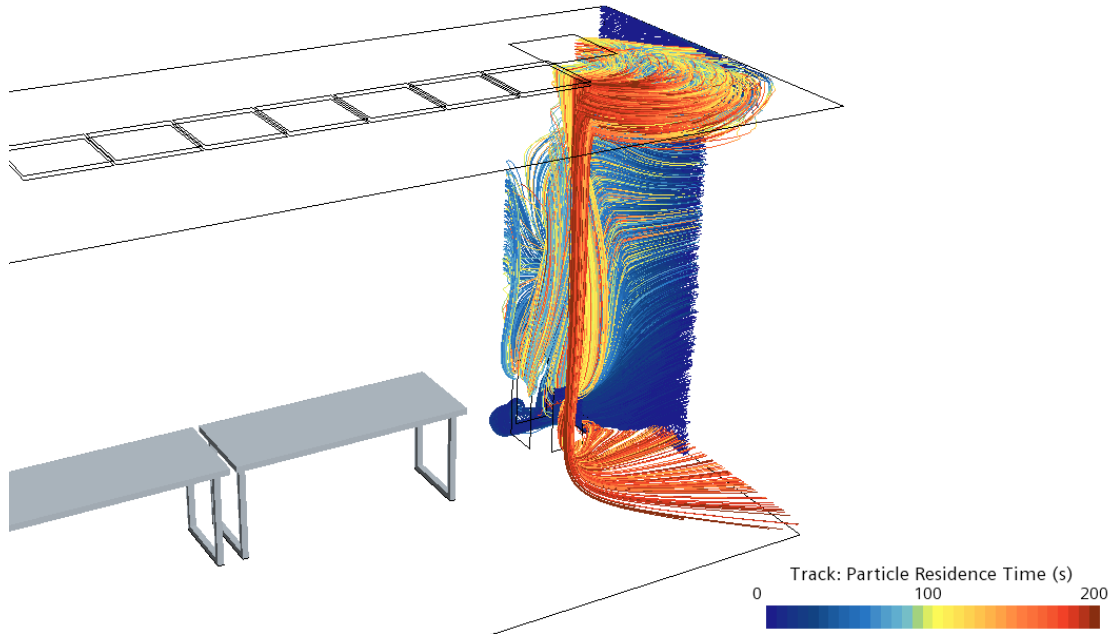
Figure 4.26 – Injection of particles from the side of the cleanroom, mimicking a large breeze due to a door in the cleanroom. Due to the velocity field pointed outwards behind the table, particles are pushed back and not able to enter the risk area above the table. Particles either return to the rest of the cleanroom or leave via the outlets.

4.2.2 Particle deposition for different particle radii

When trying to investigate how different the particle dispersion is for varying diameters in the class 5 cleanroom, it was found that the deposition changes were negligible within the range of 0.1 to 5 µm in terms of deposition area on the table. The amount of intersection on the table changes slightly as seen in Tab. 4.2. Here we have the amount of intersections on the table per category of particles for two ranges. For particles larger than $d>1$ µm a differences of approximately 3.5% was found with $d<5$ µm. The increase in intersections comes from the fact that heavier particles drop to the table faster due to gravity and lighter particles move behind the table. Although both distributions are considered uniform, not an equal number of particles per category was automatically selected for the range of 0.1-50 µm, as seen in Fig. 4.27b. This also explains the lower amount of intersections for $d<10$ µm.

Table 4.2 – The number of particles depositing on the table per diameter range. Though there is an increase in deposition when comparing $d<20$ µm and $d<30$ µm or when comparing $d<40$ µm with $d<50$ µm, which have an equal number of particles involved.

	Particles deposited on table (0.1-5 µm)		Particles deposited on table (0.1-50 µm)
$d<1$ µm	6026	$d<10$ µm	3417
$d<2$ µm	6583	$d<20$ µm	7471
$d<3$ µm	6739	$d<30$ µm	8645
$d<4$ µm	6805	$d<40$ µm	12322
$d<5$ µm	6825	$d<50$ µm	14065

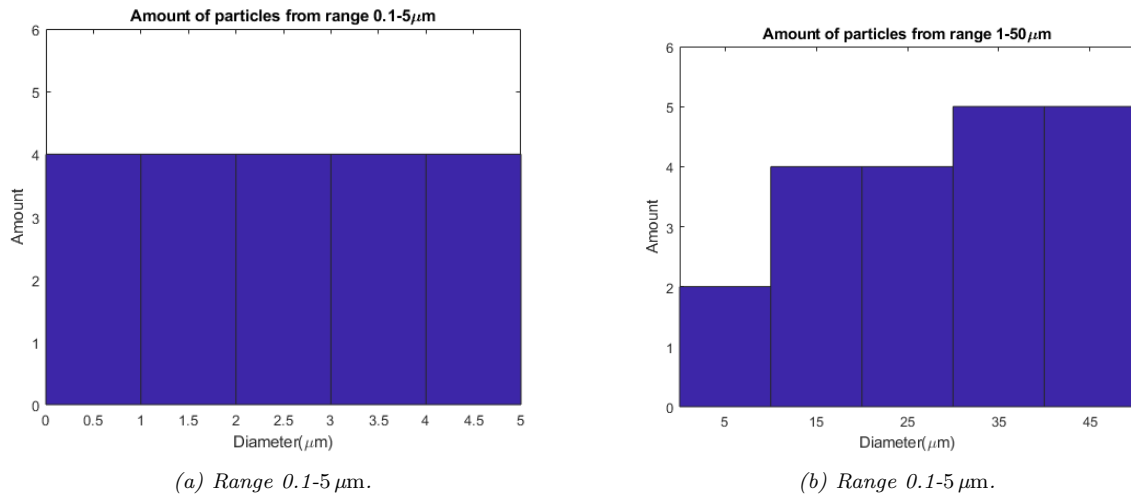(a) Range 0.1-5 μm.   (b) Range 0.1-5 μm.

Figure 4.27 – Histograms of the number of particles for two ranges of particle diameter.

When increasing the range to a uniform distribution between 1 to 50 μm and plot the intersections of particles we obtain Fig. 4.28.
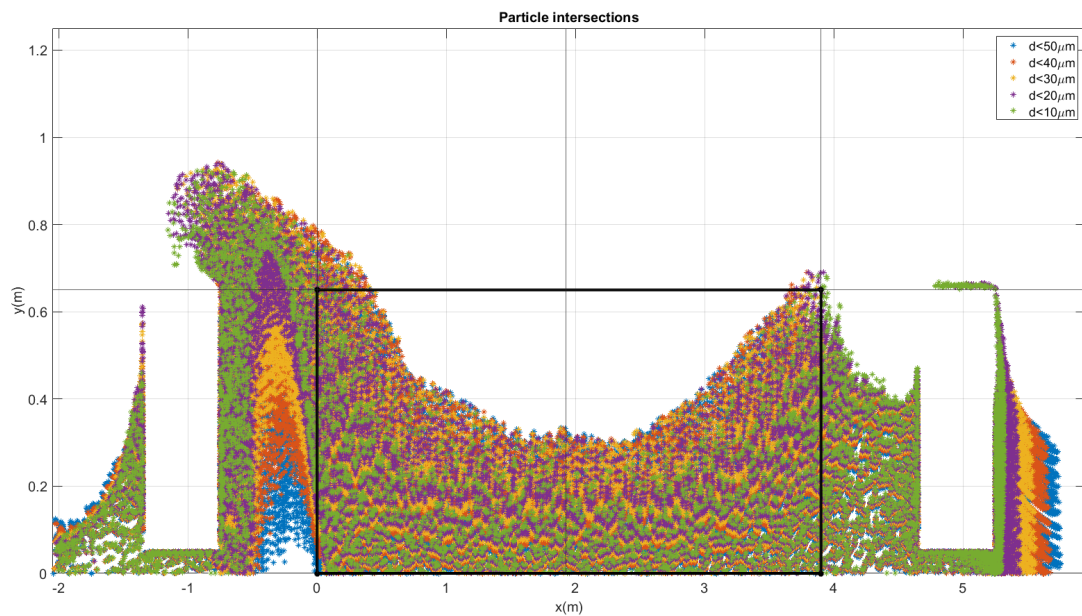

Figure 4.28 – Deposition of particles released from z=2.5 m with diameters ranging from 1 to 50 μm.

Here we selected 20 random particle sizes from the uniform distribution. These particles were divided over 5 categories, so $d<40$ μm corresponds to particles between 30 and 40 μm. From the figure we see that, even with this increased diameter distribution, the particle dispersion is very similar. Differences only appear in the same region that was discussed before in the previous section at $x<0$ with the flow passing between the pillar and the table. Here we see that heavy particles drop down faster, since gravity is becoming a dominant factor in the deposition velocity in this particle size range, as explained by Whyte [60]. Of course, the sizes of particle illustrated here are out of the scope for a class 5 cleanroom. The differences for deposition of the particles that do fall into this category did not show any remarkable or interesting additional features, only small deviations from the trajectories. From here on we continue the simulations with a constant particle size of $d=1$ μm.

4.2.3 Equipment on the desk

Equipment on desks can block the flow, causing particles to either deposit on the equipment or flow around it. In this simulation, equipment is portrayed by boxes with similar dimensions as objects in the cleanroom of Prodrive Technologies, both on and under the table. Based on our conclusions from Sec. 4.2.1, we use a release plane at height $z=2.5$ m, see Fig. 4.18 and we exclude deposition on top of the equipment.
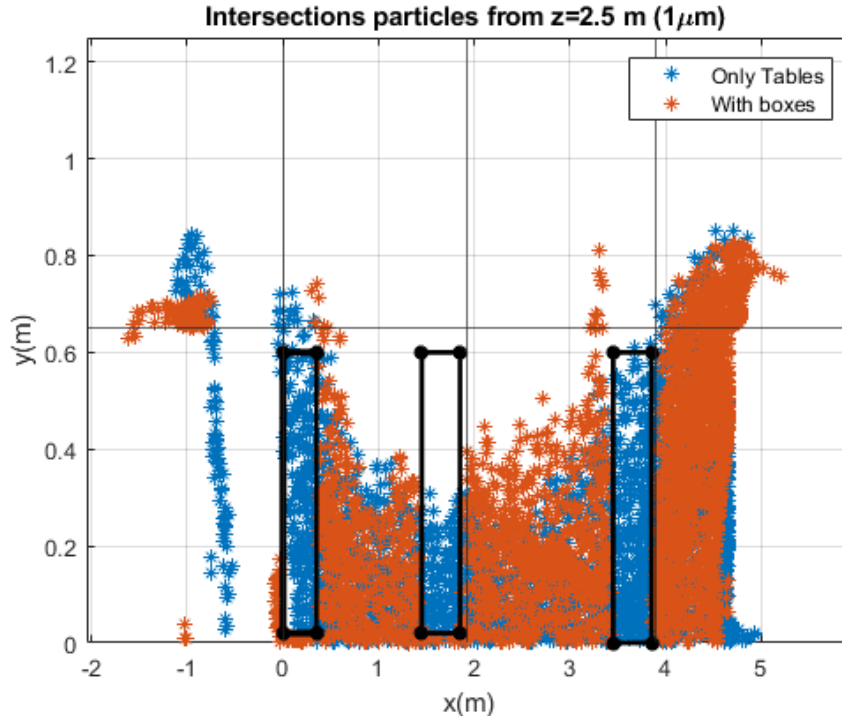

Figure 4.29 – Deposition of particles released from z=2.5 m with boxes.

From Fig. 4.29 we can see the locations of the equipment on the desks, located at around $x=0.2$ m, $x=1.8$ m and $x=3.6$ m. If we look close to the left pillar at $x=-1$ m we see a lot of intersections in the simple geometry, whereas with boxes the flow is blocked and more intersections take place at the back of the pillar due to a higher velocity at the table. The flow towards the vent closest to the table is blocked. We have set the air flow inside of each vent to be equal. This is not the case in real life, but dependent on the flow field and the blocking of air vents by equipment. For future research it might be interesting to see how the mass flow per vent changes when using equipment. Behind the boxes no deposition takes place, but on the side intersections occur a bit further back on the table. This can be seen at $x=0.6$ m and $x=3.4$ m. Fig. 4.30 shows the velocity field for two geometries. The flow moves along the boxes instead of deviating towards the outlets, creating a more laminar flow between boxes with less turbulence, see Fig. 4.31. Whereas without equipment, the flow has three patches of high TKE, one on the table and two against the wall. For with equipment, flows from underneath and above the table merge, leading to high turbulence areas behind the table. Preventing turbulence and fluctuations in the airflow is desirable since turbulence enhances particle dispersion, causing particles to not follow the flow field.
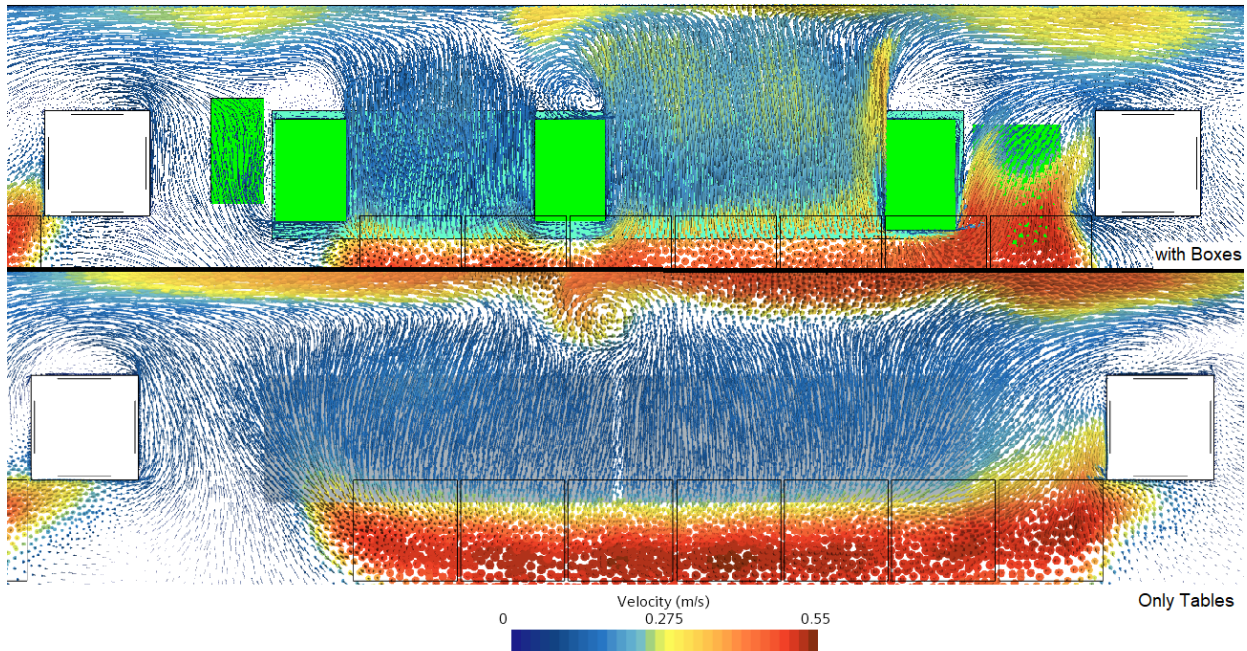
Figure 4.30 – Velocity fields at z=1.05 m for the geometries of 'with Boxes' (top) and 'only Tables' (bottom). The equipment is indicated in bright green. The tables indicated with light blue (top) and grey (bottom). The outlets and pillars illustrated by the white squares.
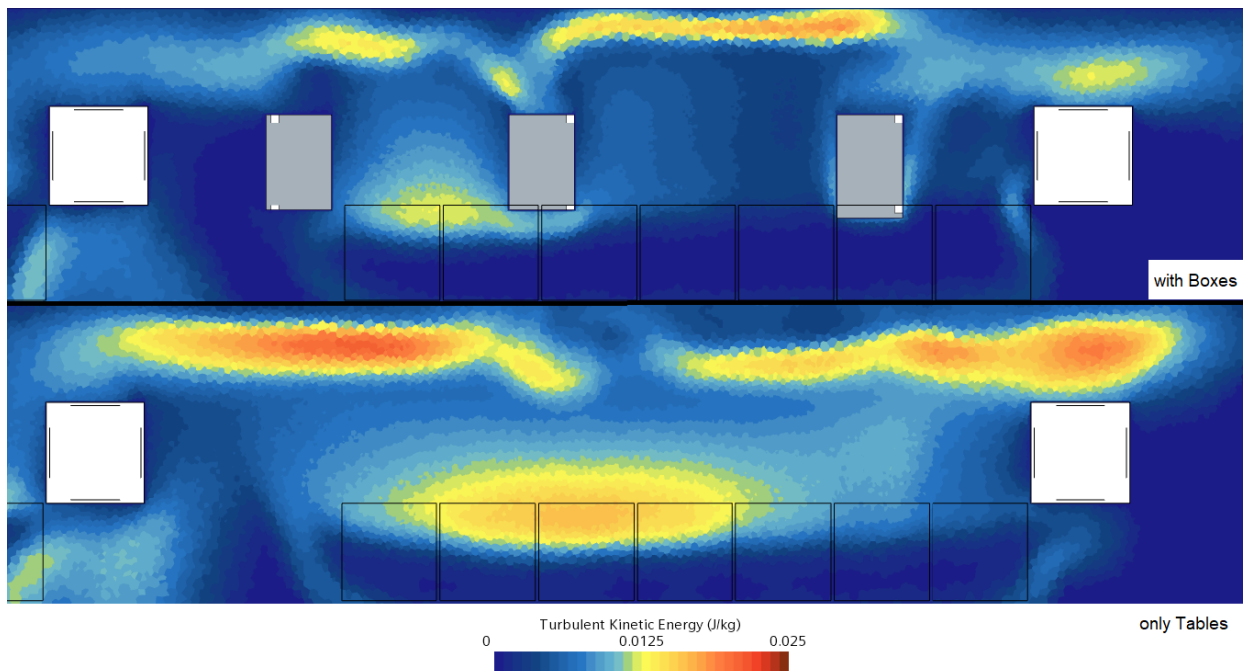

Figure 4.31 – Turbulent Kinetic Energy at z=1.05 for both cases 'with boxes' and 'only Tables'. With the equipment lowering turbulence across the table due to a more laminar flow between the equipment. Three patches of high TKE are indicated in the lower picture, whereas in the top half these patches are limited.

In general, the PRT for particles in the whole cleanroom increases when equipment is placed on the desks. The reason for this being that the particles cannot take the shortest path to teh outlets, but have to go around the equipment. When looking at Fig. 4.32a, a few things can be noted. In between the left boxes the particles move in a less turbulent and more aligned flow towards the wall. After moving past the table the particles move up against the wall before moving between the inlets towards the rest of the cleanroom, generating a large PRT at x position 1.00 m to 1.25m. This happens at a specific position at the wall. Since the geometry with boxes has a more laminar profile, instead of moving sideways, particles move straight. Therefore, particles moving up against the wall happens at lower x, as seen at x around 0.5 to 0.8 m. This causes particles to move up against the wall and leave the interesting region through the inlets, staying at high z and creating a large PRT. In between the right boxes the same thing happens, but since the particles move to

the wall in a more aligned way the velocity gradient towards the right becomes less and particles take more time circulating above the table, increasing the PRT. The difference between the two cases can be illustrated when looking at the PRT above the table in Fig. 4.32b. The values on the left side of the middle box are relatively lower compared to the right side of the box for the total PRT in the cleanroom. From this, we conclude that due to the equipment on the desk, turbulence is limited, which is desirable compared to the configuration with only tables. The deposition is highly dependent on the release position with the equipment generating two different regions in the cleanroom of Prodrive Technologies. On the left table particles move away through the inlets and on the right there is more deposition on the table. Particles released all the way from the right do barely come above the table, because they get sucked towards the vents and move right from the box. This would make it difficult to provide accurate results of the whole cleanroom with just one sensor.
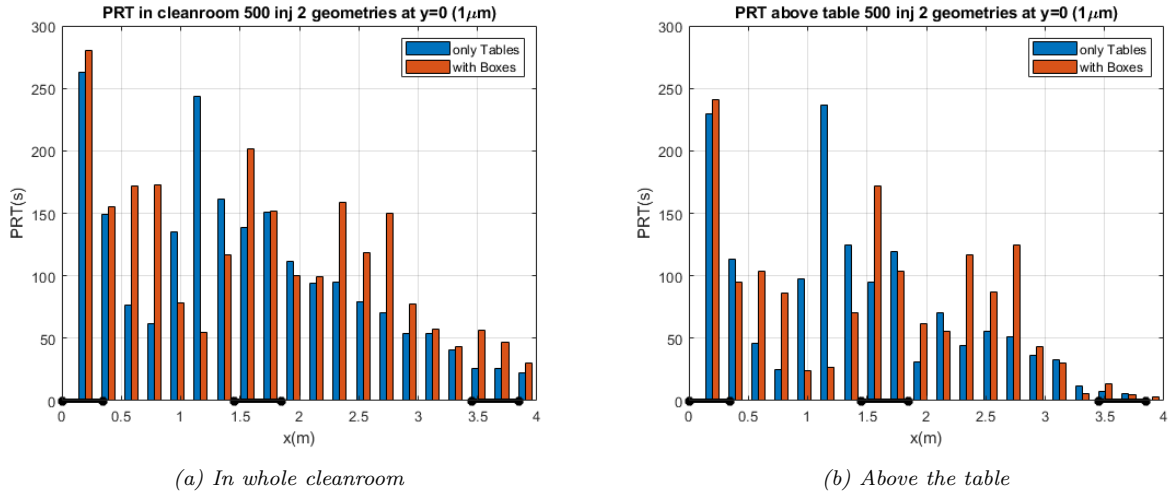

(a) In whole cleanroom

(b) Above the table

Figure 4.32 – Particle residence time in the whole cleanroom and above the table for the geometries 'only Tables' and 'with Boxes' released from $(y,z)=(0,2.5)$.

4.2.4   Particle dispersion with a person

For investigating the influence of a person on the particle dispersion we have used the geometry shown in Fig. 4.17. With the same release plane from the previous section at z=2.5 m. Since the effects of these persons take place above z=1.6 m, the height of the release plane has increased. In Fig. 4.33 it can be seen, that particles do not deposit behind and between two persons. The person is blocking the flow, lowering the velocity just behind it.
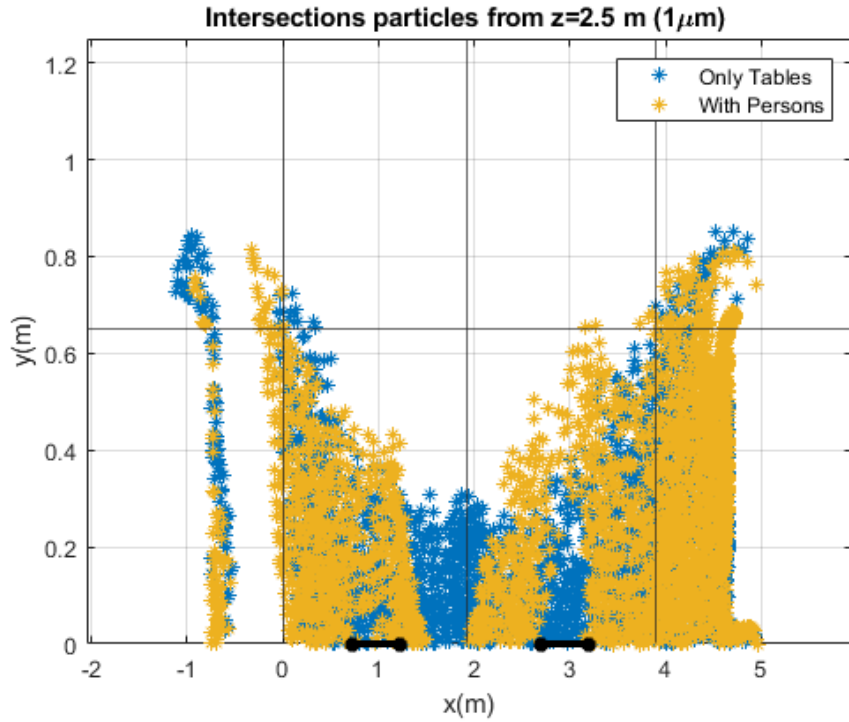
Figure 4.33 – Deposition of particles released from z=2.5 m, clearly illustrating the presence of persons. Particles do not deposit between persons or behind persons.

In order to understand why no deposition takes place in between the two persons we take a look at the velocity profiles. For the geometry without persons, the velocity profiles are smooth functions with increasing velocity close to the outlets and lower velocity in the middle. The vertical velocity components increase close to the inlets and go to zero when reaching the table at 0.85 m. Particles do deposit at larger y behind the person, which can be explained from Fig. 4.34a and Fig. 4.34b.
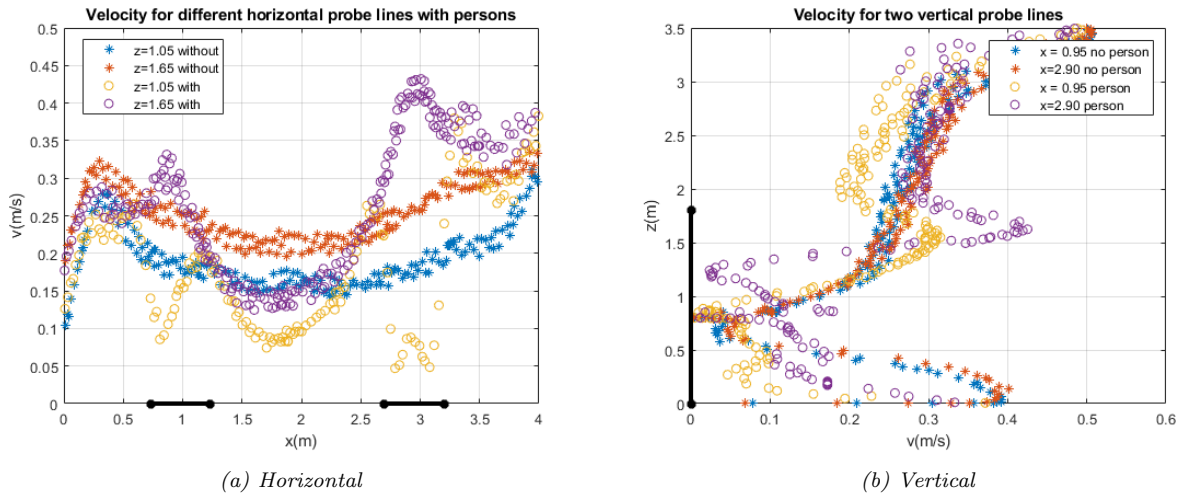

(a) Horizontal

(b) Vertical

Figure 4.34 – Horizontal and vertical velocity probe lines at $z = 1.05$ and $z = 1.65$ illustrating the drop in velocity behind a person at z=1.05, but an increase at z=1.65. With the black line indicating the positioning of the persons.

The velocity in front and above the head of a person working on the desk increases compared to the simple situation. This corresponds with the purple graph in fig. 4.34a. The same phenomena can be seen in Fig. 4.34b for the graphs with a person at z=1.65 m. The particles entering the flow here will get a higher velocity and deposit further on the table. This is further illustrated in Fig. 4.35b.

Behind a person at lower z, the velocity lowers due to the blocking of the flow in both plots. When the flow passes on top of a person, the flow moves to the sides, colliding into the rest of the flow from the inlets. The merging of these flows lowers the velocity between the persons. This

effect can also be seen in Fig. 4.35a. This lowering is not symmetrical in the middle. When looking at Fig. 4.33, there is more deposition close to the right person. This probably has to do with the asymmetrical number of inlets. Because there are more inlets on right side of the cleanroom. This causes the right table to receive more volume and higher velocity. This can also be seen from the horizontal and vertical probe lines for the simple case with only tables. The velocities differ for the left and right side. In real life, people sit down next to the desk or move around in the cleanroom. In the case of sitting down, the same effects would probably occur at lower height and Fig. 4.34b. From this we conclude that a person working closely to the desk increases the area over which particles can deposit, when the particles are released above the person. So in the case of a cleanroom where people are working on and off the desk, no constant particle dispersion is observed. This creates difficulties on placing the sensor on the desk, since there is no constant airflow.
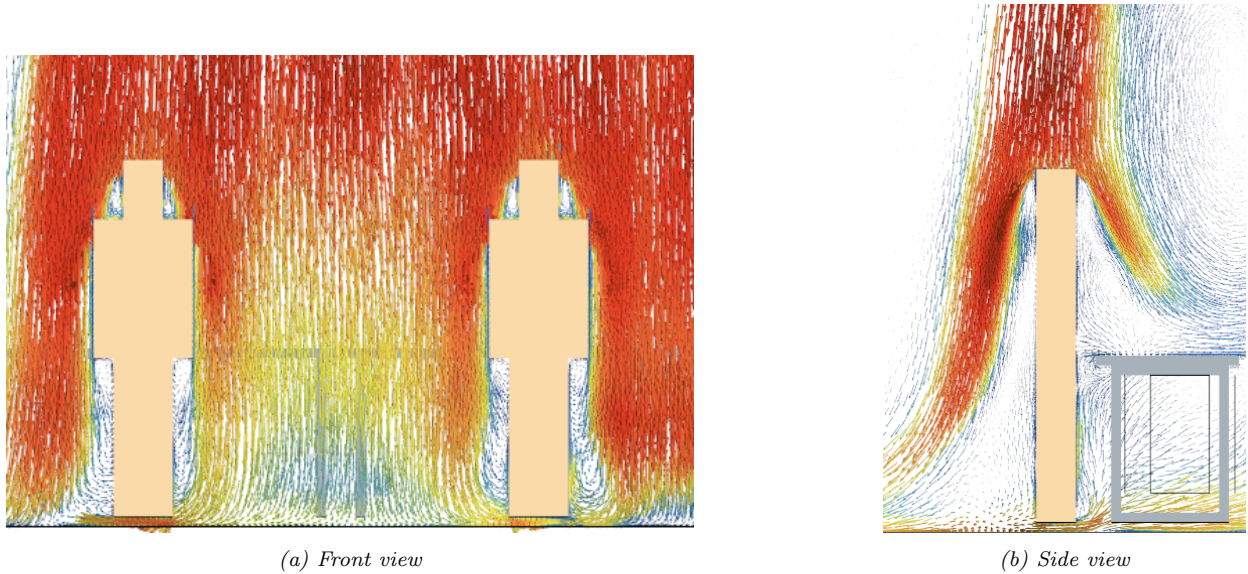

(a) Front view

(b) Side view

Figure 4.35 – Front and side view from the flow of the inlets with two persons, illustrating the deviation from the flow due to the person. In the middle the velocity lowers due to merging of the flows, whereas in the side view the velocity increases away from a persons head.

4.2.5 Summary findings flow simulations

From these investigations we can conclude that a limited injection plane with single size particles is the best option for performing simulations. In case the particles are not above the table, they are deleted immediately and the differences between trajectories of varying size particles is negligible. Furthermore, the deposition of particles changes slightly for different configurations. When equipment is placed on the desk, a more laminar flow with higher velocity develops on the table. The limitation of turbulence is beneficial in limiting particle dispersion. When personnel is working close to the table, particles deposit a bit further on the table, because of flow deviating from a persons head with more horizontal velocity in the y direction. In the middle, two velocity fields merge with each other lowering the velocity of the flow field.

By using a 'wall' of air from the inlets, the region of interest is separated from the rest of the cleanroom, making it difficult for particles from the outside to deposit on the table. Particles released within this region have a deposition surface about 60% of the table surface, but there is a high risk of recirculation. This recirculation had a negative impact creating long particle residence times, especially released at $y > 0$ from the left side. This might be due to the asymmetry in the placement of the inlets.

5   Conclusion & Outlook

Combining all these results has led to critical insights on particle counting and possible usage of particle sensors inside a cleanroom, with the focus on a small part of Prodrive Technologies' cleanroom. The right technical specifications, combined with proper placement in the cleanroom is crucial for obtaining accurate results on the particle size distribution. Both parts of this thesis have contributed to this. While investigating a one-to-one relation between intensity and the particle radius R, it was found that a white light source is the best option for obtaining a smooth relation with low sizing error and a relatively high intensity obtained by the photodetector. The resolution was below $0.1\,\mu$m for a detection angle of 5 degrees at an angle between 85°-90°, resulting in a usable resolution for classifying particles in bin sizes defined by a class 5 cleanroom. From the intensity figures we derive that the white LED is a less effective source, since certain wavelengths that appear to scatter a lot of intensity are damped due to the wavelength spectrum. A white LED source is more practical to work with.

For future work, investigating the exact optimal angle for the photodetector and the corresponding detection angle is important to gain insight in the relationships between intensity on the photodetector and particle size resolution. Furthermore, it would be interesting to see how the size of the viewing volume can be optimized depending on the concentration of particles. Besides, knowing where particles pass through the viewing volume is of importance, because the intensity a particle receives is dependent on the position when entering the light source.

When looking at the flow around a particle counting sensor, several aspects need to be taken into account, such as the velocity fields, sensor placement and turbulence. For the simple clean room geometry with only the tables, it was concluded that positioning a single sensor on a desk creates difficulties in portraying accurate results on the more general distribution of the whole cleanroom. The area of particle deposition is limited to the sides and the front of the table when particles are released below a height of 2.5 m and only to the sides of the table for particles coming from close to the ceiling. Due to the flow from the inlets and the recirculation zone we could define a smaller area important for particle deposition. This causes troubles, since flow from the inlets separates the region above the table with the rest of the cleanroom, it would give false results to characterize particle concentration or a size distribution outside of this region with a sensor placed on the desk. Also the asymmetry that appeared due to the positioning of the inlets in the ceiling and a possible employee working on the desk, could make the placement of the sensor a crucial element.

The asymmetry in positioning of the inlets generates a velocity gradient to the right (above the center of the table) and particles escaping between the inlets instead of moving towards the outlets. Although no inlets could be placed in the ceiling due to space shortage. For further research it would be interesting to see how the reorganization of inlets would change the particle deposition for placement of a sensor. Different configurations can be thought of, such as alternately placed inlets or more inlets. Also changing the location of the outlets in the pillars to in the floor or the wall behind the table might influence the deposition onto the table. This is turn would result in an optimized cleanroom with a good air extraction system. When using the geometry with equipment, the deposition of particles shifted to the center of the table since the sides were blocked by equipment. The resulting flow with less turbulence caused a distinction between the flow on the left and right table. In this case, multiple sensors would be needed to characterize the particle deposition on the table. Where particles from the left table moved through the inlets outside of the region above the table, on the right table particles recirculated above the table many times before moving towards the outlets.

Altogether, obtaining real time data with a single sensor on the desk will not provide conclusive results. Using multiple sensors on each edge of the table over a longer period of time gives better insights on the size distribution and contamination around the table. Since the geometry presented is separated from the rest of the cleanroom by a blockade of air from the inlets, sensors at different

locations in such a segment would provide the necessary information about contamination across the cleanroom in general, improving the air quality.

6   Acknowledgements

I would like to thank a few people that guided me during the project. First of all, Veridiano Moreno Marques from Prodrive Technologies for helping me during the project with his critical questioning and fresh insights in tackling problems on a weekly basis. Secondly, Herman Clercx from the University of Technology Eindhoven for giving me advice and feedback on the fluid flow theory and its implementation in modeling. Besides these I would like to thank Niels Smith from Prodrive Technologies for helping me define the research questions and planning to successfully finish this graduation project. At last, I would like to thank all colleagues from Prodrive Technologies that helped or provided feedback during my master thesis.

Bibliography

[1] James W Useller. *Clean room technology*, volume 5074. Technology Utilization Division, National Aeronautics and Space Administration, 1969.

[2] S Vidali. Human contamination control in a clean room. *Microchemical journal*, 45(3):336–342, 1992.

[3] W Whyte and T Eaton. A cleanroom contamination control system. *European Journal of Parenteral and Pharmaceutical Sciences*, 7(2):55–61, 2002.

[4] Denina Hospodsky, Jing Qian, William W Nazaroff, Naomichi Yamamoto, Kyle Bibby, Hamid Rismani-Yazdi, and Jordan Peccia. Human occupancy as a source of indoor airborne bacteria. *PloS one*, 7(4):e34867, 2012.

[5] EN ISO. 14644-1,"cleanrooms and associated controlled environments". *European Standard*, 2015.

[6] Sylvie Parat, Alain Perdrix, Sylvie Mann, and Pierre Baconnier. Contribution of particle counting in assessment of exposure to airborne microorganisms. *Atmospheric Environment*, 33(6):951–959, 1999.

[7] Angels Figuerola-Tejerina, Ana Hernández-Aceituno, Guadalupe Alemán-Vega, César Orille-García, Miguel Ruiz-Álvarez, and Helena Sandoval-Insausti. Developing a faster way to identify biocontamination in the air of controlled environment rooms with hepa filters: airborne particle counting. *Scientific Reports*, 10(1):1–8, 2020.

[8] G. Mie. Beiträge zur optik trüber medien, speziell kolloidaler metallösungen. *Ann Phys*, 25:377–445, 1908.

[9] Paul G Huray. *Maxwell's equations*. John Wiley & Sons, 2011.

[10] Peter Debye. Das verhalten von lichtwellen in der nähe eines brennpunktes oder einer brennlinie. *Annalen der Physik*, 335(14):755–776, 1909.

[11] G Gouesbet. Generalized lorenz–mie theories, the third decade: a perspective. *Journal of Quantitative Spectroscopy and Radiative Transfer*, 110(14-16):1223–1238, 2009.

[12] Hendrik Christoffel Hulst and Hendrik C van de Hulst. *Light scattering by small particles*. General publishing company Ltd, 1981.

[13] Milton Kerker. *The scattering of light and other electromagnetic radiation: physical chemistry: a series of monographs*, volume 16. Academic press, 1969.

[14] Craig F Bohren and Donald R Huffman. *Absorption and scattering of light by small particles*. John Wiley & Sons, 2008.

[15] David Pariseau. Air quality instrumentation: A history. `https://particlesplus.com/air-quality-instrumentation-a-history/`. accessed: 03.10.2022.

[16] Xiaoyu Yu, Yunbo Shi, Tian Wang, and Xu Sun. Dust-concentration measurement based on mie scattering of a laser beam. *PLoS One*, 12(8):e0181575, 2017.

[17] RS Gao, AE Perring, TD Thornberry, AW Rollins, JP Schwarz, SJ Ciciora, and DW Fahey. A high-sensitivity low-cost optical particle counter design. *Aerosol Science and Technology*, 47(2):137–145, 2013.

[18] Erika Brattich, Alessandro Bracci, Alessandro Zappi, Pietro Morozzi, Silvana Di Sabatino, Federico Porcù, Francesca Di Nicola, and Laura Tositti. How to get the best from low-cost particulate matter sensors: Guidelines and practical recommendations. *Sensors*, 20(11):3073, 2020.

[19] Bin Zhao and Ping Guan. Modeling particle dispersion in personalized ventilated room. *Building and Environment*, 42(3):1099–1109, 2007.

[20] Z Zhang and Q Chen. Prediction of particle deposition onto indoor surfaces by cfd with a modified lagrangian method. *Atmospheric Environment*, 43(2):319–328, 2009.

[21] JD Posner, CR Buchanan, and D_ Dunn-Rankin. Measurement and prediction of indoor air flow in a model room. *Energy and buildings*, 35(5):515–526, 2003.

[22] Sasan Sadrizadeh, Sture Holmberg, and Ann Tammelin. A numerical investigation of vertical and horizontal laminar airflow ventilation in an operating room. *Building and Environment*, 82:517–525, 2014.

[23] Qingyan Chen. Comparison of different k-ε models for indoor air flow computations. *Numerical Heat Transfer, Part B Fundamentals*, 28(3):353–369, 1995.

[24] Olivier Rouaud and Michel Havet. Computation of the airflow in a pilot scale clean room using k-ε turbulence models. *International Journal of Refrigeration*, 25(3):351–361, 2002.

[25] Christian Wolff. Rayleigh- en mie-verstrooiing. `https://www.radartutorial.eu/01.basics/rb59.nl.html`. accessed: 02.08.2022.

[26] MATLAB. *version 9.12.0 (R2022a)*. The MathWorks Inc., Natick, Massachusetts, 2022.

[27] C. Mätzler. MATLAB functions for Mie scattering and absorption. *Sensors and Actuators B: Chemical,*, July 2002.

[28] Frank Bowman. *Introduction to Bessel functions*. Courier Corporation, 2012.

[29] B ISO et al. Particle size analysis—laser diffraction methods, 2009.

[30] Peter Görner, Xavier Simon, Denis Bémer, and Göran Lidén. Workplace aerosol mass concentration measurement using optical particle counters. *Journal of Environmental Monitoring*, 14(2):420–428, 2012.

[31] R. Nave. Blue sky. `http://hyperphysics.phy-astr.gsu.edu/hbase/atmos/blusky.html`. accessed: 03.08.2022.

[32] Steven D Kochevar. Basic guide to particle counters and particle counting. *Particle Measuring Systems, Inc.*, pages 54–54, 2006.

[33] Paul Latimer and Peter Barber. Scattering by ellipsoids of revolution a comparison of theoretical methods. *Journal of Colloid and Interface Science*, 63(2):310–316, 1978.

[34] Menachem Elimelech, John Gregory, and Xiadong Jia. *Particle deposition and aggregation: measurement, modelling and simulation*. Butterworth-Heinemann, 2013.

[35] Palas. Aerosol sensor welas® 2100. `https://www.palas.de/en/product/aerosolsensorwelas2100`. accessed: 11.08.2022.

[36] PP Vaidyanathan. Generalizations of the sampling theorem: Seven decades after nyquist. *IEEE Transactions on Circuits and Systems I: Fundamental Theory and Applications*, 48(9):1094–1109, 2001.

[37] Umer Hassan and Muhammad Sabieh Anwar. Reducing noise by repetition: introduction to signal averaging. *European Journal of Physics*, 31(3):453, 2010.

[38] Oxford Reference. monochromatic radiation. `https://www.oxfordreference.com/view/10.1093/oi/authority.20110803100206892`. accessed: 15.08.2022.

[39] Gianluca Tosini, Ian Ferguson, and Kazuo Tsubota. Effects of blue light on the circadian system and eye physiology. *Molecular vision*, 22:61, 2016.

[40] Leroy D Dickson. Characteristics of a propagating gaussian beam. *Applied Optics*, 9(8):1854–1861, 1970.

[41] Javier Alda. Laser and gaussian beam propagation and transformation. *Encyclopedia of optical engineering*, 999, 2003.

[42] Anne Marie Dixon. *Environmental monitoring for cleanrooms and controlled environments*. CRC Press, 2016.

[43] William Whyte. *Cleanroom technology: fundamentals of design, testing and operation*. John Wiley & Sons, 2010.

[44] Stephen B Pope. *Turbulent flows*. Cambridge university press, 2000.

[45] Amèni Mokni, Hatem Mhiri, Georges Le Palec, and Philippe Bournot. Numerical study of vertical wall jets: Influence of the prandtl number. *International Journal of Aerospace and Mechanical Engineering*, 3(3):313–320, 2009.

[46] Anuj K Shukla and Anupam Dewan. Flow and thermal characteristics of jet impingement: comprehensive review. *Int. J. Heat Technol*, 35(1):153–166, 2017.

[47] Bernhard Weigand and Sebastian Spring. Multiple jet impingement- a review. In *TURBINE-09. Proceedings of International Symposium on Heat Transfer in Gas Turbine Systems*. Begel House Inc., 2009.

[48] Doug McLean. *Understanding aerodynamics: arguing from the real physics*. John Wiley & Sons, 2012.

[49] Leonhard Euler. Principes généraux du mouvement des fluides. *Mémoires de l'académie des sciences de Berlin*, pages 274–315, 1757.

[50] Peter Alan Davidson. *Turbulence: an introduction for scientists and engineers*. Oxford university press, 2015.

[51] FT Nieuwstadt, Jerry Westerweel, and Bendiks J Boersma. *Introduction to Theory and Applications of Turbulent Flows*. Springer, 2016.

[52] T-H Shih, William W Liou, Aamir Shabbir, Zhigang Yang, and Jiang Zhu. A new k-epsilon eddy viscosity model for high reynolds number turbulent flows: Model development and validation. Technical report, 1994.

[53] Mohammad S Saidi, M Rismanian, Masoud Monjezi, Mohsen Zendehbad, and S Fatehiboroujeni. Comparison between lagrangian and eulerian approaches in predicting motion of micronsized particles in laminar flows. *Atmospheric Environment*, 89:199–206, 2014.

[54] Siemens Digital Industries Software. Simcenter star-ccm+ user guide, version 2021.1. `https://support.industrysoftware.automation.siemens.com/general/documentation.shtml`. accessed: 02.11.2022.

[55] William C Hinds and Yifang Zhu. *Aerosol technology: properties, behavior, and measurement of airborne particles*. John Wiley & Sons, 1999.

[56] Bin Zhao, Ying Zhang, Xianting Li, Xudong Yang, and Dongtao Huang. Comparison of indoor aerosol particle concentration and deposition in different ventilated rooms by numerical method. *Building and Environment*, 39(1):1–8, 2004.

[57] Guy Metcalfe, Michel FM Speetjens, Daniel Robert Lester, and HJH Clercx. Beyond passive: chaotic transport in stirred fluids. *Advances in Applied Mechanics*, 45:109–188, 2012.

[58] Christopher Earls Brennen and Christopher E Brennen. Fundamentals of multiphase flow. 2005.

[59] Daniel Cromer—Lynn Pruisner. Snow, rain, and the stokes number.

[60] W Whyte, M Derks, et al. Airborne particle deposition in cleanrooms: Relationship between deposition rate and airborne concentration. *Clean Air and Containment Review*, 25:4–10, 2016.

[61] Tsang-Jung Chang, Hong-Ming Kao, and Rita Sau-Wai Yam. Lagrangian modeling of the particle residence time in indoor environment. *Building and environment*, 62:55–62, 2013.

[62] Alvin CK Lai and Fangzhi Chen. Modeling particle deposition and distribution in a chamber with a two-equation reynolds-averaged navier–stokes model. *Journal of aerosol science*, 37(12):1770–1780, 2006.

[63] James R Pfafflin and Edward N Ziegler. *Encyclopedia of environmental science and engineering*, volume 1. Gordon and Breach, 1992.

[64] Prodrive Technologies. Prodrive technologies' optical sensor drives clean air in the car. `https://prodrive-technologies.com/news-articles/optical-sensor-drives-clean-air-in-the-car/`. accessed: 03.11.2022.

[65] DMT. Dmt test dust a2 fine. `https://testdust.dmt-group.com/en/standard-test-dust/9/dmt-test-dust-a2-fine`. accessed: 13.10.2022.

[66] Engeneering Toolbox. Air - dynamic and kinematic viscosity. `https://www.engineeringtoolbox.com/air-absolute-kinematic-viscosity-d_601.html`. accessed: 04.10.2022.

[67] Jousef Simscale. Defining turbulent boundary conditions. `https://www.simscale.com/forum/t/defining-turbulent-boundary-conditions/80895`. accessed: 04.10.2022.

[68] Shikha Maurya. Estimating turbulent boundary layer. `https://www.calculatoratoz.com/en/boundary-layer-thickness-for-turbulent-flow-calculator/Calc-11214`. accessed: 05.10.2022.

[69] Soon-Bark Kwon, Jaehyung Park, Jaeyoun Jang, Youngmin Cho, Duck-Shin Park, Changsoo Kim, Gwi-Nam Bae, and Am Jang. Study on the initial velocity distribution of exhaled air from coughing and speaking. *Chemosphere*, 87(11):1260–1264, 2012.

[70] Marcin Sosnowski, Jaroslaw Krzywanski, Karolina Grabowska, and Renata Gnatowska. Polyhedral meshing in numerical analysis of conjugate heat transfer. In *EPJ Web of Conferences*, volume 180, page 02096. EDP Sciences, 2018.

[71] Yun-Chun Tung, Shih-Cheng Hu, Tengfang Xu, and Ren-Huei Wang. Influence of ventilation arrangements on particle removal in industrial cleanrooms with various tool coverage. In *Building Simulation*, volume 3, pages 3–13. Springer, 2010.

[72] Ronald Gene Pinnick, JM Rosen, and DJ Hofmann. Measured light-scattering properties of individual aerosol particles compared to mie scattering theory. *Applied Optics*, 12(1):37–41, 1973.

[73] Megan R McGrory, Martin D King, and Andrew D Ward. Using mie scattering to determine the wavelength-dependent refractive index of polystyrene beads with changing temperature. *The Journal of Physical Chemistry A*, 124(46):9617–9625, 2020.

[74] Arup Bhattacharya, Andrew R Metcalf, Ali Mohammadi Nafchi, and Ehsan S Mousavi. Particle dispersion in a cleanroom–effects of pressurization, door opening and traffic flow. *Building Research & Information*, 49(3):294–307, 2021.

[75] Z Zhang and Qingyan Chen. Experimental measurements and numerical simulations of particle transport and distribution in ventilated rooms. *Atmospheric environment*, 40(18):3396–3408, 2006.

[76] Thomas Wriedt. Mie theory: a review. *The Mie Theory*, pages 53–71, 2012.

[77] Francesco Romano, Samanta Milani, and Cesare M Joppolo. Airborne particle and microbiological human emission rate investigation for cleanroom clothing combinations. *Building and Environment*, 180:106967, 2020.

[78] Wei Sun. Cleanroom airlock performance and beyond. *ASHRAE Journal*, 60(2):64–69, 2018.

[79] Volker Gnielinski. G1 heat transfer in pipe flow. In *VDI heat atlas*, pages 691–700. Springer, 2010.

[80] Boris Grigorevich Korenev. *Bessel functions and their applications*. CRC Press, 2002.

[81] L Schiller. Über die grundlegenden berechnungen bei der schwerkraftaufbereitung. *Z. Vereines Deutscher Inge.*, 77:318–321, 1933.

[82] Marcin Sosnowski, Renata Gnatowska, Jacek Sobczyk, and Waldemar Wodziak. Computational domain discretization for cfd analysis of flow in a granular packed bed. *Journal of Theoretical and Applied Mechanics*, 57(4):833–842, 2019.

A   Exact Dimensions of Geometries

Table A.1 – Table with all dimensions

Length scales	(m)
Total: l × b × h	8.4 × 3.0 × 3.0
Inlet: l × b	0.58 × 0.58
Outlet: l × b	0.3 × 0.6
Spacing inlets	0.02
Height table	0.85
Height outlet	0.15
Total L tables	3.9
Height injector	1.6
Height person	1.8
Width pillars	0.6
Velocity	**(m/s)**
Inlet	0.5
Oulet	-0.47
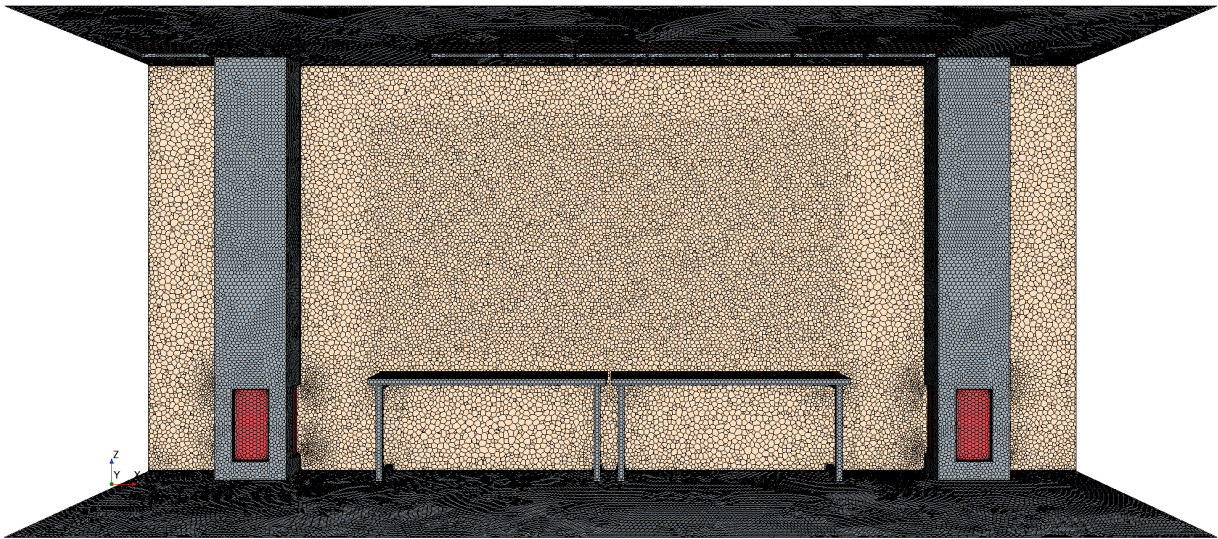
Figure A.1 – Mesh of a plane through the tables indicating the refinement that was added after the mesh independence study.

B   Particle counting sensor
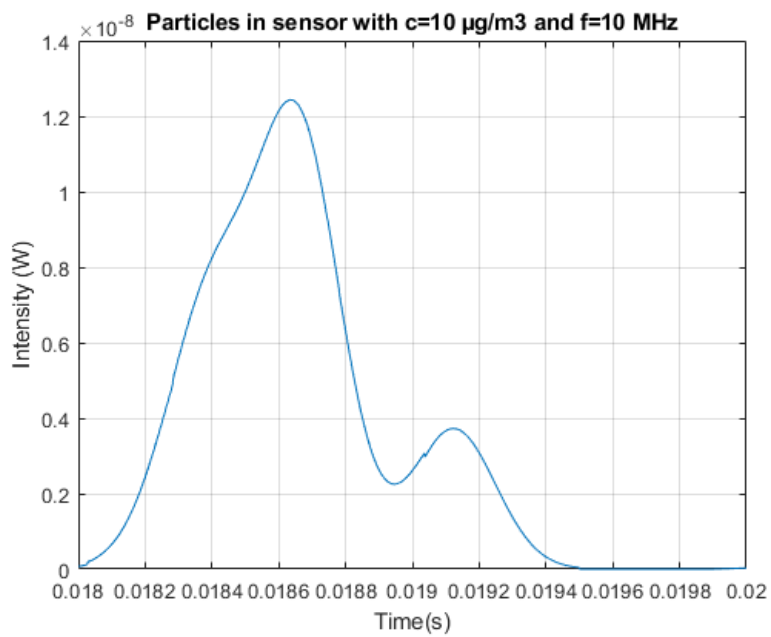
Figure B.1 – Part of modelled signal with a 40 MHz sampling frequency, still not able to distinguish the different particles.
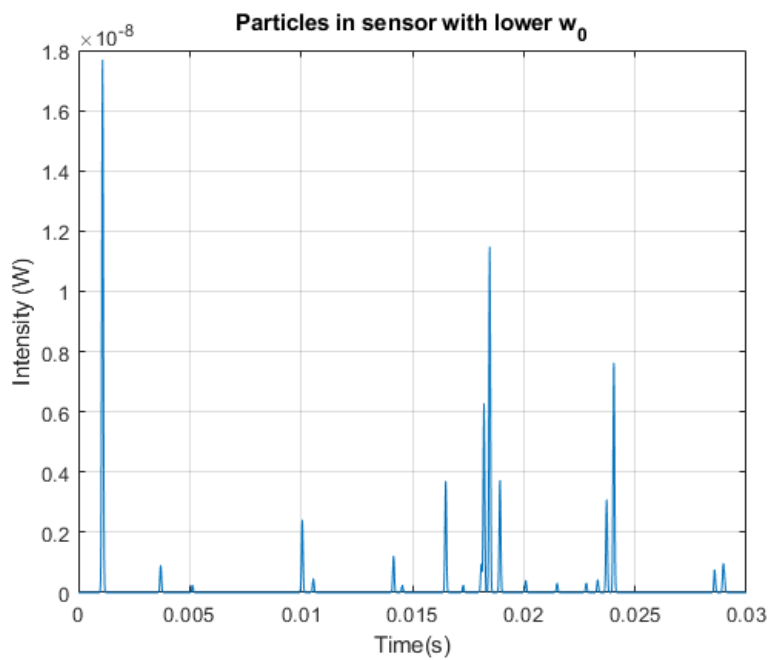

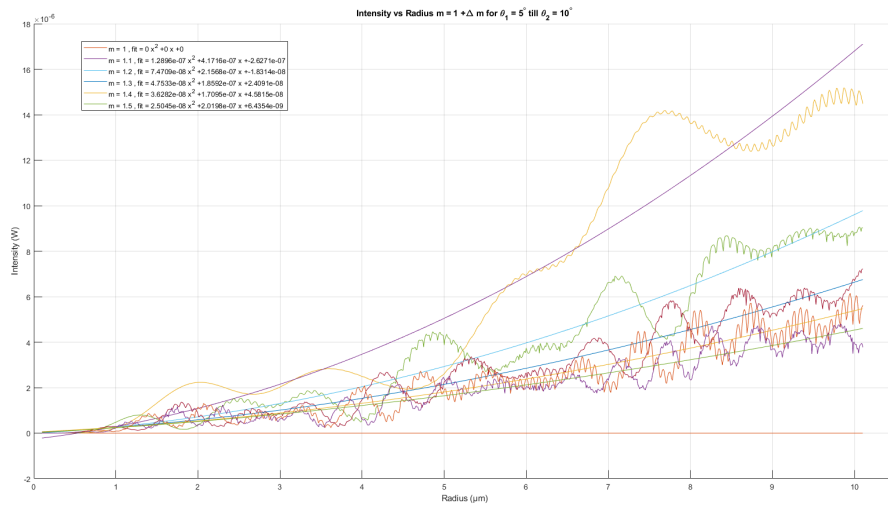*Figure B.2 – Same theoretical signal for lower w_0 of $\frac{1}{6}w$.*

Figure B.3 – Intensity vs. radius for different m and a constant Δm=0.1. Different relationships with oscillations are observed with the intensity becoming lower for increasing wavelength. The oscillations become smaller for higher m, but there appear more. The detection angle is 5° to 10°.
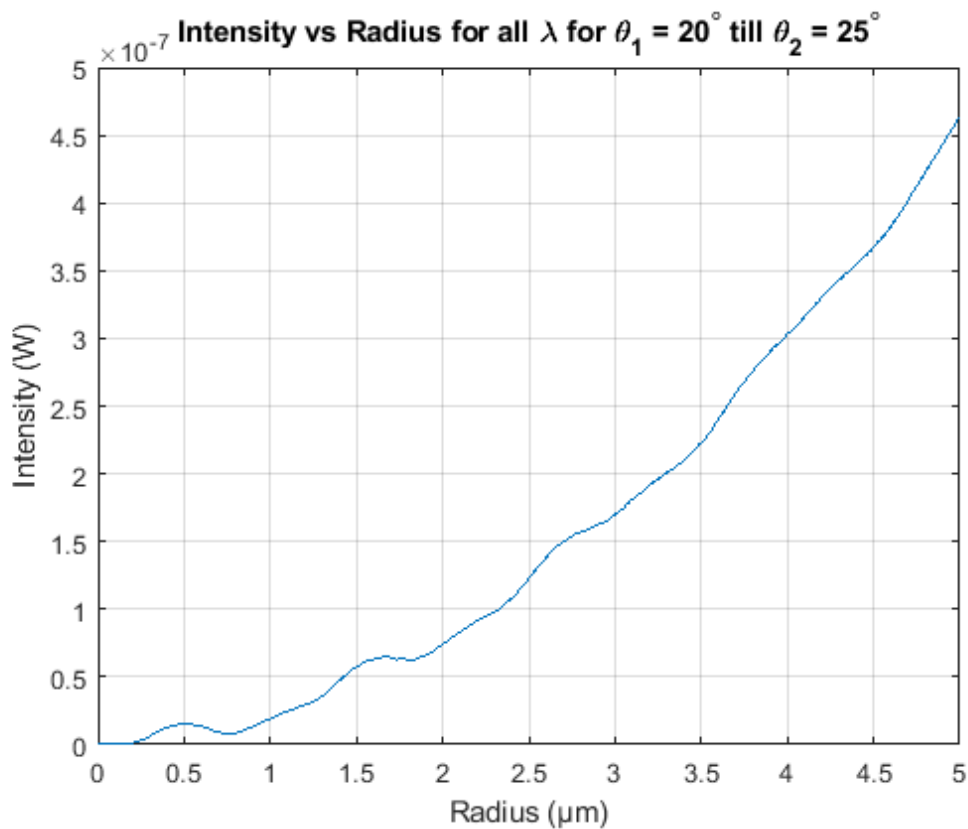

Figure B.4 – Intensity for a white light source as a function of R at a detection angle of 20°-25°.

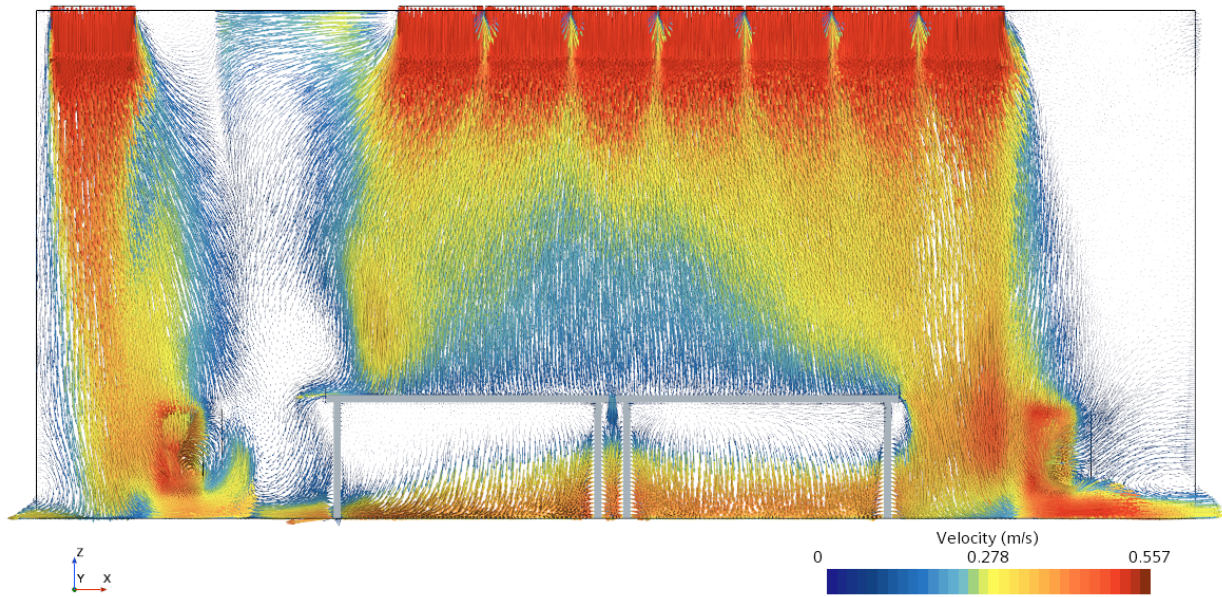# C Particle deposition in cleanroom

Figure C.1 – XZ-plane for geometry with only tables, illustrating the colliding of the flows between the pillar and the inlets.

D   Theoretical study on the lobes

In this appendix we describe another approach for relating scattering patterns to particle radius R. Looking back at the video in Fig. 4.7c, again more and more lobes start to appear for larger R. From these lobes we can determine the maxima and by plotting the number of peaks and the angular width of these peaks as function of particle radius we could possibly define an indicator for R. Here we define a detection angle of 10° to 70° to incorporate as many peaks as possible to lower the error. We assume we have a photodetector, that could determine intensity in this angular range as function of position where it reaches the detector. This could be the case for photodiode arrays in which one pixel corresponds with a photodiode and they can be separately addressed, these pixels can have dimensions of 0.5 µm. Plotting the number of peaks and angular width between these maxima as function of the radius we obtain Fig. D.1a and Fig. D.1b.

(a) Number of peaks   (b) Angular width

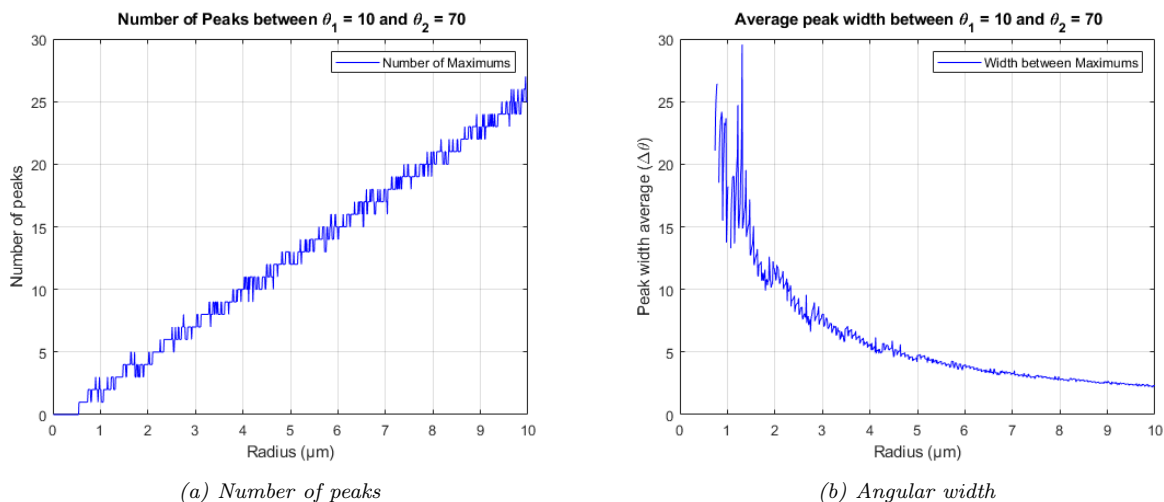*Figure D.1 – Theoretical analysis of the number of peaks and the angular width as function of the particle radius for a laser beam with λ=663 nm. From both plots the error in particle sizing is brought down to 1.2 µm at worst.*

From figure D.1a an almost linear relationship between R and the number of peaks arises. For R <0.6 µm we cannot determine its size from the number of peaks since no real maximum or lobes are present within the detection angle. The sizing error still is about 1 µm when using this, taking into account the discrete intervals for the number of peaks. For example, if we take the number of peaks to be 5, there are at least 9 corresponding particle sizes to this number. If we take a look at the graph of the angular width a couple of things can be noticed. The error is brought down to less than 1 µm for all radii, although above 5 µm the differentiation in angular width per radius becomes problematic due to the small differences in intensity. Again below 0.6 µm there are no lobes, so particles are not classifiable. Also, at several instances there is a sudden increase in angular width, such as 1.2, 1.8, 2.7 µm and more. This sudden increase relates to a sizeable lobe merging into the front lobe creating a large angular width between the front lobe and the next maximum, raising the average. Since in the beginning there are just a few lobes, the angular width can almost double around 1.2 µm. Since the scattering amplitude at around 90° and larger portrays suddenly drops and increases in the production zone, we limited ourselves to 70 degrees as a maximum angle. The same procedures can be done for backscattering and smaller detection angle. Since the average is then taken over a smaller number of lobes, fluctuations in the graphs showed a worse correlation. Due to the effect of noise on such small intensity levels, determining the exact maxima for the side lobes and thus the whole detection angle remains difficult. This in turn could lead to large errors. In conclusion single-wavelength lasers no clear one-to-one relation is found, as sizing errors of more than 1 µm is too large for properly binning of the particles.